WASHINGTON UNIVERSITY IN ST. LOUIS

Department of Physics

Dissertation Examination Committee:
James Buckley, Chair
Roger Chamberlain
Francesc Ferrer
Martin Israel
Henric Krawczynski
Lee Sobotka

Investigation of Energy-Dependent Morphology in Pulsar Wind Nebulae

by

Steven Brett McArthur

A dissertation presented to the
Graduate School of Arts and Sciences
of Washington University in
partial fulfillment of the
requirements for the degree
of Doctor of Philosophy

August 2012

Saint Louis, Missouri

Abstract

Observations of TeV gamma rays enable investigation of extreme, high-energy astrophysical environments. Of the identified TeV sources within the Galaxy, the largest number are pulsar wind nebulae (PWNe), formed by the shocked wind of relativistic leptons emitted by a pulsar and confined by the surrounding medium, with broadband emission arising from synchrotron and inverse Compton mechanisms. PWNe exhibit a wide range of morphologies as a result of a complex evolution, depending on the properties of the parent pulsar and confining medium.

This work describes the discovery of gamma-ray emission from the PWN within the supernova remnant (SNR) CTA 1 by the *VERITAS* telescope array. By imaging the Cherenkov light from gamma-ray induced atmospheric showers, *VERITAS* revealed an extended TeV nebula surrounding the pulsar PSR J0007+7303. Comparison of the observed properties with known PWN, along with a one-zone model, suggests a recent interaction with the SNR reverse shock and allows for an estimate of the average nebular magnetic field strength. No significant energy-dependent morphology is seen.

A multi-zone, cylindrically symmetric model is created to investigate tailed-out PWN morphology, accounting for multiple mechanisms for particle transport and cooling. The model is applied to the CTA 1 data, with a limited search of the parameter space performed to fit the observed spectrum and extent. Possible improvements to the model performance are discussed.

Acknowledgments

First and foremost, I'd like to thank my advisor Jim Buckley for his guidance, patience, and humor during the entire graduate school process, and for making my research sound interesting even when I felt a bit lost in its direction. Additional thanks go to the rest of my committee: Marty Israel, Francesc Ferrer, Henric Krawczynski, Roger Chamberlain, and Lee Sobotka. They've been a wonderful source of counsel throughout the last few years, and during the writing process in particular.

I'd like to acknowledge that my work has been supported through U.S. Department of Energy grant DEFG0291ER40628, the U.S. Department of Education GAANN Fellowship program, and the McDonnell Center Graduate Fellowships.

Thank you to my fellow VERITAS members for forming such a wonderful collaboration with an amazing instrument. Special thanks thanks to E. Aliu, R. Mukherjee, and O. Kargaltsev for sharing your experience with me, from the theory of PWNe to the trials of scientific paper writing. Additional thanks are due to the CTA 1 paper committee, who unknowingly managed to get the writing in a finalized shape with the perfect timing for me to include it here. Lastly, a huge thank you goes to the VERITAS crew in Arizona who have kept the telescope running with their blood, sweat, and tears, perhaps more literally than they'd like.

A big thank you to my astrophysics friends and colleagues at Wash U for making the office such a fun and interesting place to work: Kelly, Vicky, Qingzhen, Brian, John E., Ryan the Left, Ryan the Wise, Nathan, Avery, Jerrad, Trey, Richard, Slava, and Matthias. To all my non-astro friends (as well as those above), thank you for

making St. Louis such a wonderful distraction from the office, from the pub to the poker table. In particular, thank you to: Patrick, Mike, John, Dan, Lauren, Jeff, and Ben; everyone on This Team Goes to 11, Crowbar, and the Quantum Fielders; as well as Alli, Strongbow, and the staff of The Scottish Arms. Also, much gratitude goes to the Wash U staff, especially to Julia and Sarah for keeping us all happy, sane, and on track.

The appreciation I have for my family is indescribable, and I can never repay all the love and support they've given me on my journey here. Thank you one and all.

And finally, a tremendous thank you to my fiancée Sarah, whose boundless love and patience have kept me grounded, and who lets me look to the future with a smile. This work is dedicated to you.

Contents

List of Tables

List of Figures

Chapter 1

TeV astronomy

The idea of using Cherenkov flashes produced in extensive air showers (EAS) to study astrophysical TeV gamma rays was first put forward in the early 1960's (Jelley and Porter, 1963; Zatsepin and Chudakov, 1961). It was realized that while the sources of normal cosmic rays (CRs) could not be directly observed due to the bending of the charged particles' paths in the interstellar magnetic fields, high-energy photons produced in the same environments would not suffer such deviations and could be used as tracers of the cosmic ray production sites. However, it was not until 1989 that the first detection of a TeV source was achieved by the Whipple Observatory, with an unambiguous detection of the Crab Nebula (Weekes et al., 1989). Since then, the catalog of TeV sources has expanded to over 100 objects (see Figure 1.1). These sources can be classified into several categories:

Galactic

Sources within our own galaxy, including supernova remnants (SNRs), pulsars, pulsar wind nebulae (PWNe), and binary systems.

Extragalactic

Sources outside our galaxy, including active galactic nuclei (AGNs) and starburst galaxies.

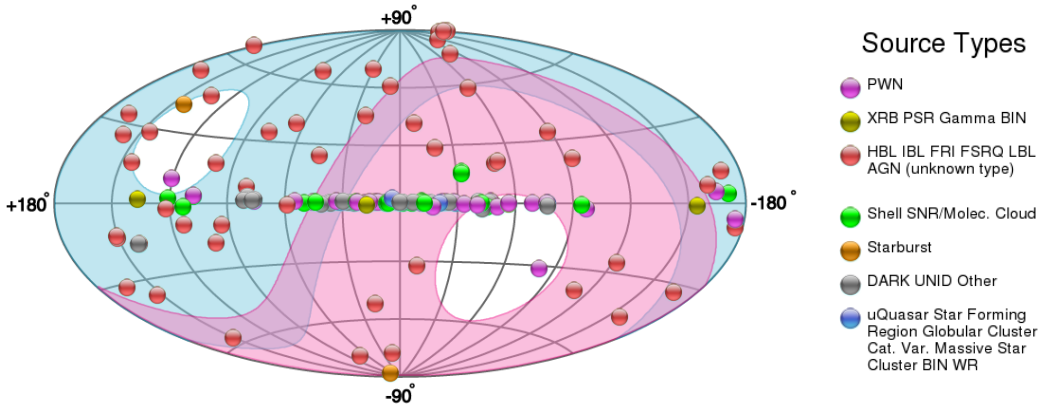

Figure 1.1: Skymap of known TeV sources, as of July 2012, presented in Galactic coordinates. The blue shaded region marks the area of sky best observable by *VERITAS*/*MAGIC*. The pink shaded regions marks that of *HESS*. Produced using the online catalog TevCat (Wakely and Horan, 2012).

Unidentified

Sources where the origin of the radiation is unknown, including numerous sources where no counterpart is seen at other wavelengths.

Observations have also been made of gamma-ray bursts (GRBs) and suspected concentrations of dark matter such as globular clusters and dwarf spheroidal galaxies. No signal has been detected from either class of objects (see, for example, (Abramowski et al., 2011; Acciari et al., 2011; Aleksić et al., 2011)), with the possible exception of the globular cluster Terzan 5 (H.E.S.S. Collaboration et al., 2011).

This section shall give a general overview of physical processes relevant to TeV astronomy and the general technique of Imaging Atmospheric Cherenkov Telescopes (IACTs), along with a more detailed description of the IACT known as *VERITAS*.

1.1 Mechanisms for high-energy emission

Radiation in the very-high-energy (VHE) regime is dominated by non-thermal processes, i.e. radiation processes which do not result in a Planck blackbody spectrum. These processes all arise from the interaction of highly relativistic charged parti-

cles with ambient magnetic fields, photon fields, and gas, as well as the possible annihilation/decay of dark matter. The production of TeV photons is dominated by inverse Compton scattering of ambient background radiation by relativistic electrons/positrons (the leptonic channel) and by the decay of neutral pions produced in the interaction of relativistic nuclei with clouds of interstellar gas (the hadronic channel). Non-thermal processes like synchrotron emission will form the spectra at lower energies and play a part in the cooling of particles, and so will also be discussed below. Detailed reviews of these processes may be found in Longair (1994) and Rybicki and Lightman (1979).

1.1.1 Synchrotron radiation

A relativistic particle of charge q and Lorentz factor γ gyrating around magnetic field lines will emit synchrotron radiation. This radiation will be beamed within a cone of opening angle γ^{-1}, with a spectrum that falls off sharply above the critical frequency

$$\nu_c = \frac{3|q|B}{4\pi mc}\gamma^2 \sin\theta, \tag{1.1}$$

where B is the magnetic field strength, m is the particle mass, and θ is the pitch angle of the particle velocity with respect to the magnetic field. For an isotropic distribution of pitch angles, the average rate of energy loss is

$$\frac{dE}{dt} = -\frac{4}{3}\sigma_T c\beta^2\gamma^2 U_B, \tag{1.2}$$

with $\sigma_T = 8\pi q^4/3m^2c^4$ is the Thomson cross-section, $\beta = v/c$, and $U_B = B^2/8\pi$ is the energy density of the magnetic field. In almost all cases, electron synchrotron emission dominates over that of other particles as the cross section scales like m^{-2}, making the lighter particles much more efficient radiators. The cooling time scale for

electrons due to synchrotron radiation is then given by

$$\tau_{sync} \equiv -\frac{E}{dE/dt} \sim \frac{1}{EB^2}. \tag{1.3}$$

It can be shown (Rybicki and Lightman, 1979) that a power-law distribution of particles with index p, $N(E) \sim E^{-p}$, will emit a power-law synchrotron spectrum $F(\nu) \sim \nu^{-(p-1)/2}$.

1.1.2 Curvature radiation

Curvature radiation is similar to synchrotron radiation in that it results from the acceleration of a relativistic charged particle within a magnetic field. Equation 1.1 can be rewritten as

$$\nu_c = \frac{3c}{4\pi R_c}\gamma^3, \tag{1.4}$$

where $R_c = \gamma mc^2/|q|B\sin\theta$ is the radius of curvature of the particle's helical orbit around the magnetic field line. If the particle were to travel along the field line rather than around it, and R_c is taken as the radius of curvature of the field line itself, then Equation 1.4 describes the critical frequency of curvature radiation. As the emitting particle is relativistic, the radiation is again beamed with an opening angle of γ^{-1}. However, as the beaming is in the direction of the particle motion, it is emitted along the direction of the field line rather than normal to the field line as in synchrotron radiation. This radiation mechanism is important for describing the emission from within the pulsar light cylinder, where magnetic fields are large and highly curved (Longair, 1994).

1.1.3 Inverse Compton scattering

When a relativistic electron interacts with a low-energy "seed" photon, it may transfer some of its energy and momentum to the photon via inverse Compton (IC) scattering.

The following discussion is limited to electrons since the radiated power scales as m^{-2} and, as was the case for synchrotron, is usually only appreciable for electrons. The low energy seed photon may be part of any radiation field, including the cosmic microwave background (CMB), local infrared (IR) fields from dust clouds, or optical light from stars. If a population of electrons scatters the same synchrotron photons that it emits, the process is synchrotron self-Compton (SSC).

A seed photon of energy $h\nu_0$ interacting with an electron with Lorentz factor $\gamma \gg h\nu_0/mc^2$ will, on average, scatter to an energy of $h\nu = \frac{4}{3}\gamma^2 h\nu_0$. The average energy-loss rate for an electron in an isotropic seed photon field of energy density U_{ph} is

$$\frac{dE}{dt} = -\frac{4}{3}\sigma_T c \beta^2 \gamma^2 U_{ph}. \tag{1.5}$$

This has the same form as the synchrotron loss rate (1.3), so that

$$\frac{(dE/dt)_{sync}}{(dE/dt)_{IC}} = \frac{U_B}{U_{ph}}. \tag{1.6}$$

The equations given above are strictly only valid in the Thomson regime, i.e. for energies satisfying the relation $4h\nu E_e \ll (mc^2)^2$. Above this limit, the electron loses a substantial fraction of its energy in a single scattering, and the full Klein-Nishina cross-section must be used so that the probability of the interaction is suppressed (Blumenthal and Gould, 1970). For the peak frequency of the CMB ($T = 2.73$ K), the transition occurs for electron energies ~ 100 TeV.

The CMB has an energy density of 0.26 eV cm^{-3} regardless of location, corresponding to an equivalent magnetic field of ~ 3 μG. For sources in the Galactic plane, the energy densities of the diffuse NIR ($kT \approx 0.3$ eV) and FIR ($kT \approx 6 \times 10^{-3}$ eV) backgrounds are each of the order $\lesssim 0.2$ eV/cm^{-3} (Hinton and Aharonian, 2007; Moskalenko et al., 2006). However, for these photon fields, the Klein-Nishina suppression is achieved at lower electron energies, so their contribution to the IC spectrum

and loss rate tend to be much lower, or at most, on the order of the CMB contribution. Therefore, for a magnetic field $B > 3$ μG, synchrotron losses will tend to dominate over the IC losses, with IC losses off the CMB providing a good approximation to the total IC losses. Synchrotron self-Compton emission is usually only important in select environments such as the Crab Nebula.

1.1.4 Neutral pion decay

TeV gamma rays may also be produced through the decay of pions created in the collision of a high-energy proton with another nucleon, or (in very high-energy sources) in electromagnetic cascades initiated by the interaction of a VHE proton ($\gtrsim 10^{16}$ eV) with an ambient photon resulting in the photoproduction of pions. For the galactic sources of interest here, only the proton-nucleon production mechanism is likely to play a major role, and this will be the focus of the remaining discussion. This proton-nucleon collision will produce both charged and neutral pions, each species in approximately equal number. While the charged pions ($\pi^{+/-}$) of Lorentz factor γ_μ will decay with a mean lifetime of $2.6 \times 10^{-8} \gamma_\mu$ s into a leptonic shower of muons, electrons/positrons, and neutrinos, the neutral pions (π^0) will decay with a much shorter lifetime ($8.4 \times 10^{-17} \gamma_\mu$ s) into a pair of gamma-rays. This process plays the greatest role when a large population of energetic protons encounters a dense medium, for instance when a supernova shock collides with a molecular cloud (see, for example, Giordano et al. 2012).

1.1.5 Useful scalings

We can now list some useful numerical results for the work that follows. These results assume we have highly relativistic electrons undergoing synchrotron and inverse Compton cooling, with the IC cooling occurring on the CMB. An electron of energy

E will emit radiation with typical energies of

$$E_{sync} = 2.2 \left(\frac{E}{100 \text{ TeV}} \right)^2 \left(\frac{B}{10 \ \mu\text{G}} \right) \text{ keV}, \tag{1.7}$$

$$E_{IC} = 0.25 \left(\frac{E}{10 \text{ TeV}} \right)^2 \text{ TeV}, \tag{1.8}$$

assuming IC scattering in the Thomson regime (thus the choice of scaling to 10 TeV rather than 100 TeV). The corresponding cooling time scales are

$$\tau_{sync} = 1.25 \left(\frac{100 \text{ TeV}}{E} \right) \left(\frac{10 \ \mu\text{G}}{B} \right)^2 \text{ kyr}, \tag{1.9}$$

$$\tau_{IC} = 119 \left(\frac{10 \text{ TeV}}{E} \right) \text{ kyr}. \tag{1.10}$$

1.2 Cherenkov radiation

An energetic particle, moving through a dielectric medium at a speed βc exceeding that of the electromagnetic phase velocity in the medium will emit a faint continuum of bluish-white light. Named *Cherenkov radiation* or *Cherenkov light* after Pavel Cherenkov, who performed the first[1] systematic study of the phenomenon (Cherenkov, 1934), the theoretical explanation was put forth by Frank and Tamm (1937).

As a charged particle moves through a dielectric medium with refractive index $n(\nu)$, its electric field will distort the atoms in its local vicinity, inducing a small dipole moment in each. As the particle moves away, these dipoles will relax back to the atoms' equilibrium configurations. Each of these time-varying dipoles can, in principle, emit electromagnetic radiation, depending on the phase relation between neighboring regions. If the particle moves slowly through the medium, the net polarization around its position will be symmetric, and no net field will extend to large distances, i.e. no radiation is emitted.

[1] Although, as noted by Jelley (1958), the first mention of the phenomenon may have been made by Marie Skłodowska-Curie, 24 years before Cherenkov's studies.

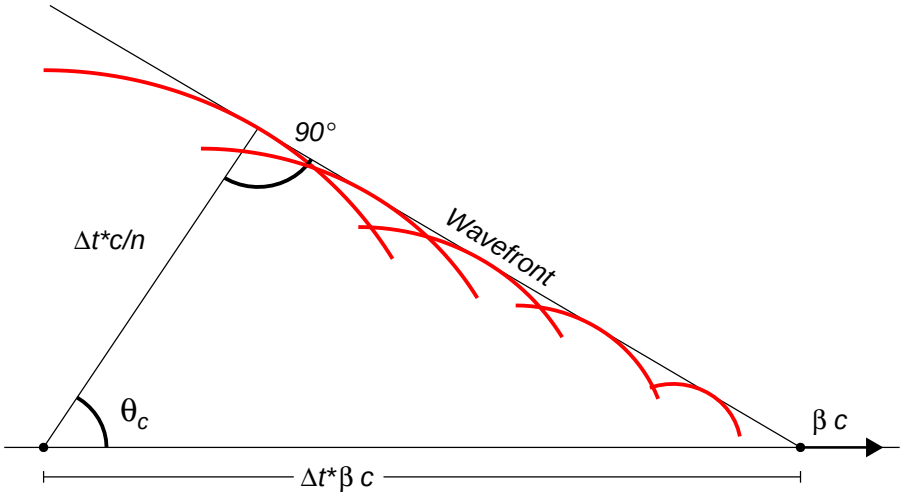

Figure 1.2: Huygens principle construction for Cherenkov radiation. The charged particle travels through a medium of refractive index n with speed $v = \beta c$. The electromagnetic phase velocity is $c/n < v$.

If, however, the particle speed exceeds the local phase velocity ($\beta c > c/n$), then the net polarization will not average out, as the atoms ahead of the particle have not yet reacted to its presence. Therefore, each point along the particle's track will emit a small electromagnetic pulse. Figure 1.2 illustrates via Hugyen's principle how these pulses add constructively at a given angle from the particle's trajectory. This Cherenkov angle θ_C is easily derived as

$$\cos\theta_C = \frac{c/n}{\beta c} = \frac{1}{\beta n}. \tag{1.11}$$

This gives the threshold speed of $\beta_{th} = 1/n$, as $\cos\theta_C \leq 1$. For a particle of rest mass m, this corresponds to a threshold energy of

$$E_{C,th} = \gamma mc^2 = \frac{mc^2}{\sqrt{1-n^{-2}}} \tag{1.12}$$

The maximum Cherenkov angle for any particle is given by taking the limit $\beta \rightarrow 1$:

$$\theta_{C,max} = \arccos\left(n^{-1}\right) \tag{1.13}$$

For the case of Cherenkov radiation in air, the density (and thus refractive index) of the atmosphere decreases with altitude. At sea level, the refractive index at visible wavelengths is 1.00029, so the maximum Cherenkov angle $\theta_{C,max} = 1^{\circ}.4$ at sea level, and about $0^{\circ}.8$ at an altitude of $\sim 8 - 10$ km, where VHE γ-ray showers typically reach their maximum development. Similarly, the threshold energies at sea level for electrons and protons are 21 MeV and 39 GeV, respectively.

1.3 Cherenkov radiation from air showers

1.3.1 Electromagnetic cascades

Due to various absorption processes, photons of wavelength less than a few hundred nm are unable to penetrate the Earth's atmosphere to the surface. This normally requires telescopes for energies above the UV to be based on satellites orbiting the Earth. Due to the steeply falling spectra of arriving gamma-rays (for a power-law flux $F(E) \sim E^{-\Gamma}$, $\Gamma > 2$ for most detected TeV sources) and the limited effective area for space-borne instruments (on the order of a few square meters at most), the sensitivity of such a detector for TeV gamma rays would be very small. However, above a threshold of $\sim$ 50 GeV, the atmosphere itself may be used as a detector through the use of Cherenkov air showers.

A gamma-ray induced air shower begins when an incident photon of energy $h\nu \gg 2m_e c^2$ enters the atmosphere and creates an electron-positron pair in the electromagnetic field of an atmospheric molecule at an altitude of $\sim$ 20 km above sea level. These particles share the energy of the original gamma ray so that they are

both highly relativistic. Each particle may then create another high-energy photon via bremsstrahlung in the electric field of a nucleus in an air molecule. This photon may itself pair-produce, with the new electrons also undergoing bremsstrahlung, etc., creating an *electromagnetic cascade*. The radiation lengths for both the pair-production and bremsstrahlung processes, ξ_{pp} and ξ_b respectively, are approximately equal for highly relativistic particles in air: $\xi_b \approx \frac{7}{9}\xi_{pp}$ (Longair, 1994). Denoting the distance at which the probability of interaction is one-half as X, such that

$$\begin{aligned} &\exp(-X/\xi) = 0.5 \\ &\Rightarrow X = \xi \ln(2), \end{aligned} \tag{1.14}$$

the number of particles after a distance d will be $\sim 2^{d/X}$, with the average energy of each particle/photon being $2^{-d/X}E_0$, where E_0 is the energy of the original gamma ray, as illustrated in Figure 1.3. The cascade continues until the average particle energy drops below the critical energy, $E_c \sim 83$ MeV, where ionization losses become dominant over bremsstahlung losses for the charged particles, and Compton scattering of the photons dominates over pair production. Particles below this energy rapidly climb up the dE/dx curve for photoionization loss, losing all of their remaining energy in a path length $< X$. Once the condition on the average particle energy is reached, statistical fluctuations in the secondary particle energies will lead to the shower gradually dying out, rather than an abrupt termination.

As the electron-positron pairs produced in the shower are highly relativistic, they emit Cherenkov light which propagates to the ground. The narrow angle of Cherenkov emission, slight Coulomb scattering of the shower particles, and deflection of the charged particles in the geomagnetic field result in a fuzzy cone of radiation $\sim$ 1–2° in opening angle. As the height of maximum shower extent lies approximately 10 km above sea level, the Cherenkov light at ground level is spread over an area $\sim$ 130 m

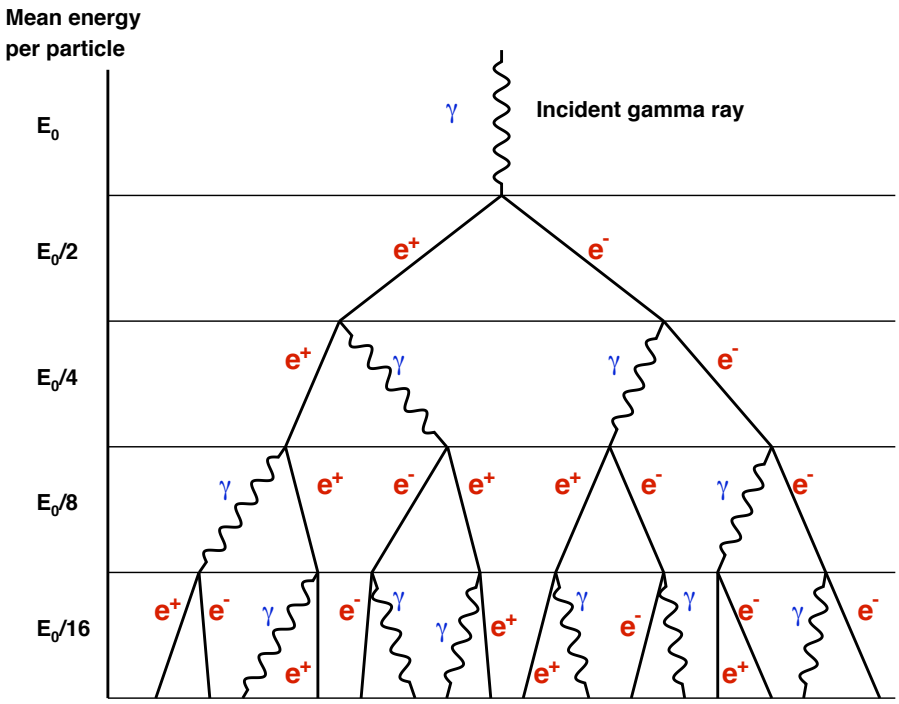

Figure 1.3: Simple model of a gamma-ray induced air shower, following that of Heitler (1954).

in radius.

1.3.2 Hadronic cascades

However, gamma rays are not the only source of atmospheric air showers. Hadronic cosmic rays—primarily protons—will initiate similar air showers. Upon first interaction in the atmosphere, a number of secondary particles are produced, including pions ($\pi^{\pm}, \pi^{0}$) which rapidly decay into secondary particles. The neutral pions decay into two gamma rays ($\pi^{0} \rightarrow 2\gamma$) with mean lifetime of $\tau_{\pi^{0}} = 8.4 \times 10^{-17}\gamma_{\pi}$ s, initiating electromagnetic cascades as described above (see Figure 1.4).

The charged pions decay into muons with a mean lifetime of $\tau_{\pi^{\pm}} = 2.6 \times 10^{-8}\gamma_{\pi}$ s

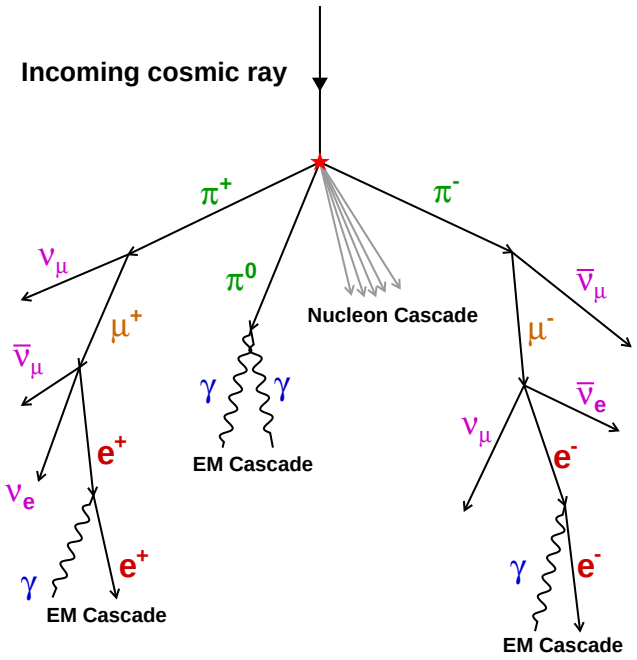

Figure 1.4: Model of a hadronic air shower.

into muons and neutrinos:

$$\pi^+ \rightarrow \nu_\mu \mu^+$$

$$\pi^- \rightarrow \bar{\nu}_\mu \mu^-.$$

The muons may then decay into electron/positrons which initiate electromagnetic cascades, although their time-dilated decay lifetime is long enough ($\tau_\mu = 2.20 \times 10^{-6} \gamma_\mu$ s) that they may reach ground level intact.

Hadronic showers are distributed isotropically across the sky and greatly outnumber the gamma-ray induced showers—the flux from even a strong gamma-ray source may be only be a fraction of a percent of the hadronic flux. Such showers thus form the dominant background for TeV observations. Fortunately, the different components and interactions of hadronic cascades provide a means of distinguishing between the two populations. The inelastic scattering of the hadronic secondaries and complex

overlap of multiple electromagnetic subshowers result in a Cherenkov image that is both broader and more irregular that gamma-ray-induced images.

1.4 Atmospheric Cherenkov Imaging Telescopes

The standard technique for atmospheric Cherenkov imaging makes use of large optical reflectors to focus Cherenkov flashes onto a pixelated camera. Each pixel consists of a photomultiplier tube (PMT), which can provide efficient detection of single photons ($\sim$ 25%) with a fast response time ($\sim$nsec). While based on old vacuum tube technology, PMTs are still the most sensitive single photoelectron detectors due to the low noise and high gain of the vacuum electron multiplier. The fast response of the camera PMTs and electronics allows for imaging the faint optical flashes of individual showers against the night-sky background. A telescope can image a particular air shower so long as it is located within the Cherenkov light pool, resulting in an effective area of tens of thousands of square meters, many orders of magnitude greater than that of satellite instruments.

As the Cherenkov light from various points along the shower profile are imaged onto the camera, they form a two-dimensional projection in the shape of an ellipse, as illustrated in Figure 1.5. Various properties of the shower development are imprinted on the distribution of light in the focal plane. For instance, the more energetic showers penetrate deeper into the atmosphere and deposit more light (thus creating larger signals in the PMTs). The arrival direction of the shower lies along the major axis of the image ellipse. The larger lateral and longitudinal extent of hadronic showers compared to gamma-ray showers results in wider and longer images in the camera. Hillas (1985) first suggested that these sorts of properties of shower images could be used to separate gamma-ray and hadronic showers, leading to the initial detection of the Crab Nebula. This method is based on calculating the various moments of the light distribution to determine the RMS width, length, centroid position, orientation,

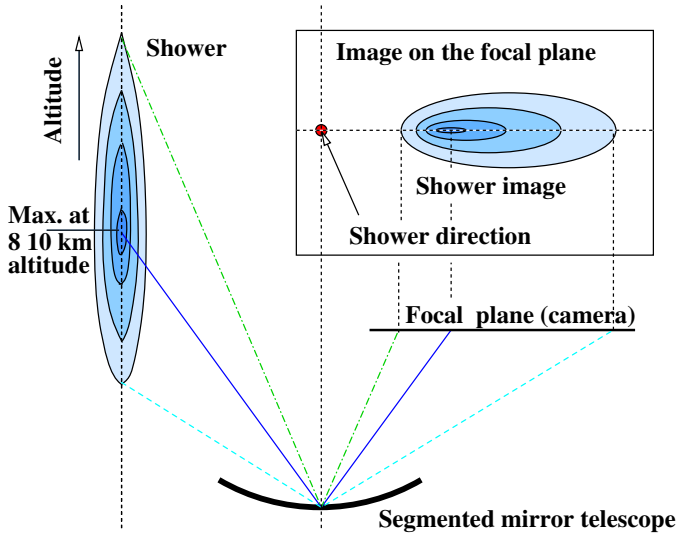

Figure 1.5: Cartoon of an IACT imaging an air shower, taken from (Völk and Bernlöhr, 2009).

and parallactic displacement of the shower image (the so-called 'Hillas parameters', see Figure 1.6 for examples).

The current generation of IACTs use multiple telescope to obtain stereoscopic imaging of showers. Requiring at least two telescopes to register an event within a short time window allows for increased rejection of accidental triggers from the general night-sky background (NSB) and a reduction in triggers from single muons created in hadronic showers (assuming the spacing between telescopes is greater than the size of a typical muon lightpool). Stereoscopic imaging also enables improved reconstruction of the shower direction (giving improved angular resolution) and the impact point of the shower axis (allowing for improved energy resolution through corrections for the lateral distribution of Cherenkov light). Event reconstruction and selection will be explained in more detail in Section 2.3.

IACTs suffer from two disadvantages when compared to both space-based observatories such as *Fermi* and water Cherenkov arrays such as Milagro and HAWC:

1. The high sensitivity of the PMTs inside the camera typically allow for observa-

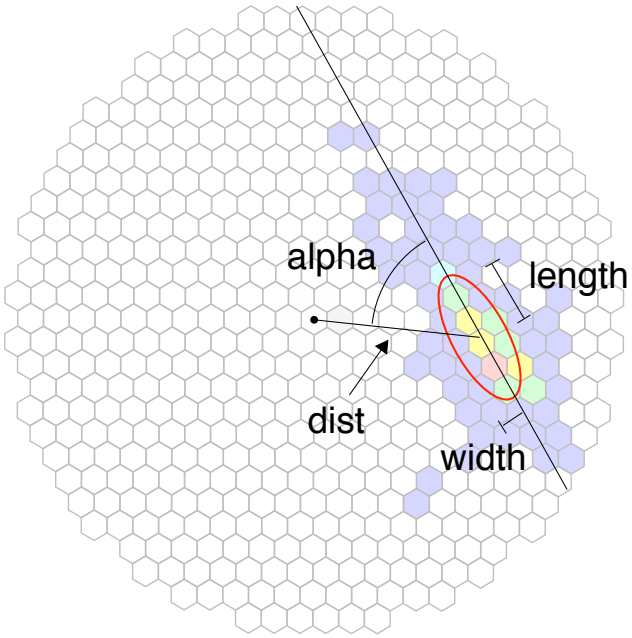

Figure 1.6: Illustration of some of the original Hillas parameters.

tions only on nights of low illumination of the moon. Local weather conditions also restrict observations to times of low humidity and clear skies. These factors combine to give IACTs a low duty cycle, typically only a few hundred hours per year.

2. The narrow field of view ($\lesssim 5°$) restricts standard operations to imaging individual sources, either known or suspected.

These factors are compensated by the large effective area (compared to satellite instruments) and improved gamma-hadron separation, spatial resolution and energy resolution (compared to water Cherenkov arrays).

Chapter 2

VERITAS

One of the current generation of TeV instruments, the Very Energetic Radiation Imaging Telescope Array System (*VERITAS*) is built upon the success of the Whipple 10-meter telescope. An array of four telescopes, it uses stereoscopic imaging of Cherenkov air showers to achieve improved sensitivity and shower reconstruction over its predecessor. This chapter describes both the hardware, data acquisition, and standard analysis methods of *VERITAS*.

2.1 The *VERITAS* array

Located at Fred Lawrence Whipple Observatory at the base of Mt. Hopkins south of Tucson, AZ, *VERITAS* officially began full operations in 2007. The array consists of four 12-meter Davies-Cotton design telescopes arranged in a quadralateral footprint, with sides of length 80 m, 110 m, 90 m, and 130 m. As originally constructed, two of the telescopes were positioned only 35 m apart, until telescope T1 was relocated in the summer of 2009 to the present configuration. Figure 2.1 show a photograph of the current array layout.

Each telescope's optical reflector is a 12 m segmented dish consisting of 350 hexagonal glass mirrors, each of area 0.32 m^2, for a total mirror area of ~ 110 m^2 per tele-

Figure 2.1: Photograph of the *VERITAS* array at the Fred Lawrence Whipple Observatory near Tucson, AZ, as of September 2009. Photo credit: S. Criswell, Whipple Observatory.

scope. The mirrors are mounted on a steel, counterweight-balanced optical-support-structure (OSS) controlled by an altazimuth positioner. The mirrors direct light into a camera containing 499 high-quantum-efficiency, UV-sensitive PMTs in a circular arrangement, with a total field of view of 3°.5. An array of Winston cone reflectors in front of the focal plane both decreases dead-space between PMTs and restricts the collection of light to photons coming from the direction of the reflector, decreasing off-axis contamination. The high voltage for each PMT is provided by a commercial power supply and is set to achieve a gain of $\sim 2 \times 10^5$, typically at the level of several hundred volts, with uniformity across the camera achieved by a flat-fielding procedure. Average PMT currents range between $4 - 8\ \mu$A for standard dark-sky observations.

2.2 Trigger system and data acquisition

The signal from a PMT passes through a high-bandwidth pre-amplier circuit built into the base of each PMT The amplified signal is sent to a 500 Msample/s flash analog-to-digital converter (FADC) system. This system digitizes the signal with 8-

bit precision, with a 2 ns sample size. If the signal exceeds the range of the digitzer, as determined by one copy of the signal sent to the *Hi/Lo* discriminator switch, then a third copy of the signal is digitized which has been delayed and reduced in gain by a factor of ~ 6. A DC bias voltage (*pedestal*) is also applied to the signal so that both positive and negative variations in the PMT signal can be measured. In the absence of an array-wide L3 trigger signal (explained below), these pedestal levels are read out at a rate of ~ 1 Hz. The pedestal level and its variations are used as a measure of the night-sky background and electronic noise from which the Cherenkov signal must be extracted. The digitized waveform is then stored in a 32 μs ring buffer, allowing for a similar delay in the array trigger.

VERITAS makes use of very large reflectors and fast photodetectors and electronics to distinguish the faint Cherenkov pulses from Poissoin fluctuations in the NSB. The NSB light has various contributions including scattered and direct moonlight, lightning, starlight, zodiacal light, and artificial light pollution. In addition to the shot noise from the NSB, additional sources of electronic noise make a small contribution to the fluctuation baseline against which the small Cherenkov pulses must be extracted. A three-level trigger system is used to decrease the accidental coincidence rate from these background events, allowing a reduction in trigger threshold and hence an improvement in the detection efficiency for the lowest-energy gamma-ray events which have fewer Cherenkov photons and thus a smaller signal-to-noise ratio.

The first trigger level (L1) is a pixel-wise trigger, consisting of a custom-built constant fraction discriminator (CFD) built into each channel of the FADC modules. The L1 trigger condition is satisfied when the PMT signal crosses a programmable threshold, chosen to optimize the overall trigger rates and usually set to 50 mV for typical dark sky conditions (see Figure 2.2). To account for varying pulse heights, which would lead to scatter in the trigger signal timing, a second condition must be met, whereby two other copies of the signal, one scaled in amplitude, the other

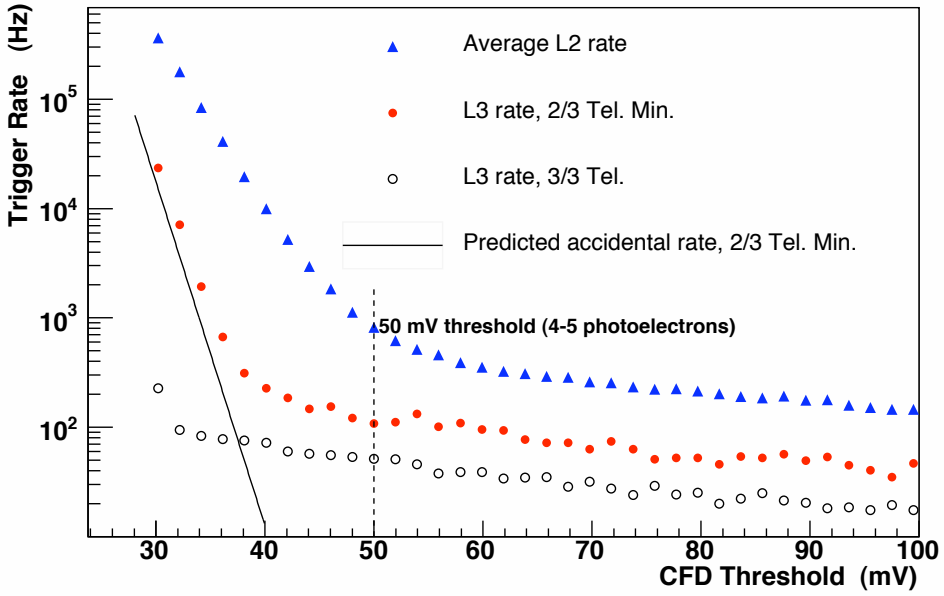

Figure 2.2: A sample bias curve, taken from Weinstein (2008), showing the dependence of the L2 and L3 trigger rates on CFD threshold. The curves were taken for a three-telescope array configuration, with the only the average L2 rate shown. The L3 rate is shown for both 2-telescope and 3-telescope coincidence conditions. The steeply falling rates to the left of the curves are dominated by NSB triggers, while those to the right are dominated by cosmic-ray showers.

inverted and delayed in time, are summed. For a trigger to occur, this total signal must cross zero while the original signal is still above threshold, and this zero-crossing time (occurring approximately at the time when the pulse rises to a fixed fraction of its maximum amplitude) provides the timing edge for the L1 trigger. The L1 circuit also incorporates a rate feed-back (RFB) loop, which increases the effective offset in the zero-crossing circuit during periods of higher noise rates (and thus higher trigger rates).

The second-level trigger (L2, or pattern trigger), operates on a per telescope basis and is intended to further reduce accidental triggers from NSB noise. The L2 requires that events passing the L1 condition on a programmable number of adjacent pixels (usually three) arrive within a short coincidence window ($\sim$ 6 ns). The L1 signals are fed into a set of electronic modules that analyze overlapping sectors of the camera. In the Leeds trigger system (used from 2007 to 2011), the modules compare the pattern of L1 triggers to a set of prechosen patterns, stored in the module's RAM. The outputs of the selection modules feed into an OR logic circuit, so that a positive signal from any one module results in a positive trigger for the entire L2 system. Beginning in autumn 2011, a new L2 system was installed. This system uses programmable gate arrays to look for coincident triggers of adjacent pixels. Preliminary tests indicate that the system provides a reduced coincidence time (with a reduction in the accidentals rate) and improved gamma-ray efficiency compared with the original pattern trigger electronics.

The third, array-level trigger (L3) receives the signals from the four L2 modules and initiates data read-out if there is a coincidence between the telescope (L2) systems. The L3 is housed in a central control building, with connections to the L2 systems provided by high-speed fiber optic signal cables which introduce known time delays between the L2 triggers. In addition to these fixed delays, the Cherenkov light front of a shower will arrive at the various telescopes at different times depending on

the telescope pointing. These delays are compensated for by a Pulse Delay Module (PDM) before sending the signals to the coincidence logic algorithm of the Sub-Array Trigger (SAT) board. The SAT requires that the L2 signals from a preset number of telescopes (typically 2) arrive with in a short (typically 50 ns) window.

When an event passes the array trigger, a signal is sent back to the data acquisition system in each telescope to read out the corresponding event from the FADC buffers. As data is read out, the L3 is inhibited by a BUSY signal to prevent further triggers, resulting in a deadtime of $\sim 10\%$ for typical operational L3 rates of 200–300 Hz. The PMT waveform data, L1 trigger pattern, Hi/Lo switch pattern, array event number, and local GPS time are collected by an *event builder* process. At the end of the run the accumulated events are compressed on a Harvester computer into a single raw data file and eventually transfered to an archival server at UCLA.

2.3 Data analysis

As described above, the raw data recorded by *VERITAS* consists of digitized PMT signal traces, along with supplementary data such as a GPS time stamp. From this data, one must extract the shower signal from electronic and NSB noise, derive relevant properties of the showers, and determine the significance and spectrum of the observed gamma-ray source. Such analysis is generally performed with one of two analysis packages: *EventDisplay* (Daniel, 2008) or the VERITAS Gamma-Ray Analysis Suite (VEGAS) (Cogan, 2008). Both packages are C++ object-based codes using structures from the ROOT (Brun and Rademakers, 1997) libraries. The general analysis procedure consists of the following stages:

- Calibration and image cleaning
- Image parameterization and shower reconstruction for each telescope
- Stereoscopic event reconstruction

- Gamma-hadron separation
- Excess significance calculation and spectral reconstruction

A more detailed description of each stage is given below. The specific implementations described refer to those in the VEGAS package. Those in *EventDisplay* may differ in details, but the general methods are the same.

2.3.1 Calibration and image cleaning

As mentioned above, the current from each PMT goes through a preamplifier to the FADC. To determine the total charge in each Cherenkov pulse, the FADC trace is integrated over a preset window (with individually programmable time offset and width determined by timing calibrations.) In order to extract the shower-induced signal from the background noise in each PMT, the pedestal, pedestal variation, and gain of each channel must be calculated and corrected for. For each pixel, the charge in each pedestal event is determined by summing the waveform data over a given window length and then accumulating these measurements in a histogram, from which the mean pedestal value and RMS value about the mean (*pedvar*) are calculated. To account for varying noise levels over the course of a single data run, this process is repeated for several time slices over the course of the run. The pedestal values may then be subtracted from the summed charges in the real event traces, while the pedvars are recorded as a measure of noise in the system.

The pedestal-subtracted integrated charges are then corrected for relative differences in PMT gains, as measured by the flasher calibration system (Hanna et al., 2010). Every night, the telescopes are directed at patch of dark sky and illuminated by an LED flasher unit located on each telescope's support structure. Each unit consists of seven UV LEDs (peak wavelength of 375 nm) directed through an opal diffuser so that the camera is uniformly illuminated by short ($\sim$ 10 ns) light pulses at 8 light levels, at a rate of 300 Hz, to characterize the PMT responses.

After the application of the above calibrations, a number of pixels may remain with substantial values of integrated charge which are due solely to electron and NSB noise and are not associated with the Cherenkov event. A cleaning procedure is applied to remove these noisy pixels (see Figure 2.3b). The standard cleaning procedure makes use of the signal-to-noise ratio in each pixel, along with the fact that NSB and electronic noise should be randomly distributed across the camera, with no correlation to the location of a given Cherenkov image. Any pixel with integrated charge more than five times its pedestal RMS is called a "picture pixel". Any other pixel that has integrated charge more than 2.5 times the variance and is adjacent to a picture pixel is called a "boundary pixel". Any pixels that are neither picture nor boundary have their integrated charge set to zero. In addition, isolated picture pixels are also set to zero.

2.3.2 Image parameterization

Once an image has been cleaned, the various moments of the light distribution are calculated and combined into Hillas parameters, where the signal within each pixel acts as a weighting factor. These parameters hold information on the geometric properties of the original shower and are used to separate the gamma-ray signal from the cosmic ray background. Treating the image as an ellipse, the most important parameters for use in analysis are:

- *Size*: the sum of all digital counts in the image
- *Length*: approximately the length of the image along the major axis
- *Width*: approximately the length of the image along the minor axis
- *Distance*: the angular distance between the image centroid and the camera center

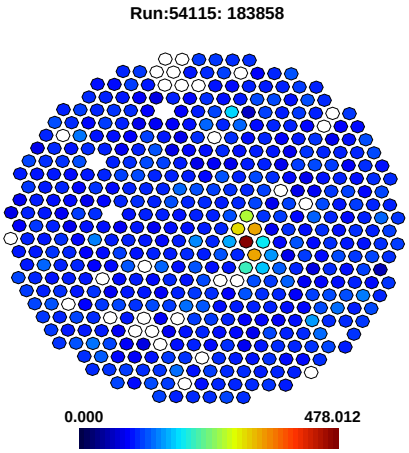

(a) Raw image from a single telescope

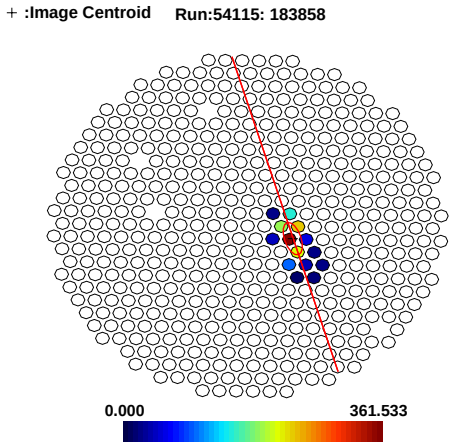

(b) Image after pedestal removal, cleaning, and Hillas parameterization

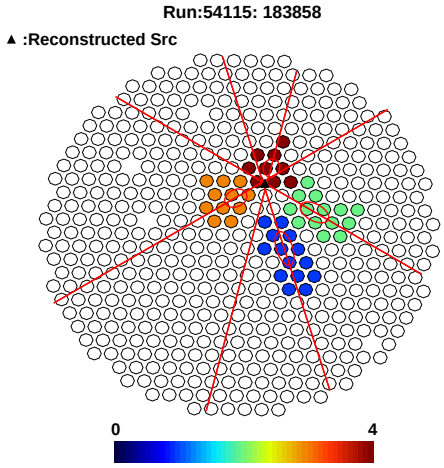

(c) Determination of sky position

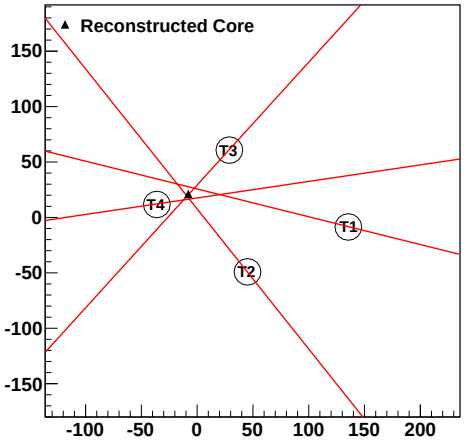

(d) Determination of core impact position

Figure 2.3: Progression of stereoscopic imaging for a gamma-ray-like event. The color scale in images (a) and (b) represent integrated charge in a pixel in digital counts. The color scale in image (c) represents telescope number.

Using i as an index, each PMT has a cleaned signal s_i and is at location (x_i, y_i), where the origin (0, 0) is the camera center. Denoting the moments of arbitrary parameters p and q as

$$\langle pq \rangle = \frac{\sum_i s_i p_i q_i}{\sum_i s_i}, \tag{2.1}$$

and using the definitions

$$\sigma_{x^2} = \langle x^2 \rangle - \langle x \rangle^2 \tag{2.2}$$

$$\sigma_{y^2} = \langle y^2 \rangle - \langle y \rangle^2 \tag{2.3}$$

$$\sigma_{xy} = \langle xy \rangle - \langle x \rangle \langle y \rangle \tag{2.4}$$

$$\lambda = \sqrt{(\sigma_{x^2} - \sigma_{y^2})^2 + 4(\sigma_{xy})^2}, \tag{2.5}$$

the parameters above are then given by

$$\text{Size} = \sum_i s_i \tag{2.6}$$

$$\text{Length} = \left(\frac{\sigma_{x^2} + \sigma_{y^2} + \lambda}{2} \right)^{1/2} \tag{2.7}$$

$$\text{Width} = \left(\frac{\sigma_{x^2} + \sigma_{y^2} - \lambda}{2} \right)^{1/2} \tag{2.8}$$

$$\text{Distance} = \sqrt{\langle x \rangle^2 + \langle y \rangle^2}. \tag{2.9}$$

The major axis is the line which minimizes the weighted sum of the squares of perpendicular distance between itself and the PMTs.

2.3.3 Event reconstruction

By this point, the events have been parameterized on a per-telescope basis. Combining the results from each telescope will yield further information about the shower, and exploits the power of of stereoscopic observations (Hofmann et al., 1999). After cutting

out individual images that suffer from tenuous reconstruction, the arrival direction of the incident gamma ray, the shower core impact location (where the original particle would have reached at ground level in the absence of atmospheric interactions), and the energy of the original air shower are all determined.

Quality Cuts

Before the array-wide imaging can be performed, a set of *quality cuts* must first be made on the data. These cuts allow for more accurate reconstruction of the showers, as the reconstruction methods will use the geometry of the images to determine the origin and trajectory of the original gamma ray, so cutting images with significant sources of parameterization error will improve overall performance. The following cuts are used in the standard analysis (as used here):

- *Minimum Size*: Smaller images are more sensitive to random noise affecting the moment analysis. They may also be less ellipical, increasing the error in the determination of a shower axis. The value of the minimum Size depends upon the suspected spectrum of the source. Harder sources allow for a higher minimum value (and thus a higher threshold energy). Standard values are >400 digital counts for a "moderate" or Crab-like spectrum ($\Gamma \sim -2.5$), and >1000 digital counts for a "hard" spectrum ($\Gamma \sim -2$).

- *Maximum Distance*: Events with centroids near the edge of the field of view may be truncated by the camera edge resulting in errors in the length and orientation, as well as errors in the Size that compromise energy reconstruction. Cuts for a standard moment analysis require Distance $<1^{\circ}.43$.

- *Minimum number of pixels*: Images with only a few cleaned pixels give little information for fitting. At least five pixels are required to pass this cut.

- *Minimum number of telescopes*: The stereoscopic methods described below relies on the pairwise intersection of shower axes to reconstruct various properties of the original shower. While an event with two "good" images, i.e. two images passing criteria described above, will be sufficient, greater accuracy is obtained by the comparison of multiple pairings. It is therefore common to require multiple telescopes for an analysis (> 2), even though this may significantly reduce the available statistics, especially at low energies. For the results discussed here, at least three images are required per event.

Sky Position and Core Impact distance

As the major axis of the Hillas ellipse is a projection of the original shower axis (see Figure 1.5), the direction of origin of the original gamma ray will lie along this axis. However, a single image suffers from a degeneracy in this position, as a simple elliptical fit does not tell on which side of the axis the true position lies.[1] By combining multiple images into a common plane, the intersection of axes from separate images break this degeneracy. (Use of the word "image" refers to a parameterized image in a single telescope which passes each of the quality cuts mentioned above.) If more than two images are used, the process is over-constrained, and appropriately weighted averages of relevant positions will improve the overall estimate.

To measure the arrival direction of the original particle, each image of an event is projected into the same camera field of view (see Figure 2.3c). The direction is then taken as the position which minimizes the total Size-weighted squared perpendicular distance between itself and the major axis of each image. To measure the core impact position, the images are instead projected into the ground plane, at the position of their respective telescopes (see Figure 2.3d). The impact position is again a weighted

[1]The ellipticity and asymmetry of the image can give some information on the proper choice (Fomin et al., 1994), a fact used by the *disp* method of reconstruction, which shows improvement over the methods described here for observations at large zenith angles (LZA) (Beilicke and the VERITAS Collaboration, 2011).

minimization of squared perpendicular distances. The distance between this position and the center of the array is the *core impact distance*.

Energy determination from lookup tables

While the length, width and size of an event may be measured with a moment analysis, the energy of the shower can not be determined from these values alone. Therefore, the expected properties of the showers are determined using Monte Carlo simulations. For these simulations, millions of incident gamma rays from a variety of zenith angles are scattered evenly but randomly over an area around the telescopes, 750 m in radius. The simulated events follow a power-law energy spectrum with photon index -2 over the energy range 50 GeV to 250 TeV. The Cherenkov light from the resulting showers is input to a model of the detector optics and electronics, and the resulting "data" is processed through the same analysis chain as the observational data.

A series of histograms is constructed recording the median shower energy E (or $\log_{10} E$) required to produce an image of a given size at a given core impact distance, thus forming a lookup table. One histogram is produced for each combination of noise level, telescope number, offset between source and the pointing direction, zenith angle, and azimuthal angle, resulting in the production of a 7-dimensional lookup table for the reconstructed energy. Analysis of observational data can then reverse the process, using the size and reconstructed core distance (and other parameters) to interpolate the values of the appropriate table and assign an expected energy for each event. The final determination of the shower energy averages the energy estimates for the good images, weighted by the Sizes.

However, fluctuations in shower development mean that an event of energy E will be reconstructed as energy $E_{rec} = E \pm \epsilon$, giving rise to a distribution of energy residuals $\Delta E = (E_{rec} - E)/E$ versus the true energy, where both the mean value (*energy bias*) and RMS (*energy resolution*) may be energy-dependent. As the true energy of actual

events can not be determined *a priori*, these properties are also measured using the same simulations used to fill the lookup tables. Energies that experience too large of a bias (>0.1) are not used in the spectral reconstruction.

2.3.4 Gamma-hadron separation

With the events now reconstructed, the cosmic-ray showers can be separated from gamma-ray showers. The primary method of separation is through the calculation of the geometric parameters of mean-scaled length (MSL) and mean-scaled width (MSW). Similar to the energy estimation, the measured values of each image in an event will be compared with those found from simulation. Using the same set of processed simulations that were used to create the energy lookup tables, tables are also created for the expected lengths and widths, along with the RMS values. For an observed event with N_{tel} number of telescope images, indexed by i, and with sizes S_i, zenith angles z_i, impact distances d_i, and noise level n_i the mean-scaled length (MSL) and mean-scaled width (MSW) are calculated by

$$MSL = \frac{1}{N_{tel}} \sum_{i=1}^{N_{tel}} \frac{L_i}{L_{sim}(S_i, z_i, d_i, n_i)}, \tag{2.10}$$

$$MSW = \frac{1}{N_{tel}} \sum_{i=1}^{N_{tel}} \frac{W_i}{W_{sim}(S_i, z_i, d_i, n_i)}, \tag{2.11}$$

where L_{sim} and W_{sim} are the expected values of length and width found by interpolation in the appropriate look-up table, derived from simulated data. As the tables are filled with only simulated gamma-ray showers, the distribution in these parameters should peak around 1.0 for actual gamma-ray events. Cosmic-ray events, being broader, should be distributed around larger values.

2.3.5 Source detection

Background Determination

While a significant fraction of cosmic-ray events have been removed from the data by the processes mentioned above, there remains some level of these events which still look like gamma-ray showers. These events are expected to appear isotropically in the sky (after accounting for variation in zenith angle and camera acceptance), so an estimate of their contribution within a source region may be made by subtracting the scaled contribution measured within a separate "background" region. The scaling factor between the signal (ON) region and the background (OFF) region is commonly labeled α, and will account for differences in solid angle Ω, observation time t, and acceptances A for these regions:

$$\alpha = \frac{\int_{on} A_{on}(\Omega, t, z, E) d\Omega \; dt \; dE}{\int_{off} A_{off}(\Omega, t, z, E) d\Omega \; dt \; dE}, \tag{2.12}$$

where z denotes the zenith angle dependence.

For single-telescope instruments such as Whipple, an *ON/OFF* mode was used, wherein centered observations of the source were alternated with observations of a region of empty sky at an identical zenith angle. The background was then assumed to be the same between these observations, after scaling by the time of observation in each position ($\alpha = t_{ON}/t_{OFF}$). The obvious drawback of the ON/OFF method is that only half the observing time is spent with the source in the field of view. Modern instruments instead use a *wobble* method (Fomin et al., 1994). The source is kept within the field of view at all times, but the telescope pointing is offset from its position by a set amount (typically $0°.5$ for *VERITAS*). This method allows for simultaneous measurement of source and background at all times, as well increasing the effective field of observation. The direction of the offset is then alternated between positions north, south, east, and west of the source, so that the same region of the

camera will vary between source and background regions between runs, reducing possible systematic errors.

The source region is defined by θ, the angular distance between the reconstructed event direction and the source of interest. A cut is placed on the maximum squared value of this angle (the θ^2 cut), so that any event within this limit is an "On" event. The exact value of this cut is dependent on the nature of the source. Point-like sources (e.g. sources within the PSF of *VERITAS*, such as the extragalactic blazars) require smaller values of θ^2 (typically $\theta^2 < 0.01$ degree^2) than nearby extended sources, such as supernova remnants (typically $\theta^2 \lesssim 0.04$ degree^2). In all cases, cuts are determined prior to examining the data using either an independent data set or simulations. Since there are several sets of such standard cuts (soft-, medium-, hard-cuts, etc.), if one applies multiple sets of cuts to data, a trials factor is introduced to downgrade the chance probability or significance of the detection.

There are two main choices for background selection used with *VERITAS*: the ring background model and the reflected-region model. For the ring background model, an annulus is constructed around the source position (Figure 2.4a). Any event falling within the annulus is considered an "OFF" event. As the annulus will encompass events at greatly different offsets from the camera center, and and thus at different acceptances, the normalization α is the ratio of the acceptances integrated over the solid angles of the regions.

In the reflected-region model, a series of background regions are constructed with the same size as the On region, but rotated around the point of the telescope pointing for each wobble position (thus "reflected region", see Figure 2.4b). As the background regions are at the same offset in the camera field of view as the source, the acceptance is the same for all regions, and α is simply in the inverse of the number of background regions. This make the reflected-region method preferable for spectral calculations. Note that the construction of the background regions prevents this method from being

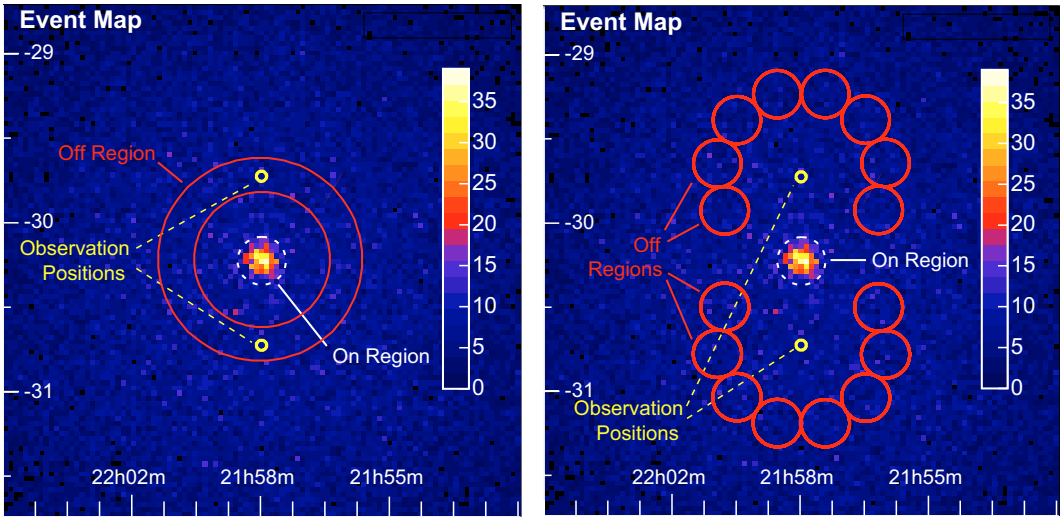

(a) Ring background model (b) Reflected regions model

Figure 2.4: Maps of candidate gamma-ray events from North and South wobble offsets, indicating background regions for the ring background and reflected-region methods, from Berge et al. (2007). The telescope pointings, shown as yellow circles, are offset from the suspected source position, and represent the center of the field of view for that particular run. The "On" region is selected as events with a given radius θ of the source. (a): Background events are taken from an annulus around the source region. (b): Background events are taken from regions of identical size as the On region and at the same offset from the pointing position.

used for any points within a radius θ of the telescope pointing direction.

To prevent actual gamma-ray events from contaminating the background estimation, an exclusion region is drawn around any known source of gamma-ray emission within the field of view, as well as the source under observation. The size of this region will depend on the strength and extension of the object being excluded. Overlap between exclusion regions and background regions must be deducted from the calculation of α. Extra care must be taken for extended objects such as SNRs, where a region of interest must be defined *a priori*. Very extended objects may even necessitate the use of larger wobble offsets than the canonical $0°.5$.

Significance of excess

Given N_{on} counts from the source region, N_{off} counts from the background region, and relative normalization factor α, the frequentist estimates of expected background counts in the signal region is αN_{off} and the number of excess counts is thus

$$N_{excess} = N_{on} - \alpha N_{off}. \tag{2.13}$$

However, the actual background is governed by Poissonian statistics, and an observed excess may simply be a natural fluctuation in the background and not an actual signal from a gamma-ray source. The significance S of a detection is thus taken by comparing the observed excess to the expected fluctuations.

A number of frequentist and Bayesian methods have been developed to determine the significance. The simplest approximate method compares the excess to its own standard deviation:

$$S = \frac{N_{excess}}{\sigma_{excess}} \tag{2.14}$$

$$= \frac{N_{on} - \alpha N_{off}}{N_{on} + \alpha^2 N_{off}}, \tag{2.15}$$

so that the observation is a "S standard deviation result". However, Li and Ma (1983) argued that when comparing against a null hypothesis, so that both N_{on} and N_{off} are purely background, then the measurements of each are connected and a better estimate of the significance would be

$$S = \frac{N_{on} - \alpha N_{off}}{\alpha(N_{on} + N_{off})}. \tag{2.16}$$

Li and Ma went on to derive another more careful estimate using a log-likelihood ratio. If λ is the ratio of the likelihoods of the null hypothesis versus any non-null hypothesis, and the values of N_{on} and N_{off} are not too small, then $-2\ln\lambda$ follows a

χ^2 distribution with one degree of freedom (only the expected value of N_{excess} is being tested). The significance $S = \sqrt{-2 \ln \lambda}$ then follows a Gaussian distribution of mean 0 and standard deviation 1. The full expression for the significance is then

$$S = \sqrt{2} \left(N_{on} \ln \left[\frac{1+\alpha}{\alpha} \left(\frac{N_{on}}{N_{on} + N_{off}} \right) \right] + N_{off} \ln \left[(1+\alpha) \left(\frac{N_{off}}{N_{on} + N_{off}} \right) \right] \right)^{1/2}. \tag{2.17}$$

Equation 2.17 is the standard method of calculating signal significance for TeV astronomy. For *VERITAS*, a significance of $S = 5$ or "5σ" is required for an official source detection. A 2D histogram can also be created of the significance vs position across the entire field of view, creating a sky map.

2.3.6 Spectral reconstruction

If On and Off counts are binned in energy, then the excess counts in each bin can be used to reconstruct the energy spectrum of the source. To extract the intrinsic differential energy spectrum of the source ($\frac{dN}{dE}$, the number of gamma rays per time per area per energy interval), one must take into account the instrument response functions (effective area, energy resolution, etc.) for the specific data analysis chain. The number of excess incident gamma rays measured at a given reconstructed energy, $N_{obs}(E_{rec})$, within an observing time T is given by

$$N_{obs}(E_{rec}) = \int_T dt \int_0^\infty dE \, \frac{dN}{dE} \, A_{eff}(E) \times p(E_{rec}|E) \times \theta(t), \tag{2.18}$$

where $A_{eff}(E)$ is the effective area of the detector at energy E, $p(E_{rec}|E)$ is the probability of reconstructing an event of energy E into energy E_{rec}, and $\theta(t)$ is a factor to correct for the dead-time of the instrument. This integral can be directly applied for model comparison (the forward folding technique), but often it is desirable

to extract a model-independent estimate of the source spectrum $\frac{dN}{dE}$. This requires an inversion of the integral and introduces some inevitable complications due to the presence of measurement error in $N_{obs}(E_{rec})$.

The effective area A_{eff} is determined using the same simulation and analysis chain previously used to construct lookup tables for event reconstruction. As describe above, millions of events from a given zenith angle are scattered evenly but randomly over an area A_{thrown} around the telescopes, where A_{thrown} has a radius of 750 m, with a simulated power-law spectrum of photon index -2. The events are run through the detector model and the same analysis cuts are applied as in the analysis of the data set. If a number $N_{cuts}(E)$ events of energy E pass these cuts, out of an original $N_{thrown}(E)$ events, then the effective area is

$$A_{eff}(E) = \frac{N_{cuts}(E)}{N_{thrown}(E)} A_{thrown}. \tag{2.19}$$

This process is repeated for different combinations of zenith angle, noise level, atmospheric model, and angular offset between the source and the telescope pointing.

Unfortunately, the imperfect energy resolution of the instrument, represented by the $p(E_{rec}|E)$ term of Equation 2.18 means that the exact shape of an effective area curve will depend upon the assumed spectrum of the source. As mentioned in Section 2.3.2, fluctuations in shower development result in misconstructed energies for individual events. For a steeply falling spectra, this means that, above the threshold energy, there will a systematic excess of low-energy events fluctuating up into a given energy bin compared to high-energy events fluctuating downward (as there are fewer high-energy events to begin with), which will affect the effective area construction. This effect is accounted for by weighting the original effective area to form new

effective areas $\tilde{A}_{\mathit{eff}}$. The source spectrum can be calculated by

$$\frac{dN}{dE}(E) = \frac{N_{obs}(E)}{T_{corr}\ \tilde{A}_{\mathit{eff}}(E)\ dE}, \tag{2.20}$$

where T_{corr} is the dead-time corrected observation time. If the fitted index of the resulting spectrum doesn't match that assumed in generating the weighted effective areas, a new weighting index is chosen, a new set of $\tilde{A}_{\mathit{eff}}$ are created, and the process is repeated until the values converge. For analysis with multiple runs, which may need different effective areas due to changes in zenith angle, noise, etc., Equation 2.20 becomes a sum over N_{obs} from each run, with the live-time and effective areas acting as a weighting factor:

$$\frac{dN}{dE}(E) = \frac{\sum_{i=0}^{n} N^{i}_{obs}(E)}{\sum_{i=0}^{n} T^{i}_{corr}\ \tilde{A}^{i}_{\mathit{eff}}(E)\ dE}, \tag{2.21}$$

Chapter 3

Introduction to pulsar wind nebulae

3.1 Pulsars

Starting with their discovery by Hewish and Bell in 1967, the number of know pulsars have grown to approximately 2000, as listed in the ATNF pulsar catalog (Manchester et al., 2005)[1]. These objects were quickly explained to be rapidly rotating neutron stars (Gold, 1968; Pacini, 1968), the compressed cores of dead stars. While the eponymous pulsed emission is now detectable from radio to TeV energies (VERITAS Collaboration et al., 2011), a majority of the energy output by the pulsar goes into an ultrarelativistic magnetized particle wind, which eventually forms an extended region of emission, called a *pulsar wind nebula* (PWN). These objects have themselves been observed across all wavebands, including the prototypical example of the Crab Nebula. This section will discuss the properties of pulsars relevant to the production of PWNe, a description of PWN formation and evolution, and some comments on TeV observations of these objects.

[1] http://www.atnf.csiro.au/people/pulsar/psrcat/

3.1.1 Pulsar formation

As a star reaches the end of its main sequence lifetime, the hydrogen at the core is depleted and the rate of nuclear fusion decreases, leaving behind heavier nuclei. As fusion slows, the internal thermal pressure decreases and the core contracts. The pressure and temperature increase until the core reignites with helium-fusion, with hydrogen-burning occurring in a surrounding shell. As the helium is eventually depleted, the star collapses again until fusion of carbon begins. The cycle of fusion and collapse continues for progressively heavier elements (C, Ne, O, Si) so that the the star obtains an onion-like structure, with fusion of heavy elements at the core surrounded by multiple layers burning the lighter elements. The final achievable reaction is dependent upon the star's initial mass, with an absolute limit occurring at the island of stability at iron.

For massive stars ($M \gtrsim 10M_{\odot}$), the end of fusion leads to a collapse which can result in a Type II supernova. As the core collapses, it undergoes photodisintegration and electron capture while the equation of state stiffens due to electron- and then neutron-degeneracy pressure. The remaining infalling matter rebounds off the core, driving a shock wave into stellar envelope. As this blast wave is further energized by a pulse of neutrinos from the core, it expels the outer layers of the star with $\sim 10^{51}$ ergs of kinetic energy ($\sim 1\%$ of the total available energy) and drives a shock into the surrounding medium while leaving behind a neutron star.

While the exact fate of a given star will depend upon factors such as the history of its mass-loss rate, metallicity, and the presence of a companion star, Ghosh (2007) offers the following generalization:

Stars with mass <8 $\mathbf{M}_{\odot}$

Outer envelope expands into a planetary nebula and core collapses to a white dwarf, supported by electron degeneracy pressure.

11–25 $M_\odot$

Collapse results in a supernova, with the core ending as a neutron star, supported by neutron degeneracy pressure.

$\gtrsim$25 $M_\odot$

Collapse results in a supernova, with the core collapsing directly into a black hole.

Stars in the transition regime of 8–11 $M_\odot$ may become either a white dwarf or neutron star, depending on the sequence of fusion at their core.

After the supernova, a neutron star is expected to possess a complicated internal structure, a surface temperature of $\sim 10^6$ K, a radius of $\sim$10 km, and a mass $\sim$1–2 $M_\odot$. The conservation of angular momentum during the collapse for the original core results in rapid spin rates, with initial periods of rotation on the order of a few seconds or less. As the original magnetic fields are frozen into the ionized plasma during the collapse, the seed fields of the original star are magnified to $10^{10} - 10^{13}$ G (Longair, 1994). The corotating field is filled with a complicated magnetosphere of charged plasma which may contain regions of depleted charge (or "gaps") where large potentials may be established (see Sections 3.1.4 and 3.1.5 for more details). These potentials will accelerate particles to ultra-high energies, which then produce beams of emission. If the magnetic axis is misaligned to the spin axis, and an observer is within the area swept out by the beam as neutron star rotates, the object is then visible as a pulsar.

3.1.2 Spin-down luminosity and characteristic age

As a rotating magnetic dipole, a pulsar will emit both dipole radiation and a relativistic wind of electron-positron pairs (see Sec. 3.2). The energy for these two features comes at the expense of the pulsar's rotational kinetic energy $E_{rot} = \frac{1}{2} I \Omega^2$, where Ω

is the pulsar angular frequency and I is the moment of inertia, typically taken to be $\sim 10^{45}$ g cm^2 for a 1.4 solar mass star with a radius 10 km. This energy loss is called the spin-down power or spin-down luminosity

$$\dot{E} \equiv -\dot{E}_{rot} = -I\Omega\dot{\Omega} = 4\pi^2 I \frac{\dot{P}}{P^3} \tag{3.1}$$

with P the pulsar's period of rotation.

Due to the energy loss, the pulsar spin-down rate will not remain constant, but in the simplest approximation may scale by some braking index n:

$$\dot{\Omega} = -k\Omega^n, \text{ or equivalently, } \dot{P} \propto P^{2-n}, \tag{3.2}$$

with k assumed to be a positive constant. For radiation from a pure magnetic dipole, $n = 3$, while higher multipole moments and plasma interactions may generate torques with indices of 1 to 2 (Ghosh, 2007). Measuring the braking index requires a measurement of both the first and second time derivatives of Ω, as $\ddot{\Omega} = -nk\Omega^{n-1}\dot{\Omega} = n\dot{\Omega}^2/\Omega$. Such measurements are difficult for two reasons: first, they require sensitive timing observations over long periods. Second, pulsars can experience a range of timing noise, including sudden jumps in Ω and $\dot{\Omega}$ called "glitches", resulting from angular momentum transfer between the pulsars outer crust and a superfluid interior (Anderson and Itoh, 1975) (although stresses from accretion have also been suggested (Morley, 1996)). As a result, confident estimates of n exist for only about 5 pulsars, with $2 < n < 3$ (Livingstone et al., 2007).

Integrating Equation 3.2 from the birth of the pulsar to the time t, one sees that the spin period evolves as

$$P(t) = P_0 \left(1 + \frac{t}{\tau_0}\right)^{1/(n-1)}, \tag{3.3}$$

where τ_0 is the spin-down time,

$$\tau_0 = \frac{P_0}{(n-1)\dot{P}_0} \tag{3.4}$$

and P_0 and $\dot{P}_0$ are the initial values of the period and its time-derivative. As the spin period changes with time, so does the spin-down power:

$$\dot{E}(t) = \dot{E}_0 \left(1 + \frac{t}{\tau_0}\right)^{-(n+1)/(n-1)}. \tag{3.5}$$

If P and $\dot{P}$ are the values measured at the current time, rearranging Equation 3.3 yields the pulsar age T as

$$T = \frac{P}{(n-1)\dot{P}} \left[1 - \left(\frac{P_0}{P}\right)^{n-1}\right]. \tag{3.6}$$

Assuming that $n = 3$ and $P_0 \ll P$, we define the characteristic age of the pulsar

$$\tau_C \equiv \frac{P}{2\dot{P}}. \tag{3.7}$$

We can then express the spin-down age as

$$\tau_0 = \frac{2\tau_C}{n-1} - T. \tag{3.8}$$

Note that if P_0 is not much less than P, the characteristic age will be an overestimate of the true age. For example, the charactistic age of the pulsar in the Crab Nebula is $\sim$ 1240 yr, while the historical age is known from Chinese records to be $\sim$ 958 yr (Stephenson and Green, 2002).

3.1.3 Magnetic field

As mentioned above, pulsars possess a large magnetic field. If the magnetic dipole moment $\vec{\mu}$ forms an angle α with the axis of rotation, the normal component of the moment $\mu_\perp \equiv \mu \sin\alpha$ will rotate with angular frequency Ω. Following the form of Landau and Lifshitz (1975), the resulting power loss due to dipole radiation is

$$\dot{E}_{dip} = -\frac{2\Omega^4 \mu_\perp^2}{3c^3} \tag{3.9}$$

$$= -\frac{32\pi^4 \mu^2 \sin^2\alpha}{3c^3 P^4}. \tag{3.10}$$

Setting this power equal to the spin down power of Equation 3.1, we obtain

$$\mu^2 = \frac{3Ic^3 P\dot{P}}{8\pi^2 \sin^2\alpha}. \tag{3.11}$$

Approximating the magnetic moment as $\mu = BR^3$, where B is the average magnetic field at the pulsar surface,

$$B^2 = \frac{3Ic^3}{8\pi^2 R^6 \sin^2\alpha} P\dot{P}. \tag{3.12}$$

We can then set an approximate lower limit for the strength of the field (using $\sin\alpha = 1$) of

$$B \approx 3.2 \times 10^{19}\ (P\dot{P})^{1/2}\ G, \tag{3.13}$$

with P measured in sec and $\dot{P}$ in sec/sec. Inferred values of the magnetic field strength range from $< 10^8$ G to $> 10^{15}$ G, with typical values $10^{11} - 10^{13}$ G (see Figure 3.1).

3.1.4 Magnetosphere and light cylinder

Goldreich and Julian (1969) first realized that a rotating, magnetic, highly-conductive neutron star can not exist *in vacuo*. The rotation of the star will cause any charges inside the star to separate so as to create an electric field (as seen in an inertial frame)

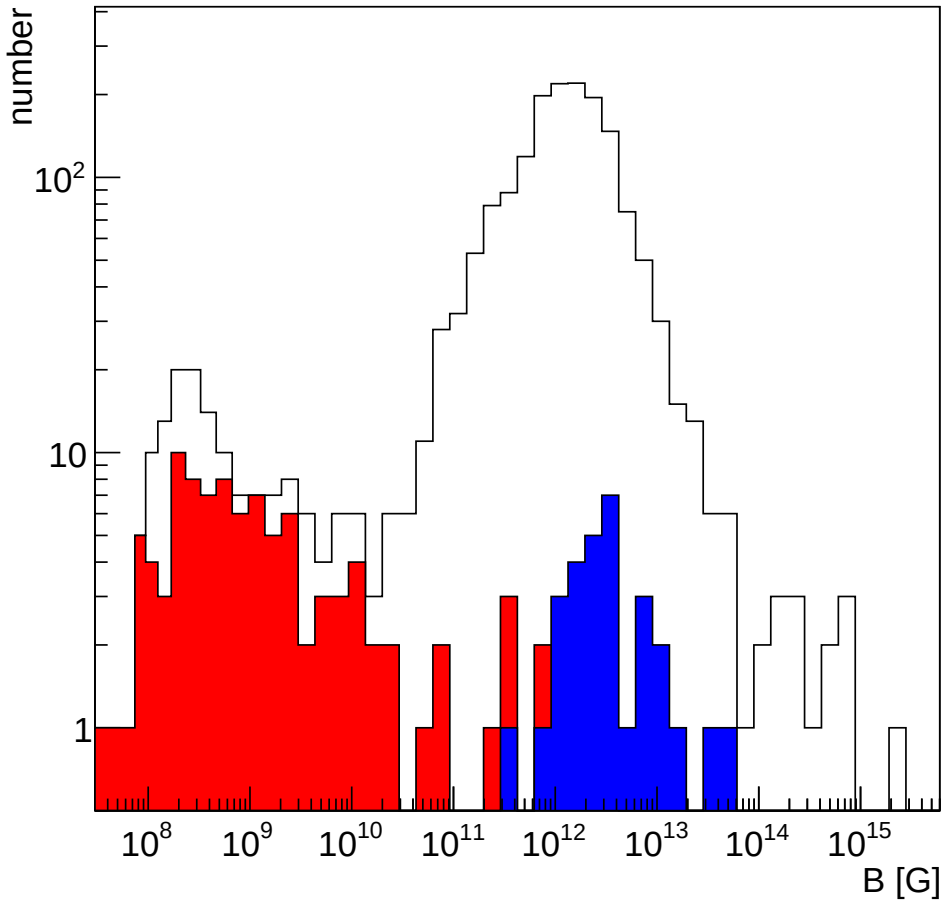

Figure 3.1: Histogram of surface magnetic field (in Gauss) for pulsars in the ATNF catalog. Binary pulsars are marked in red. Pulsars with TeV-detected PWNe (see Table 3.1) are marked in blue.

which cancels the force from the magnetic field, so that

$$\vec{E} + \frac{\vec{\Omega} \times \vec{r}}{c} \times \vec{B} = 0. \tag{3.14}$$

The electric field outside the pulsar has a component along the direction of the magnetic field

$$E_{||} = \frac{\Omega R}{c} \left(\frac{R}{r}\right)^7 B_0^2 \cos^3\theta, \tag{3.15}$$

where B_0 is the strength of the magnetic field at the poles and θ is the polar angle. At the surface of the pulsar, the electric force on an electron from this component will exceed the gravitational force in the same direction by many orders of magnitude:

$$\begin{aligned} \frac{e\vec{E} \cdot \vec{B}}{\vec{F}_g \cdot \vec{B}} &= \frac{e\Omega R^3 B_0}{GMm_e c} \cos^2\theta \\ &\approx 8 \times 10^{11} \left(\frac{B_0}{10^{12}\ \mathrm{G}}\right) \left(\frac{1\ \mathrm{s}}{P}\right) \cos^2\theta. \end{aligned} \tag{3.16}$$

At the appropriate latitudes, this force imbalance will be directed radially outward, stripping charges from the pulsar surface. These charges will distribute themselves to short any electric fields, forming a magnetosphere around the pulsar. The charge density of the magnetosphere will approach the Goldreich-Julian density:

$$\rho_{GJ} = \frac{-\vec{\Omega} \cdot \vec{B}}{2\pi c[1 - (\Omega r/c)^2 \sin^2\theta]}. \tag{3.17}$$

There is evidently a surface which separates positively and negatively charged regions, called the null-charge surface, defined by the condition $\vec{\Omega} \cdot \vec{B} = 0$. Charges of one sign will cluster near the poles, while charges of the opposite sign will cluster in the equatorial regions. This magnetosphere will corotate with the pulsar out to a distance from the spin axis where the tangential velocity would equal the speed of light. This distance, $R_{LC} = cP/2\pi$, defines the *light cylinder*, outside of which corotation is

forbidden and the dipole-like field structure and the wind must be modified.

3.1.5 Vacuum gaps and particle acceleration

By causality, magnetic field lines may not close outside the light cylinder; any that cross the light cylinder radius are therefore called open field lines. Charges may flow along these open field lines to escape the magnetosphere. A decrease in charges from a region (a "gap") may allow for $\vec{E} \cdot \vec{B} \neq 0$ within the region, and particles may be accelerated by this non-zero electric field as they slide along field lines. The maximum potential drop available for acceleration in an aligned rotator was calculated by Goldreich and Julian (1969) to be

$$\Delta\Phi = \frac{2\pi^2 R^3 B_0}{P^2 c^2} \tag{3.18}$$

$$\approx 6.6 \times 10^{12} \left(\frac{B_0}{10^{12}\ \mathrm{G}}\right) \left(\frac{P}{1\ \mathrm{s}}\right)^{-2}\ \mathrm{V} \tag{3.19}$$

There are three main models for where these vacuum gaps are created. In polar cap models, two regions form near the neutron star surface along the magnetic field axis. In outer gap models, regions form in the outer magnetosphere, bounded by the light cylinder surface, the null-charge surface, and the last closed line. In slot gap models, the regions form between the first open field line and the last closed line, near the polar cap. Regardless of the true location of the vacuum gaps, the particles accelerated within them will radiate via synchrotron, inverse Compton, or curvature radiation (see Section 1.1). The resulting photons can pair produce on ambient photons (or on the virtual photons of the magnetic field close to the pulsar surface), creating new e^-/e^+ pairs. The formation of these pairs will help replenish the depletion regions, limiting the growth of the vacuum gaps (Cheng et al., 1986).

3.2 Formation of a pulsar wind nebula

The magnetic field and charged particles escaping from the light cylinder form a magnetized, ultrarelativistic wind. If the pulsar's magnetic axis is inclined with respect to its spin axis (an "oblique rotater"), the equitorial region of the wind will take on a striped pattern, with successive regions of alternating magnetic polarity, separated by a current sheet. The energy balance of the wind is often characterized by σ, the ratio of electromagnetic energy flux to the particle energy flux:

$$\sigma = \frac{B^2}{4\pi\Gamma^2\rho c^2}, \tag{3.20}$$

where Γ is the bulk Lorentz factor of the wind and ρ is the proper mass density. The so-called "σ problem" of PWNe, first noted in the Crab Nebula (Kennel and Coroniti, 1984), arises from the discrepancy between estimates of σ at varying distances from the pulsar light cylinder. Models of pulsar magnetospheres predict Poynting dominated winds, with $\sigma \gg 1$. However, further from the pulsar the wind must be dominated by kinetic energy, $\sigma \ll 1$, to match the expansion of the larger nebula. Therefore, somewhere within the wind, the majority of energy must be transfered from the fields to the particles. The mechanism for this transfer is as yet unknown, although some schemes such as magnetic reconnection have been suggested (e.g., Pétri and Lyubarsky, 2008, and references therein).

As the pulsar wind expands into the SNR, it is confined by surrounding, slowly-moving ejecta and decelerated. As the pressure of this confined material increases, a termination shock is established at a radius, R_{TS}, where the internal pressure of the PWN, $\mathcal{P}_{\mathcal{N}}$, balances the ram pressure of the relativistic wind flowing from the pulsar:

$$R_{TS} = \sqrt{\frac{\dot{E}}{4\pi\xi c\mathcal{P}_{\mathcal{N}}}}, \tag{3.21}$$

where, ξ is the filling factor of the wind ($\xi = 1$ for an isotropic wind). At the shock, the spin-down luminosity is divided between particle and magnetic energy fluxes as

$$\dot{E} = 4\pi R_{TS}^2 \Gamma^2 \rho m c^3 (1 + \sigma). \tag{3.22}$$

Alternatively, this can be expressed as a combination of luminosities of the various components:

$$\dot{E}_B = \eta_B \dot{E} \tag{3.23a}$$

$$\dot{E}_E = \eta_E \dot{E} \tag{3.23b}$$

$$\dot{E}_I = \eta_I \dot{E} \tag{3.23c}$$

where the subscripts B, E, and I correspond to the magnetic, electron pair, and ionic components of the wind, respectively, and with $\eta_B + \eta_E + \eta_I = 1$. This formulation is related to the σ of Kennel and Coroniti by

$$\sigma = \frac{\eta_B}{\eta_E + \eta_I}. \tag{3.24}$$

Upstream of the shock, particles flow along field lines and don't radiate. As particles cross the shock, they will be scattered one or more times and may undergo first-order relativistic Fermi acceleration. Due to the scattering, the particles will no longer slide along field lines and may obtain a non-zero pitch angle, making them emit synchrotron and IC radiation and creating the observable PWN. The shock can accelerate particles to very high energies, although compared with strong nonrelativistic shocks (which produce a canonical $E^{-2.0}$ power-law spectrum) the efficiency of injection and the resulting spectral index from such relativistic shocks are less well understood. These parameters appear to depend on numerous factors such as magnetic field obliquity with respect to the shock normal and strength of the magnetic

turbulence (Baring, 2011).

3.3 Evolution of pulsar wind nebulae

After the initial formation, PWNe go through several stages of evolution, which depend on the properties of both the parent pulsar and the surrounding medium (SNR ejecta or ISM) as well as interactions with the SNR shock. A general overview of this progression is given by Gaensler and Slane (2006).

3.3.1 Young PWNe

Using the results of Truelove and McKee (1999), the outer blast wave of an SNR in the free expansion phase initially moves outward with a velocity of

$$v_{\rm SNR}(t) = 0.75 \frac{R_{\rm ch}}{t_{\rm ch}} \left(\frac{t}{t_{\rm ch}} \right)^{-1/3}, \tag{3.25}$$

where we use the characteristic distance and time:

$$R_{\rm ch} = (M_{\rm ej}/\rho_{\rm ISM})^{1/3}, \tag{3.26}$$

$$t_{\rm ch} = E_{\rm SN}^{-1/2} M_{\rm ej}^{5/6} \rho_{\rm ISM}^{-1/3}, \tag{3.27}$$

with $E_{\rm SN}$ the kinetic energy of the supernova, M_{ej} the total mass of the supernova ejecta, and $\rho_{\rm ISM}$ the constant mass density of the surrounding ISM. For young SNRs, this will be $> (5 - 10) \times 10^3$ km s^{-1} (Gaensler and Slane, 2006). Meanwhile, asymmetry in the supernova explosion will impart a kick velocity to newly created pulsar. Measured values of these velocities are typically in the range of a few hundred km s^{-1} (Hobbs et al., 2005). Therefore the pulsar remains near the center of the remnant at early times.

The pulsar wind downstream of the termination shock will be supersonic compared

to the sound speed of the cold ejecta and will drive a forward shock outward. For a radially symmetric SNR-PWN system with freely expanding SNR ejecta of a constant density and a linear velocity profile, van der Swaluw et al. (2001) found that the radius of the PWN forward shock is given by

$$R_{\rm PWN}(t) = K\dot{E}_0^{1/5} E_{\rm SN}^{3/10} M_{\rm ej}^{-1/2} t^{6/5}, \tag{3.28}$$

where K is a constant of order unity and $\dot{E}_0$ is the constant luminosity of the pulsar (valid for $t \ll \tau_0$). The $t^{6/5}$ scaling was reproduced by their hydrodynamic simulations, and confirmed the findings of previous authors (e.g. Reynolds and Chevalier, 1984). Scaling to typical values of the parameters,

$$R_{\rm PWN}(t) = 1.1 \left(\frac{\dot{E}_0}{10^{38}\ {\rm erg/s}}\right)^{1/5} \left(\frac{E_{\rm SN}}{10^{51}\ {\rm erg}}\right)^{3/10} \left(\frac{M_{\rm ej}}{M_\odot}\right)^{-1/2} \left(\frac{t}{1\ {\rm kyr}}\right)^{6/5}\ {\rm pc}. \tag{3.29}$$

Due to the increasing PWN radius and the high sound speed for the relativistic gas inside the nebulae, the PWN remains centered on the pulsar at this stage. The nebula may appeared elongated along the spin axis of the pulsar due to magnetic pressure from a toroidal magnetic field (van der Swaluw, 2003). Rayleigh-Taylor instabilities may also form filamentary structures inside the nebulae.

3.3.2 Crushed and relic PWNe

As the expanding supernova ejecta encounters the downstream region of the forward shock, it encounters the shocked ISM is rapidly decelerated, forming a reverse shock. This reverese shock is separated from the forward shock by a contact discontinuity between shocked ejecta and shocked ISM. While the reverse shock initially expands outward behind the forward shock, it may eventually move inward, with the exact behavior of the reverse shock and subsequent reverberations depending on the structure of the SNR ejecta and the surrounding medium. The remnant only enters the self-

similar Sedov-Taylor phase once the reverse shock and subsequent secondary shocks subside (Truelove and McKee, 1999).

Assuming an ambient medium of constant number density n_0 surrounding the SNR, a spherical reverse shock will reach the edge of a centered PWN in a time (Reynolds and Chevalier, 1984)

$$t_{\rm col}(t) \approx 7 \left(\frac{M_{\rm ej}}{10\ M_\odot}\right)^{5/6} \left(\frac{E_{\rm SN}}{10^{51}\ {\rm erg}}\right)^{-1/2} \left(\frac{n_0}{1\ {\rm cm}^{-3}}\right)^{-1/3}\ {\rm kyr}. \tag{3.30}$$

. A significant pulsar velocity will decrease this collision time. As the reverse shock compresses the PWN, the magnetic field strength greatly increases, causing the highest energy particles to rapidly burn off via synchrotron cooling, dramatically increasing the X-ray brightness of the system. The increasing pressure leads to a sudden rebound and expansion, starting a series of reverberations over a several thousands of years. In addition, the kick velocity of the pulsar, combined with any asymmetry in the propagation of the reverse shock, can cause the pulsar to escape from its original nebula, creating a *relic nebula*. As the pulsar is separated from the original PWN and therefore no longer injects new, high-energy particles into the nebula, these objects will be appear as extended radio/TeV sources with little X-ray emission, offset from the parent pulsar although possibly connected by a radio and X-ray bridge. Meanwhile the pulsar can create a new PWN around its current position, although the new PWN will not expand supersonically as the original one did, as the sound speed within the shocked (hot) ejecta is $\sim c/\sqrt{3}$.

3.3.3 Bow shock nebulae

If the pulsar has a high kick velocity, as the pulsar approaches the edge of the remnant, the local sound speed drops so that the pulsar and its wind are moving supersonically. If the remnant is still in the Sedov phase, this transition occurs at a distance 68% of

the way from the remnant center to the forward shock (van der Swaluw et al., 2004). The pulsar will also travel supersonically when it eventually crosses the forward shock of the SNR and enters the interstellar gas.

The pair wind from the pulsar is now decelerated at a termination shock confined by ram pressure, rather than the internal pressure of the PWN. This ram pressure is not isotropic, so that the distance between the shock and the pulsar varies with the polar angle from the direction of the pulsar's motion. For an isotropic wind forming a single, thin shock, the shock radius scales as

$$R_w(\theta) = R_0 \csc\theta \sqrt{3(1 - \theta \cot\theta)}, \tag{3.31}$$

with the stand-off distance R_0 given by

$$R_0 = \left(\frac{\dot{E}}{4\pi \rho_0 V^2 c} \right)^{1/2}, \tag{3.32}$$

where V the pulsar velocity and ρ_0 is the mass density of the surrounding gas. Detailed magnetohydrodynamic (MHD) simulations show a more complex, double shock structure (see Figure 3.2), with Equation 3.31 only valid for angles $\theta < \frac{\pi}{2}$, and the shock radius at large θ approaching a limit of $\sim 5-6R_0$ (see, for example, Bucciantini et al., 2005; van der Swaluw et al., 2003).

The shocked wind and ISM material flowing away form the termination shock is confined into a collimated tail behind the pulsar, so that the nebulae assumes a cometary appearance. The synchrotron nebula may be visible from radio to X-rays (see Figure 3.3 for an example), while Hα emission can be seen from shocked ISM. No pulsar tail has been observed at TeV energies.

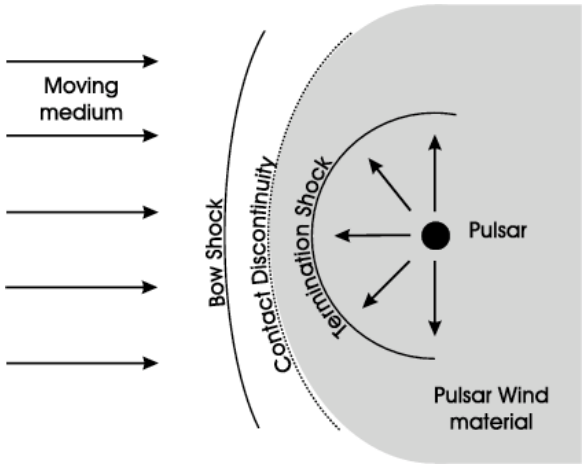

Figure 3.2: Diagram of a bow-shock PWN moving through a uniform medium, as seen in the rest frame of the pulsar. In the lab frame the pulsar would be moving to the left. Figure taken from van der Swaluw et al. (2003)

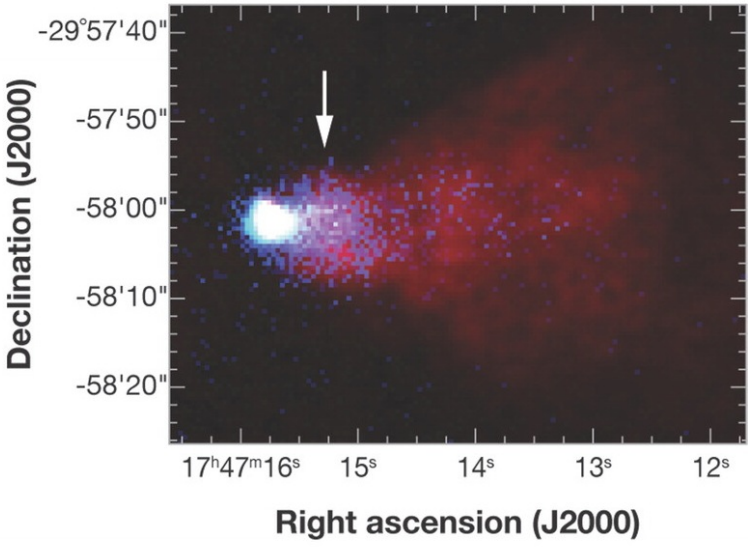

Figure 3.3: Image of G359.23–0.82 ("the Mouse"), the bow shock associated with PSR J1747-2958, at two energies: X-ray (blue, *Chandra*) and radio (red, VLA). Figure taken from Gaensler and Slane (2006).

3.3.4 Ghost nebulae

As the pulsar continues to travel through the ISM, its age grows much greater than its spin-down time τ_0, and its $\dot{E}$ steady drops. The energy injected into the nebula becomes insufficient to power observable emission, and the surrounding bubble of relativistic material becomes confined by the ISM thermal pressure at a distance $\gg 1$ pc, forming a *ghost nebula* (Blandford et al., 1973). No detection of these objects have been reported.

3.4 TeV emission from PWNe

The emission of TeV gamma rays from pulsar wind nebulae is commonly explained as the inverse Compton scattering of ambient photon fields by the relativistic electrons of the shocked wind. For most PWNe, the seed photons originate from outside the nebula, such as the CMB or local optical and IR fields. In the Crab Nebula, the electron population scatter the same synchrotron photons it emits at lower (radio to X-ray) energies. In addition to the standard leptonic scenario, any hadronic component of the pulsar wind may contribute to the TeV emission through the production of neutral pions, if the wind impacts a dense ambient medium such as the outer SNR shell.

As of July 2012, more than 30 PWNe have been detected at TeV energies, while several other TeV sources are considered candidate PWNe. Some objects have been identified through associations and positional coincidence with PWNe known at other wavelengths with better angular resolution (e.g. radio, X-ray). However, others are seen only in VHE gamma-rays, with their designation based upon positional coincidence with a nearby pulsar and spectral/morphological similarities with more well-known PWNe. Table 3.1 lists those PWNe and PWNe candidates detected at TeV energies that also have an associated pulsar with measured spin properties. In addi-

tion, several unidentified TeV objects (the second largest class at Galactic latitudes), also exhibit such similarities and may be also be PWNe, even though the parent pulsar is not observed. Often a definitive identification of a TeV source with a PWN is difficult due to other potential sources (e.g. the SNR shell itself) and the possibility of multiple SNRs falling along the line of sight in some particularly crowded parts of the galaxy (e.g. tangent to a spiral arm).

While most PWNe and PWNe candidates are located towards the inner Galaxy and are therefore only observable by instruments in the Southern hemisphere (i.e. *HESS*), numerous sources have been identified by Northern observatories as well. These sources generally have the advantages of lower background light and less source confusion, making for easier detection and identification. Table 3.1 lists PWN candidates detected by all TeV instruments (*HESS*, *VERITAS*, and *MAGIC*).

Table 3.1: Pulsar wind nebulae and PWN candidates detected at TeV energies with associated pulsars. Data from Kargaltsev and Pavlov (2010) and TeVCat (Wakely and Horan, 2012), except the properties of PSR J0537-6910, which are from the ATNF catalog. Pulsars marked with * are tenuous. Note that TeV objects identified as PWNe through other associations (e.g. located within a SNR) but without a detected pulsar are not listed.

PWN name	Pulsar	dist [kpc]	P [ms]	$\log \tau_C$ [yr]	$\log \dot{E}$ [erg/s]
CTA 1	J0007+7303	1.4	315.86	4.14	35.36
Crab	J0534+2200	2	33.08	3.09	38.66
N 157B	J0537-6910	48	16.12	3.69	38.69
Geminga	J0633+1746	0.250	237.10	5.53	34.51
Vela X	J0834-4511	0.29	89.33	4.05	36.84
HESS J1023-575	J1022-5746	8	111.47	3.7	37.0
HESS J1026-582	J1028-5819	2.3	91.40	4.9	35.9
G292.2-0.5	J1119-6127	5	407.75	3.21	36.37
HESS J1303-631	J1301-6305*	7	184.52	4.04	36.22
HESS J1356-645	J1357-6429	2.5	166.11	3.86	36.49
Kookaburra (Rabbit)	J1418-6058	5.6	110.57	4.00	36.69
Kookaburra (PWN)	J1420-6048	5.6	68.18	4.11	37.02
MSH 15-52	J1513-5908	5.2	150.66	3.19	37.25
HESS J1616-508	J1617-5055*	6.5	69.36	3.91	37.20
HESS J1708-443	J1709-4429	2.3	102.46	4.24	36.53
HESS J1718-385	J1718-3825*	4.2	74.67	4.95	36.11
G0.9+0.1	J1747-2809	8.5	52.15	3.73	37.6
HESS J1809-193	J1809-1917	3.71	82.75	4.71	36.25
HESS J1813-178	J1813-1749*	4.7	44.70	3.66	37.83

Continued on next page

Table 3.1 – continued from previous page

PWN name	Pulsar	dist [kpc]	P [ms]	$\log \tau_C$ [yr]	$\log \dot{E}$ [erg/s]
HESS J1825-137	J1826-1334	3.9	101.49	4.33	36.45
HESS J1833-105	J1833-1034	4.8	61.87	3.69	37.52
HESS J1837-069	J1838-0655	7	70.50	4.36	36.74
Kes 75	J1846-0258	6.3	325.68	2.86	36.91
IGR J18490-0000	J1849-0001	7	38.52	4.6	37.0
HESS J1857+026	J1856+0245	9	80.90	4.32	36.66
HESS J1912+101	J1913+1011	4.48	35.91	5.23	36.46
G54.1+0.3	J1930+1852	6.2	136.86	3.46	37.06
MGRO J2019+37	J2021+3651*	4	103.74	4.23	36.53
TeV J2032+4130	J2032+4127	1.7	143.25	5.04	35.43
Boomerang	J2229+6114	0.8	51.16	4.02	37.35

Chapter 4

Discovery of TeV Gamma-ray Emission from CTA 1 by VERITAS

This chapter contains a late draft of the paper "Discovery of TeV Gamma-ray Emission from CTA 1 by VERITAS", detailing the initial TeV observations of the SNR CTA 1, containing the GeV pulsar PSR J0007+7303, along with some interpretation of the observed emission in the context of a PWN.

4.1 Abstract

We report the discovery of TeV gamma-ray emission coincident with the shell-type radio supernova remnant (SNR) CTA 1 using the *VERITAS* gamma-ray observatory. The source, VER J0006+729, was detected as a 6.5 standard deviation excess over background and shows an extended morphology of dimensions $0°.30 \times 0°.24$, with a centroid $5'$ from the Fermi gamma-ray pulsar PSR J0007+7303 and its X-ray pulsar wind nebula (PWN). The photon spectrum is well described by a power-law $dN/dE = N_0(E/3\ \mathrm{TeV})^{-\Gamma}$, with a differential spectral index of $\Gamma = 2.2 \pm 0.2_{\mathrm{stat}} \pm 0.3_{\mathrm{sys}}$, and

normalization $N_0 = (9.1 \pm 1.3_{\rm stat} \pm 1.7_{\rm sys}) \times 10^{-14}$ cm^{-2} s^{-1} TeV^{-1}. The integral flux, $F_\gamma = 4.0 \times 10^{-12}$ erg cm^{-2} s^{-1} above 1 TeV, corresponds to 0.2% of the pulsar spin-down power at 1.4 kpc. The energetics, co-location with the SNR, and the relatively small extent of the TeV emission strongly argue for the PWN origin of the TeV photons. We consider the origin of the TeV emission in CTA 1.

4.2 Introduction

There are many possible associations of gamma-ray sources with supernova remnants (SNRs). These gamma rays could come from shock acceleration in the shell, a pulsar associated with the SNR, or a pulsar wind nebula (PWN) surrounding the pulsar. Such gamma-ray/SNR associations date back to *COS B* observations of SNRs coincident with OB stellar associations (Montmerle, 1979). Observations of the Galaxy by *EGRET* in the energy range 30 MeV–30 GeV revealed $\sim$ 19 unidentified sources at low Galactic latitudes that were found to be spatially correlated with mostly shell-type SNRs (Torres et al., 2003). One such source was 3EG J0010+7309, with a relatively small 95% error circle of 28′ (Hartman et al., 1999), that was spatially coincident with the SNR CTA 1 (G119.5+10.2) and the X-ray point source RX J0007.0+7303, which was postulated to be a pulsar(Brazier et al., 1998). The association between 3EG J0010+7309 and RX J0007.0+7303 was found to be plausible, given the lack of flux variability seen in 3EG J0010+7309, its hard spectral index ($\Gamma = 1.58 \pm 0.18$ between 70 MeV and 2 GeV), and its similarity with other known pulsars detected by *EGRET* (Brazier et al., 1998).

CTA 1 is a composite SNR, discovered by Harris and Roberts (1960), with a shell-type structure in the radio band and a center-filled morphology at X-ray energies. The radio shell is incomplete towards the north-west (NW) of the remnant, possibly due to rapid expansion of the shock into a lower-density region (Pineault et al., 1993).

The distance to SNR CTA 1 as derived from the associated HI shell is $d = 1.4 \pm 0.3$ kpc (Pineault et al., 1997), the SNR age is estimated to be $\sim 1.3 \times 10^4$ yr (Slane et al., 2004), and the diameter of its radio shell is $\sim 1^\circ.8$ (Sieber et al., 1981).

Archival X-ray observations of SNR CTA 1 in the 5–10 keV band show non-thermal diffuse emission of low surface brightness in the center of the remnant, likely corresponding to a pulsar wind nebula driven by an active neutron star (Slane et al., 1997). The neutron star candidate RX J0007.0+7303 is a faint source located at the brightest part of the synchrotron emission (Seward et al., 1995). A *Chandra* image of RX J0007.0+7303 provides further evidence that this source is an energetic rotation-powered pulsar, resolving a central point source, a compact nebula, and a bent jet (Halpern et al., 2004). An initial observation with *XMM-Newton* in 2002 found the X-ray spectrum of the central source to be consistent with that of a neutron star, although no pulsations were detected (Slane et al., 2004). Based on these initial X-ray observations, the spin-down luminosity of the underlying pulsar was estimated to be in the range $10^{36} - 10^{37}$ ergs s^{-1}, supporting the identification of the *EGRET* source 3EG J0010+7309 as a pulsar (Halpern et al., 2004; Slane et al., 2004).

Eventually, a search for pulsed GeV emission from CTA 1 using the data from the *Fermi Gamma-Ray Space Telescope* revealed a highly significant 316 ms signal, confirming the origin of 3EG J0010+7309 (Abdo et al., 2008). The spin-down power was determined to be $\sim 4.5 \times 10^{35}$ erg s^{-1}, which is sufficient to power the pulsar wind nebula (Slane et al., 2004). Following the *Fermi* discovery of the gamma-ray pulsar, a deep 130 ks observation of RX J0007.0+7303 was carried out with *XMM-Newton* to characterize the timing behavior. The X-ray signal of PSR J0007+7303 was discovered at a statistical significance of 4.7σ in the 0.5-2 keV band, out of phase with the gamma-ray pulse (Caraveo et al., 2010). Similar to Geminga (Halpern and Holt, 1992) and 3EG J1836+5925 (Abdo et al., 2010; Halpern et al., 2007), PSR J0007+7303 is also radio quiet and underluminous in X-rays. GeV emission in the off-pulse phase interval

has also recently been detected by *Fermi* (Abdo et al., 2012).

Many galactic TeV sources appear to be associated with pulsars via their wind nebulae, comprised of relativistic wind particles confined by the pressure of the surrounding medium (Gaensler and Slane, 2006). The initially highly supersonic wind terminates in a shock which can be associated with axisymmetric, toroidal structures often seen in the X-ray images of PWNe (e.g., Kargaltsev and Pavlov, 2008).

PWNe now represent the most populous class of TeV emitters (Hinton and Hofmann, 2009). The non-thermal emission seen in PWNe from the radio up to gamma rays below a few GeV or less is generally interpreted as synchrotron radiation from the accelerated leptons. The emission observed at higher energies, up to several TeV, can be produced via inverse Compton (IC) scattering of these same high-energy electrons with background photons (e.g. the cosmic microwave background (CMB), infrared radiation from dust, starlight, and synchrotron photons) (Atoyan and Aharonian, 1996). Alternatively, hadronic mechanisms may also be responsible for the TeV emission, in which case the wind should be composed of relativistic hadrons that collide with the ambient medium and produce pions, with the TeV emission coming from π^0 decay. To date, however, there has been no solid evidence requiring a large contribution to the gamma-ray emission from such hadronic processes.

PWNe experience several stages of evolution (e.g., Gaensler and Slane, 2006). At an early stage the pulsar wind freely expands into the SN ejecta. For a slowly moving pulsar the PWN is approximately centered on the pulsar while for a supersonically moving pulsar the PWN will take a cometary shape. At later times, the PWN is compressed by the reverse SNR shock and may be displaced significantly from the pulsar if the reverse shock is asymmetric. Such crushed and displaced PWNe have been dubbed relic PWNe.

The X-ray and gamma-ray observations of CTA 1 suggest that the extended non-thermal emission around the gamma-ray pulsar is a synchrotron PWN. Motivated by

these observations, model calculations by Zhang et al. (2009) suggested that the TeV emission is largely produced by the PWN, and that the level of emission should be detectable at TeV energies by *VERITAS*. For IC scattering off the PWN electrons, Zhang et al. (2009) predicted a gamma-ray flux $F_\gamma(1 - 30 \text{ TeV}) \sim 1.1 \times 10^{-12}$ erg cm^{-2} s^{-1}. Previous TeV observations of CTA 1 by the earlier imaging atmospheric Cherenkov telescopes gave upper limits, as follows: 2.64×10^{-11} photons cm^{-2} s^{-1} ($E >$ 250 GeV) by CAT (Khelifi et al., 2001), 1.25×10^{-11} photons cm^{-2} s^{-1} ($E > 620$ GeV) by Whipple (Hall et al., 2001), and 1.09×10^{-12} photons cm^{-2} s^{-1} ($E > 1.3$ TeV) by HEGRA (Rowell and HEGRA Collaboration, 2003).

In this paper, we report the *VERITAS* detection of TeV emission from the central region of CTA 1.

4.3 VERITAS instrument & observations

The Very Energetic Radiation Imaging Telescope Array System (*VERITAS*) uses ground-based detection techniques pioneered by its predecessor, the Whipple 10m Telescope (Weekes et al., 1989), to explore the Universe in very high-energy (VHE) gamma rays from $\sim$ 100 GeV to $\sim$ 30 TeV. The *VERITAS* telescope array consists of four 12-m diameter Davies-Cotton telescopes and is located at the basecamp of the Fred Lawrence Whipple Observatory (FLWO) in southern Arizona (Holder et al., 2011). Flashes of Cherenkov light from gamma-ray and cosmic-ray showers are focused by a set of mirrors onto a camera located in the focal plane of each telescope. Each camera comprises 499 photomultiplier tube pixels and light concentrators arranged in a hexagonal pattern with a total field-of-view of $3^\circ.5$. Stereoscopic imaging of showers from multiple viewing angles allows the determination of the shower core location relative to the array using simple geometric reconstruction techniques which rely on the fact that the major axes of the shower images are projections of the shower axis. The combined instrument has an angular resolution of $< 0^\circ.1$ (68% containment) and

energy resolution of $15 - 20\%$ for energies > 200 GeV. It can detect a source with a flux of 1% of the steady Crab Nebula VHE flux at a 5 standard deviation significance level in less than 30 hours (Ong et al., 2009).

A three-level trigger system is used to help eliminate background noise. The first trigger occurs at the pixel level, requiring the signal to reach a 50 mV threshold (corresponding to 4–5 photoelectrons) set by a constant fraction discriminator (CFD). The second, telescope-level trigger requires at least three adjacent pixels passing the CFD trigger to form an image. A third, array-level trigger requires simultaneous Cherenkov images in at least two telescopes, within a 50 ns time window, which then causes a readout of the 500 MSample/s Flash-ADC data acquisition system for each pixel.

CTA 1 was observed over two epochs. The first set of observations spanned from September 2010 to January 2011, with a total livetime of 25 hours 39 min after data-quality selection based on weather conditions and hardware status. An additional 15 hours 36 min of quality-selected data were taken from September to December 2011. Observations were taken in "wobble" mode (Fomin et al., 1994), in which the telescope pointing is offset from the source position by some angular distance. This method allows for simultaneous collection of data and estimation of the background. Due to the extended nature of the remnant and expected extension of the PWN, an offset distance of $0°.7$ was used, larger than the typical VERITAS distance of $0°.5$. To decrease bias, the offset direction was varied between each 20 minute run while maintaining the same offset distance, alternating between the north, south, east and west directions (in the equatorial coordinate system). Observations were taken in a narrow range of zenith angles, $40 - 47°$, with an average of $42°.5$ for the full dataset. All of the data presented here were taken with all four telescopes in the array.

4.4 Analysis

The CTA 1 data were processed using standard *VERITAS* analysis techniques, as described in Acciari et al. (2008). The cosmic-ray background was suppressed efficiently by parametrizing the recorded shower images by their principal moments (Hillas, 1985), and the shower direction and impact parameter were reconstructed from these images, using stereoscopic methods (see, e.g., Aharonian et al., 1997; Krawczynski et al., 2006). Gamma-ray/hadronic shower separation is achieved through selection criteria (*cuts*). Based upon the predicted spectrum of Zhang et al. (2009), two sets of standard cuts were used. These cuts were optimized on simulations for sources of $\sim 5\%$ of the Crab Nebula flux and with moderate and hard spectral indices ($\sim$ -2.5 and -2.0, respectively). For these cuts, at least three of the telescopes in the array had to have images recorded in the camera, with at least 1200 digital counts ($\sim$ 240 photo-electrons) for the hard-cut analysis and 500 digital counts ($\sim$ 95 photo-electrons) for the moderate-cut analysis. Cuts were also applied to the mean scaled length (*MSL*), mean scaled width (*MSW*), and integrated charge in the signal (*size*). Finally a cut was applied on θ, the angular distance in the field of view from the reconstructed arrival direction of the event to the putative source location. A cut of $\theta < 0^\circ.09$ ($\theta < 0^\circ.23$) was used for a point-source (extended-source) search, with the size of the extended-source cut selected *a priori*. For the analysis presented here, the cuts for the moderate- and hard-spectra analysis are $MSW < 0.35$ and $MSL < 0.7$.

The background was estimated using the ring background model (e.g., see Berge et al., 2007), with a ring of mean radius $0^\circ.7$ and a background to source area ratio of 8.0. Regions in the field of view containing stars of B magnitude brighter than 6.0 were excluded from the background estimation in order to reduce systematic errors. The statistical significance of the excess was calculated using Equation 17 of Li and Ma (1983). The energy threshold for this analysis after applying the moderate (hard) cuts is $\sim$ 550 GeV (1 TeV) at a zenith angle of 45°, with a systematic error of about

20% on the energy estimation. Two independent analysis packages, as described by Cogan (2008) and Daniel (2008), were used to reproduce the results presented here on CTA 1.

4.5 Results

Figure 4.1 shows the TeV excess map of the region of the sky around CTA 1. The hard-spectrum, extended-source analysis produced an excess with a significance of 7.5 standard deviation (σ) pre-trials, in a search region of radius $0^\circ.4$ around the pulsar PSR J0007+7303, within the radio shell of the SNR CTA 1. Accounting for the two sets of applied cuts with two different integration radii, and determining the *a priori* trials factor by tiling the search region with $0^\circ.04$ bins (Aharonian et al., 2006b), we estimate the post-trials significance of detection to be 6.5σ. Overlaid on the TeV image are the high-resolution radio contours at 1420 MHz, obtained using the Dominion Radio Astrophysical Observatory (DRAO) Synthesis Telescope, and the Effelsberg 100-m telescope, showing bright radio arcs visible to the south and east, with an incomplete shell in the northwest, possibly due to the breakout of the SNR blast wave into a medium of lower density (Pineault et al., 1993, 1997).

For spectral analysis, the moderate-spectrum cuts were used in order to provide the lowest energy threshold for the analysis. The differential photon spectrum above 500 GeV is shown in Figure 4.2, with spectral data points listed in Table 4.1. The spectrum is generated with the reflected-region background model (Berge et al., 2007) with 41 hours 15 min of quality-selected data. The spectrum can be fit with a power-law of the form $dN/dE = N_0(E/3\ \mathrm{TeV})^{-\Gamma}$, with $\Gamma = 2.2 \pm 0.2_{\mathrm{stat}} \pm 0.3_{\mathrm{sys}}$ and $N_0 = (9.1 \pm 1.3_{\mathrm{stat}} \pm 1.7_{\mathrm{sys}}) \times 10^{-14}\ \mathrm{cm}^{-2}\ \mathrm{s}^{-1}\ \mathrm{TeV}^{-1}$. The integral energy flux above 1 TeV, $F_\gamma = 4.0{\times}10^{-12}$ erg cm^{-2} s^{-1}, corresponds to 0.2% of the pulsar spin-down luminosity at 1.4 kpc and $\sim 4\%$ of the steady TeV gamma-ray emission from the Crab Nebula.

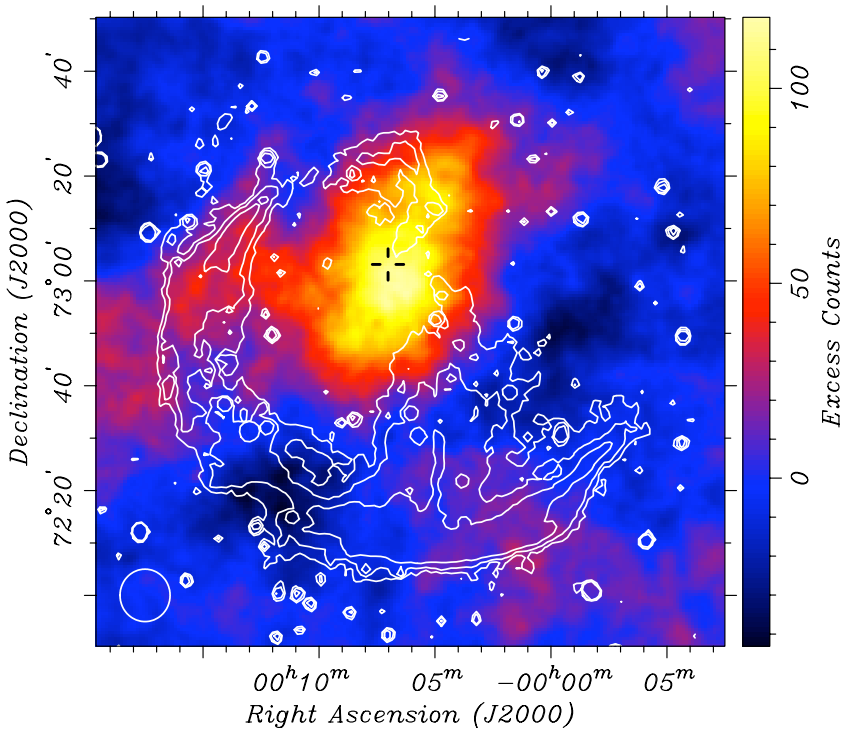

Figure 4.1: *VERITAS* excess map of the region around SNR CTA 1 using a hard-spectrum analysis. The color scale indicates excess gamma-ray events within an integration radius of 0°.23. The circle at the lower left corner shows the size of the point-spread function (68% containment). The radio contours at 1420 MHz (Pineault et al., 1997) are overlaid in white, showing the SNR shell. The cross marks the position of the pulsar (Abdo et al., 2008), located $5' \pm 2'$ from the centroid of TeV emission. North is up and east is to the left.

Energy Range [TeV]	Flux [cm^{-2} s^{-1} TeV^{-1}]	Significance [σ]
0.56 – 1.00	$(1.9 \pm 0.9) \times 10^{-12}$	2.3
1.00 – 1.78	$(7.3 \pm 1.7) \times 10^{-13}$	4.5
1.78 – 3.16	$(1.2 \pm 0.4) \times 10^{-13}$	3.3
3.16 – 5.62	$(3.4 \pm 1.2) \times 10^{-14}$	3.1
5.62 – 10.00	$(1.2 \pm 0.5) \times 10^{-14}$	2.5
10.00 – 17.78	$(7.1 \pm 2.5) \times 10^{-15}$	2.8

Table 4.1: Differential flux measurements of CTA 1 with *VERITAS*. The errors are statistical only.

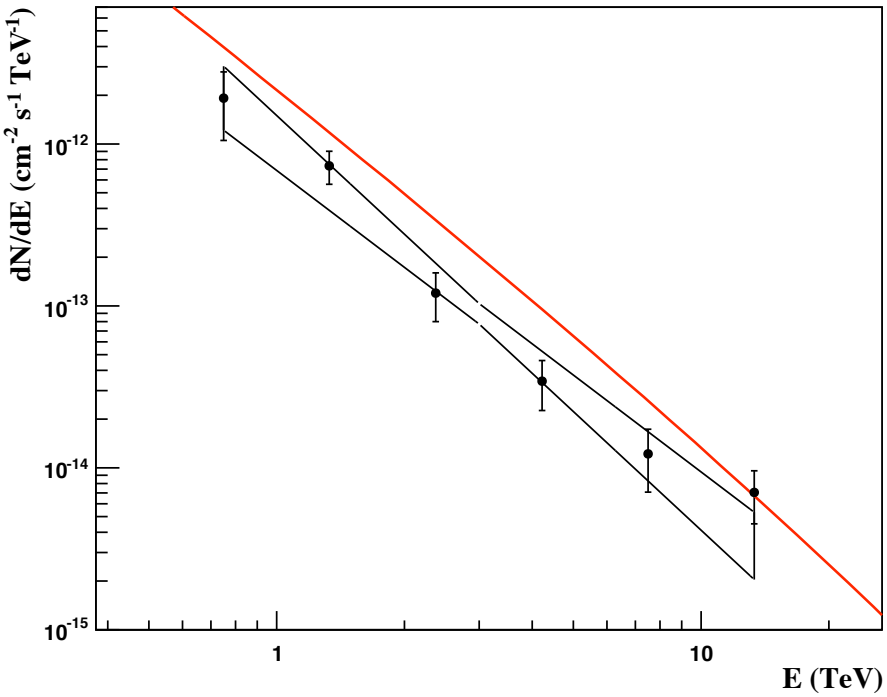

Figure 4.2: *VERITAS* differential gamma-ray spectrum of CTA 1. The black butterfly shows the uncertainties of the best-fit power-law model. The red line marks the flux predicted by Zhang et al. (2009, Figure 4). The errors are statistical only.

4.5.1 Morphology

Figure 4.1 shows that the extent of the TeV gamma-ray emission region in CTA 1 exceeds the point-spread function (PSF; 68% containment radius of the events coming from a point source) of *VERITAS*. In order to estimate the extent of the source, an asymmetric two-dimensional Gaussian is fit to the acceptance-corrected uncorrelated map of excess events binned in $0^\circ.05$ bins. Although the shape and extent of the emission is likely more complex than a simple asymmetric Gaussian, as a first approximation, it still provides a statistically reasonable estimate of the source extent. Due to the finite resolution of the detector, the emission we see is a convolution of the real source and the PSF describing the system. Accounting for the PSF of the instrument, the resulting 1σ angular extent is $0^\circ.30 \pm 0^\circ.03$ along the semi-major axis and $0^\circ.24 \pm 0^\circ.03$ along the semi-minor axis, with an orientation angle of $17^\circ.4 \pm 15^\circ.8$ west of north. We note that this is a sensitivity-limited measurement.

The fitted centroid location is $00^h\ 06^m\ 26^s,\ +72^\circ\ 59'\ 01.0''$ (J2000), which is 5 arcmin from PSR J0007+7303. Therefore, the *VERITAS* source name is VER J0006+729. The statistical uncertainty in the centroid position is $0^\circ.09$ in RA and $0^\circ.04$ in declination. The systematic uncertainty in the position due to the telescope pointing error is 50".

4.5.2 Archival X-ray analysis

Figure 4.3 shows the exposure-corrected, smoothed *ROSAT* PSPC X-ray image of the region around CTA 1. The 0.5–2 keV *ROSAT* image reveals a center-filled morphology, with a faint compact source located at the peak of the brightness distribution. The cross in the image marks the location of the X-ray point source RX J0007.0+7303 and the *Fermi* pulsar J0007+7303. The pulsar is located close to the center of the extended TeV source with $\sim 5'$ offset from the peak of the TeV surface brightness. Figure 4.4 shows the non-thermal X-ray image from *ASCA* in the 4–10 keV band

(Roberts et al., 2001), along with the TeV contours. The non-thermal emission is seen to match well with the TeV emission morphology.

Figure 4.5 is the smoothed *XMM-Newton* image of the vicinity of PSR J0007+7303 showing the X-ray PWN. The inset shows the smoothed *Chandra* image revealing a compact nebula and bent jet attached to the point source, along with diffuse emission at larger scales. The *Chandra* jet is particularly apparent in the analysis presented by Halpern et al. (2004), where it is estimated that the *Chandra* point source accounts for $\sim 30\%$ of the flux of RX J0007.0+7303, with the compact nebula plus jet comprising the remaining $\sim 70\%$. The luminosity of the fainter large-scale emission (within $r < 4'$ from the pulsar) is about a factor of 5–10 larger than that of the compact PWN and pulsar. The X-ray spectrum of the point source can be described by an absorbed power-law plus blackbody model, with a photon index of $\Gamma = 1.6 \pm 0.6$. The compact PWN spectrum is harder, with a photon index $\Gamma \simeq 1 - 1.3$ (Halpern et al., 2004). The spectrum of the large-scale diffuse emission was fitted by Caraveo et al. (2010) with a power-law modified by the interstellar absorption. The fit gave $\Gamma = 1.8 \pm 0.1$. However, the fit quality was fairly poor suggesting a more complex spectrum (e.g., a possible additional thermal component; see below).

4.6 Discussion

We have discovered spatially extended TeV emission from the region of CTA 1. Here we discuss the results in the context of the available multiwavelength data.

4.6.1 The nature of the TeV source: A PWN scenario

The good positional match between the extended *VERITAS* source and CTA 1 makes their physical association virtually indisputable. However, the extent of VER J0006+729 is much smaller than that of the SNR and, hence, the TeV source does not resem-

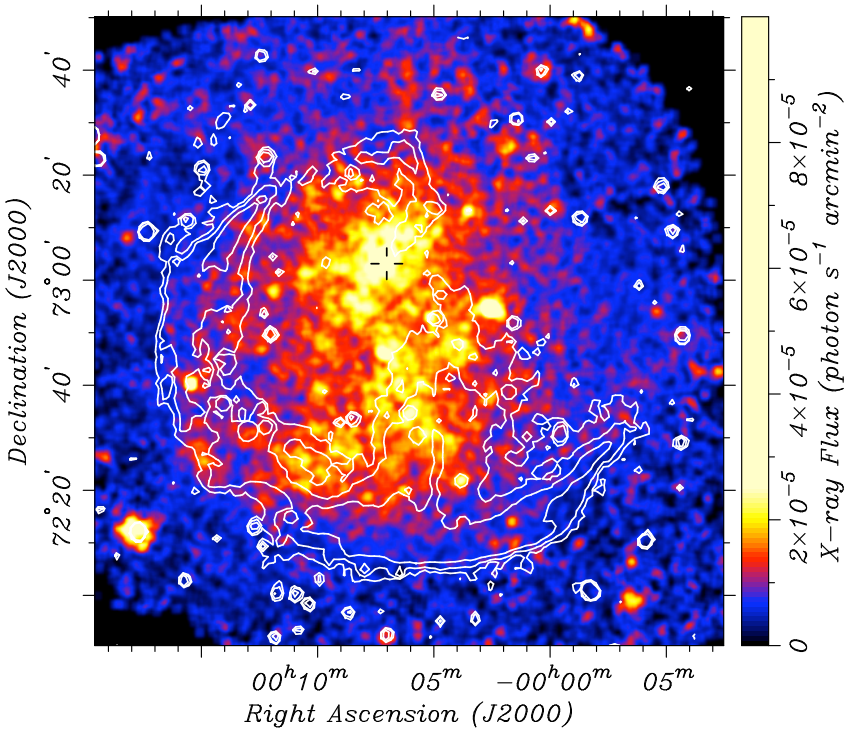

Figure 4.3: *ROSAT* X-ray image (0.5–2.0 keV) of the SNR CTA 1 shown in equatorial coordinates. The cross marks the location of the X-ray point source RX J0007.0+7303 and the *Fermi* PSR J0007+7303. The SNR shell is shown by the 1420 MHz radio contours (Pineault et al., 1997), overlaid in white.

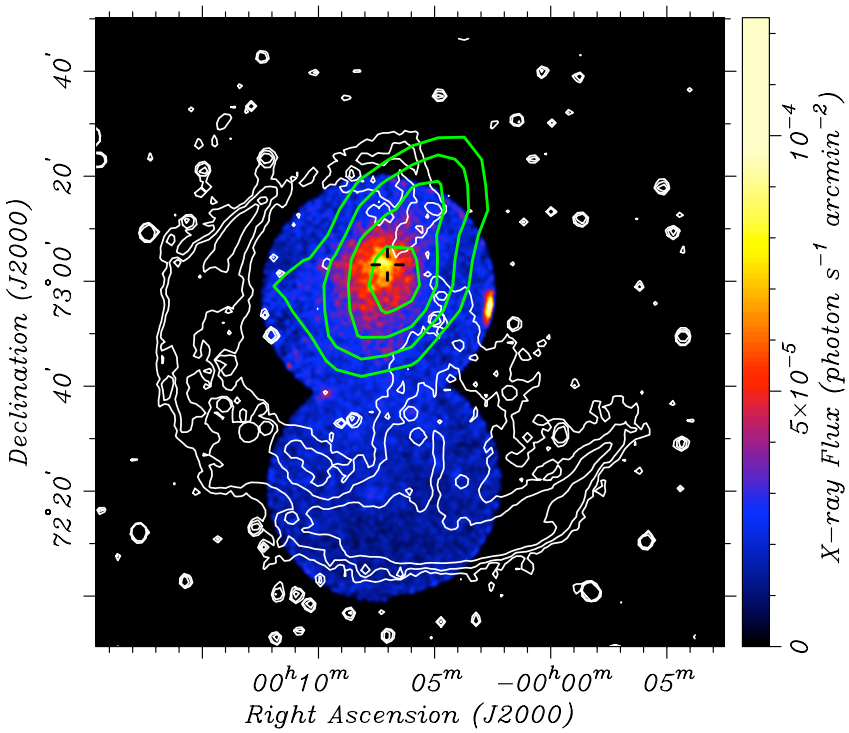

Figure 4.4: *ASCA* GIS image (4–10 keV) of the SNR CTA 1, using the same field of view as Figures 4.1 and 4.3. The position of PSR J0007+7303 is marked by the cross. The 1420 MHz radio contours are shown in white. The *VERITAS* significance contours at 3, 4, 5, and 6σ are shown in green.

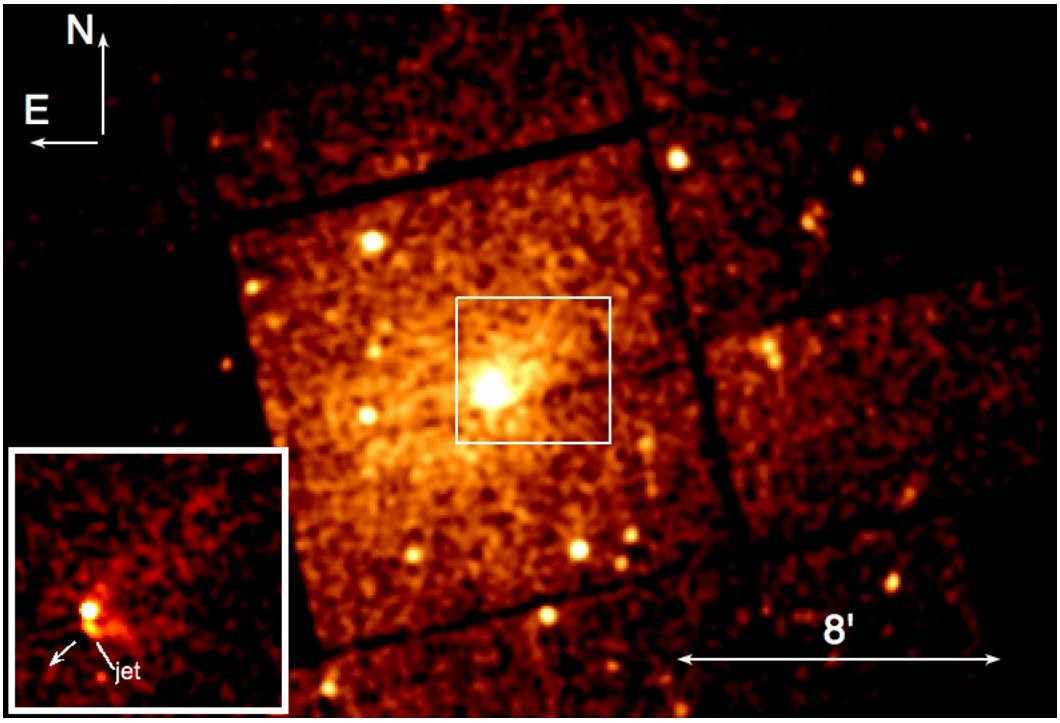

Figure 4.5: *XMM-Newton* 93 ks EPIC/MOS1+2 image (0.5–10 keV; pixel size 4″; smoothed with the $r = 12''$ Gaussian kernel) of PSR J0007+7303 and its vicinity showing the X-ray PWN. The inset is the higher resolution *Chandra* ACIS image (0.5–8 keV; pixel size 2″, smoothed with the $r = 4''$ Gaussian kernel). The arrow in the inset image shows the likely direction of the pulsar proper motion (based on the shape of the compact PWN).

ble several SNRs whose shells have been resolved in TeV gamma rays (Komin and for the H. E. S. S. collaboration, 2011). There still remains a possibility that only part of the CTA 1 shell is interacting with a dense molecular cloud which could cause a local enhancement in the TeV brightness of the emission (Komin and for the H. E. S. S. collaboration, 2011). However, we do not find any evidence for such a cloud at any other wavelength, including 60 μm IR or HI (see Pineault et al., 1993), and the high Galactic latitude of the SNR places it nearly 250 pc above the Galactic plane, much higher than the scale height of molecular clouds. The TeV source is also unlikely to be related to a gamma-ray binary or a background blazar given that the TeV emission is extended and non-variable.

Therefore, the most plausible remaining scenario is that VER J0006+729 is powered by the young PSR J0007+7303, which is located within the extent of the TeV source. The pulsar is surrounded by an X-ray PWN which consists of a bent jet, a compact core, and a large-scale diffuse component, as seen in the *Chandra* and *XMM-Newton* images (see Figure 4.5). The bending of the jet (see the inset in Figure 4.5, and also Halpern et al. (2004)) could be caused by the ram pressure of the oncoming medium due to the NW–SE pulsar motion or by the interaction with a reverse shock propagating NW within the SNR extent. Alternatively, a kink instability might be responsible for the bending of the jet. Indeed, the Vela pulsar jet shows some kink-like shape changes. However, these wiggles tend to occur on smaller spatial scales, while globally the Vela jet is always (during the last 10 years) seen to bend toward one side, likely due to the pressure of the oncoming ambient material (Pavlov et al., 2003). Similarly, in the *XMM-Newton* and *Chandra* images of CTA 1, obtained at different epochs, the jet is seen to consistently bend in the same direction.

If the change in the jet morphology is caused by ram pressure, then we can estimate the pressure from the jet's curvature, following Pavlov et al. (2003). Assuming that the jet pressure is dominated by the contribution from a magnetic

field $B_{-4} = B/(10^{-4}$ G), for a jet curvature radius $R_{\rm curv} \simeq 10''$ and a jet diameter $d_{\rm jet} \sim 1''$ the pressure estimate is $P_{\rm ram} \sim 1 \times 10^{-11} B_{-4}^2$ erg cm^{-3}. Despite the fairly high magnetic field assumed, the estimated pressure is rather low compared to the ambient pressure inferred for other young pulsars with X-ray PWNe resolved by *Chandra* (Kargaltsev and Pavlov, 2008). Assuming that the ram pressure is caused by the pulsar motion through a medium of density $n_{-1} = n/(10^{-1}$ cm$^{-3})$, one obtains a very modest pulsar speed $v \simeq 90\ n_{-1}^{-1/2} B_{-4}$ km s^{-1} which corresponds to the proper motion of just $\sim 0.013\ n_{-1}^{-1/2} B_{-4} d_{1.4}^{-1}$ arcs yr^{-1}, assuming a distance of $d_{1.4} = d/(1.4$ pc). This means that over its lifetime τ the pulsar should have moved by only $\sim 3\ n_{-1}^{-1/2} (\tau/1.3 \times 10^4$ yrs$) B_{-4} d_{1.4}^{-1}$ arcminutes. This distance is much less than the size of the SNR and the extent of the TeV source, and it is even less than the extent of large-scale X-ray PWN seen in the *XMM-Newton* and *ASCA* images. We also note that despite being dependent on several parameters, the above estimate of the distance traveled by the pulsar likely represents an upper limit. Thus the estimated velocity from the jet-bending is inconsistent with the otherwise plausible hypothesis that the NW extension of the TeV source (see Figure 4.1) might be due to aged relativistic electrons left behind by the fast moving pulsar.

It is also possible that the relic PWN that has been pushed to one side (i.e. NW of the pulsar) by the reverse shock that must have arrived from the SE direction. Indeed, such a scenario is supported by the overall asymmetry of the SNR shell which appears to expand into much lower density medium in its NW part and hence the reverse shock is not expected to arrive from the NW direction. A recent interaction with the reverse shock could possibly also explain the bending of the jet while emission ahead of the pulsar could be explained by the turbulent mixing between the pulsar wind and SN ejecta behind the reverse shock (similar to G327.1-1.1; Temim et al. 2009). The latter may contribute some thermal emission and explain the poor quality of the power-law fit to the extended X-ray emission (Caraveo et al., 2010). A deeper *XMM-Newton*

observation can test this hypothesis by providing a high-S/N spectrum of the faint large-scale X-ray emission which should then contain a thermal emission component coming from the ejecta (c.f. e.g., Vela X spectrum; LaMassa et al. 2008).

Pulsar wind particles may be transported either by diffusion or by advection. One could in principle compare the two terms, if the bulk flow speed (as a function of distance from the pulsar) and the magnetic field structure were known. The MHD models for isotropic pulsar winds (e.g., Kennel and Coroniti, 1984) are unlikely to be valid on large scales and when mixing due to interaction with the reverse shock is present. However, we can make some estimates of the average magnetic field by assuming which process is dominant in transporting the particles.

Assuming that X-ray- and TeV-emitting particles move away from the pulsar with similar velocities (i.e. that the X-ray- and TeV-emitting regions are co-spatial and that the effects of energy-dependent diffusion are negligible), and that the synchrotron cooling-time is the dominant time-scale, one can crudely estimate the magnetic field strength(see, e.g., Aharonian et al., 2005). For X-ray and TeV gamma-ray emission regions of sizes $R_{\rm X}$ and R_γ, respectively, with $\overline{E_{\rm X}}$ and $\overline{E_\gamma}$ being the corresponding mean energies of the photons in keV and TeV units, the magnetic field is $B_{\rm pwn} \sim 160(R_{\rm X}/R_\gamma)^2(\overline{E_{\rm X}}/\overline{E_\gamma})$ μG. For the observed $R_{\rm X}/R_\gamma \approx 0.5$, $\overline{E_{\rm X}} = 5$ keV, and $\overline{E_\gamma} = 5$ TeV, the corresponding average magnetic field is ~ 40 μG. This is much higher than what is suggested by modeling (see below) and also much higher than what is seen in other such evolved systems.

Note that the ratio $R_{\rm X}/R_\gamma \approx 0.5$ is likely an underestimate and the *ASCA* data suggest that it can be a factor of 2–3 larger (see Fig. 4.4). Indeed, in the *ASCA* images some diffuse emission appears to be seen up to $40'$ away from the pulsar (Slane et al., 2004). The true extent and the non-thermal nature of the faint X-ray emission can only be measured in deep observations with *XMM-Newton*. Similarly, the TeV size we quote is a lower limit since more the extended portions away from the pulsar are likely

to be the fainter than our detection threshold. The estimate of the average magnetic field should thus be taken as a crude order-of-magnitude estimate.

Another estimate of the magnetic field can be made by assuming that diffusion is the dominant transport mechanism throughout the nebula. In the simplest case of cross field diffusion (the Bohm limit), the diffusion constant is given by $D = \gamma mc^3/3eB$, where γ is the electron Lorentz factor. Using the relation $E_\gamma \sim \gamma^2 \epsilon$, where E_γ is the mean up-scattered IC photon energy and ϵ is the seed photon energy, the diffusion constant for electrons scattering on the CMB in a magnetic field $B_{-5} = B_{\rm pwn}/(10^{-5}$ G) can then be expressed as $D = 8.5 \times 10^{25} E_\gamma^{1/2} B_{-5}^{-1}$ cm^2 s^{-1}. Assuming that particles travel during their characteristic cooling time of $\tau_\gamma \approx 100(1 + 14.4 B_{-5}^2)^{-1} E_\gamma^{-1/2}$ kyrs (see de Jager and Djannati-Ataï, 2009), the diffusion length is $\sim (6D\tau_\gamma)^{1/2} \sim 13 B_{-5}^{-1/2}(1 + 14.4 B_{-5}^2)^{-1/2}$ pc which translates into $\sim 20' d_{1.4}^{-1}$ for $B_{\rm pwn} = 5$ μG. (Note that, for a given distance to CTA 1, this estimate depends only on the magnetic field strength.) This size roughly corresponds to the observed extent of the TeV source. Although small, such low magnetic field (~ 5 μG) was inferred through the multiwavelength spectral modeling for the Vela X plerion (de Jager et al., 2008). The low $B_{\rm pwn}$ resulting from the Bohm diffusion estimates has been previously noticed for several other relic PWNe (e.g. de Jager and Djannati-Ataï (2009), as well as by Uchiyama et al. (2009) and Anada et al. (2010) based on their analysis of the synchrotron spectra measured by *Suzaku* across the extent of TeV sources HESS J1825–137 and HESS J1809–193.)

Furthermore, we can use a dynamical model for the evolution of a PWN inside a non-radiative SNR (Gelfand et al., 2009) to estimate the physical properties of the PWN. The results are illustrated in Figure 4.6. We find that to correctly reproduce the radius of the SNR (lower panel, shown in blue) while simultaneously matching the estimated PWN radius (shown in red), the current spin-down power, and the total TeV flux, we require an ambient density $n_0 \approx 0.07$ cm^{-3}. This is somewhat larger

than that estimated from *ASCA* measurements of the thermal X-ray emission (Slane et al., 1997, 2004), although those measurements were based on observations of a small fraction of the SNR shell.

Also shown in Figure 4.6 (upper panel) is the time evolution of the PWN magnetic field for this model. At the current age of $\sim$ 10 kyr implied by the SNR radius, the PWN magnetic field strength is $\sim$ 6 μG. The recent decrease in the PWN radius, and increase in the magnetic field, result from the beginning of the SNR reverse shock interaction with the nebula, as suggested by other arguments presented above. Figure 4.7 shows the archival broadband data for CTA 1 along with the emission predicted for the model used in Figure 4.6 assuming a broken power-law injection of particles from the pulsar, for which a braking index of 3 is assumed. The model parameters are summarized in Table 4.2.

Radio observations of CTA 1 do not provide conclusive evidence for emission from the PWN (Pineault et al., 1997). We note that, in their modeling, Zhang et al. (2009) assumed that the entire emission from the SNR was associated with the PWN. In fact, the PWN is much fainter. Here we have used the 1.4 GHz image from Pineault et al. (1997) to estimate the flux within a 20 arcminute radius around the pulsar, and have used this flux as an upper limit for the PWN emission. In Figure 4.7, we have extrapolated this upper limit to lower frequencies assuming a spectral index $\alpha = 0.3$ (where $S_\nu \propto \nu^{-\alpha}$, is the flux at the frequency ν) and to higher frequencies assuming $\alpha = 0$. These index values represent the typical range observed in radio PWN, and the associated flux values correspond to conservative upper limits. An additional difference in the models is that we have calculated the evolving magnetic field strength based on the fraction of spin-down energy injected as magnetic flux whereas Zhang et al. (2009) assume a time-dependent field value which is independent of any other system parameters. Our results suggest a break energy of $\sim$ 50 GeV with $\sim$ 80% of the spin-down power appearing in the form of particle flux. Like most such

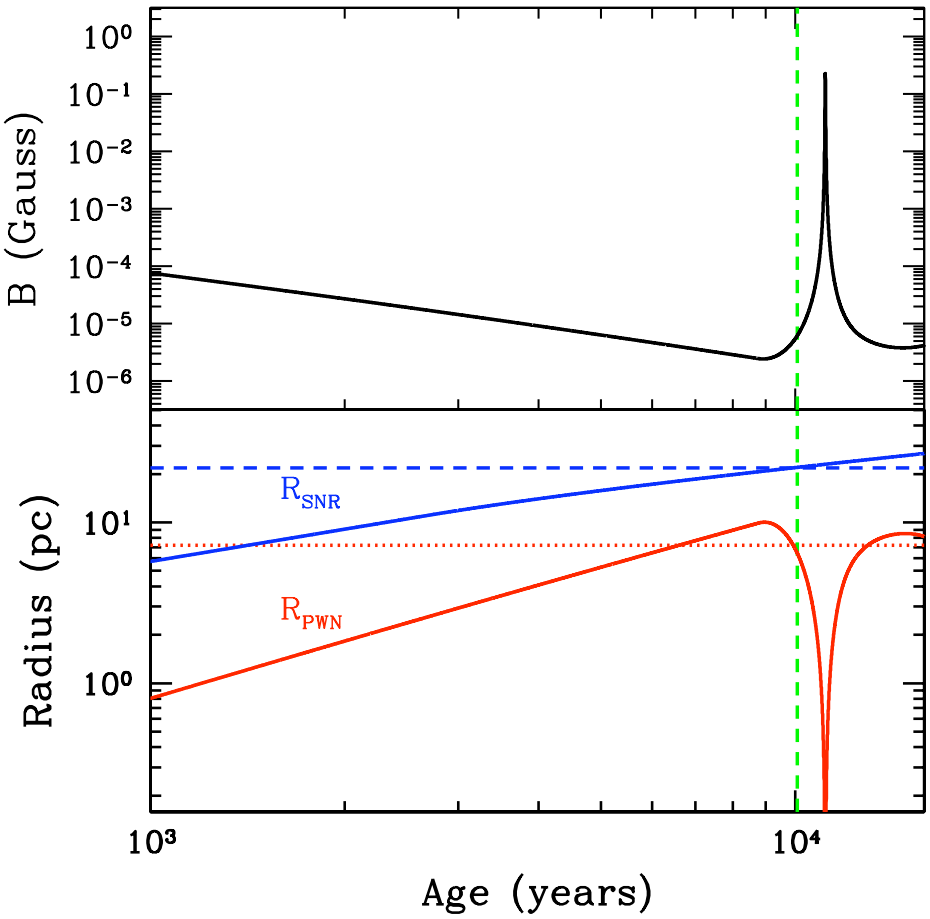

Figure 4.6: Upper: Time evolution of the PWN magnetic field, using the model of Gelfand et al. (2009), with parameters given in Table 4.2. Lower: Time evolution of the modeled SNR (blue) and PWN (red) radii. Horizontal dashed lines indicate the current values for CTA 1. The vertical green line indicates the age at which the measured SNR radius is reached. (See text for model description.)

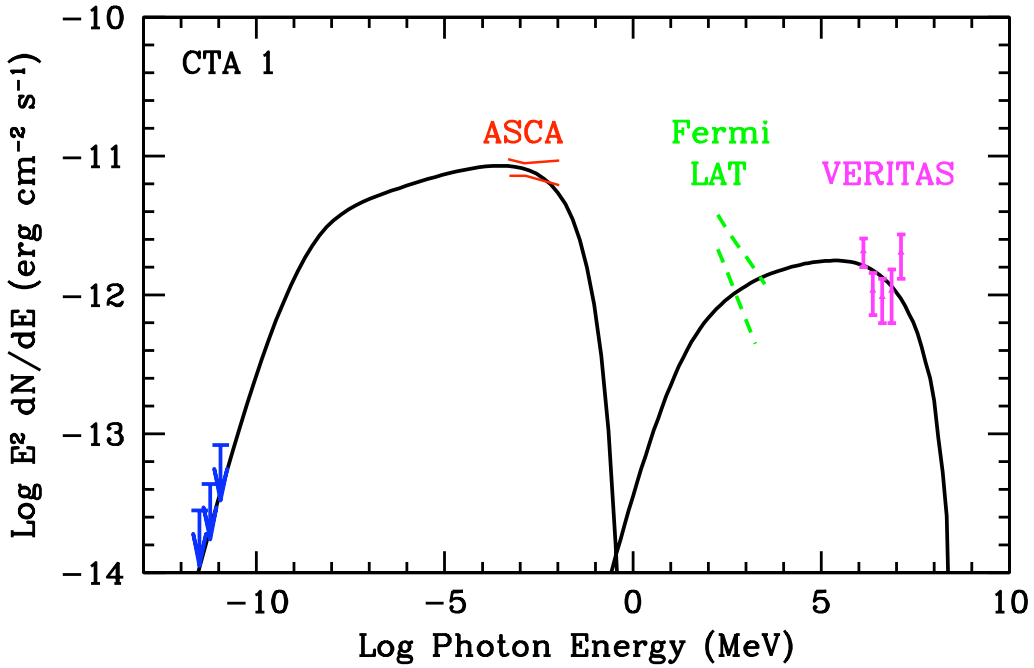

Figure 4.7: Broadband emission from CTA 1, along with a model for synchrotron and inverse Compton emission from the PWN.

systems, CTA 1 is thus a particle-dominated PWN.

The dashed green curves in Figure 4.7 represent the best fit for the unpulsed *Fermi*-LAT spectrum published in Abdo et al. (2012). In the model calculation shown, the TeV emission is produced by inverse Compton scattering of photons from the CMB, integrated starlight, and infrared emission from local dust, following the approximate prescription given by Strong et al. (2000). The model produces reasonable agreement with the radio, X-ray, and TeV data with a solution that gives approximately the correct pulsar spin-down power and characteristic age at the current epoch. However, the model is a poor fit to the reported *Fermi*-LAT spectrum. We have considered additional photon fields to produce enhanced inverse Compton emission at GeV energies, but have been unable to reproduce the published spectral index. We note that the reported unpulsed GeV emission is quite faint and it is in the presence of bright pulsed emission from PSR J0007+7303. It will be of considerable interest to carry out further investigations of this unpulsed emission as more *Fermi*-LAT data

Parameter	Value
Input:	
Explosion Energy, E_{SN}	10^{51} erg (fixed)
Ejecta Mass, M_{ej}	6.1 $M_\odot$
Ambient density, n_0	0.068 cm^{-3}
Initial spin-down, $\dot{E}_0$	7.5×10^{36} erg s^{-1}
Spin-down timescale, τ_0	3.2×10^3 yr
Braking index, n	3 (fixed)
η_B	0.2
α_1	0.5
α_2	2.8
Break energy, E_b	50 GeV
Output:	
Age	1.0×10^4 yr
B_{PWN}	6.3 μG
$\dot{E}$	4.4×10^{35} erg s^{-1}
τ_c	1.3×10^4 yr
P_0	155 ms

Table 4.2: Model parameters for broadband emission from CTA 1. See Gelfand et al. (2009) for parameter definitions.

are accumulated.

4.6.2 Comparison with other relic PWNe

Figures 4.8, 4.9, and 4.10 show the comparisons of the properties of CTA 1 with other PWNe and PWNe candidates detected at TeV energies. At the distance of 1.4 kpc, the > 1 TeV luminosity of the PWN in CTA 1 is 9.4×10^{32} erg s^{-1}. Figure 4.8 shows the relative luminosities of PWNe in the TeV and X-ray bands, as functions of spin-down power and characteristic age (Kargaltsev and Pavlov, 2010). CTA 1 fits with the picture that TeV PWNe are generally found around pulsars with ages $\lesssim$100 kyrs and $\dot{E} \gtrsim 10^{35}$ erg s^{-1}, although the TeV luminosities do not depend on the pulsar age nearly as much as the X-ray PWNe luminosities do. Figure 4.9 shows the distance-independent ratio of the TeV to X-ray luminosity as a function of characteristic age for a set of PWNe or PWN candidates, with the CTA 1 marked by the red triangle.

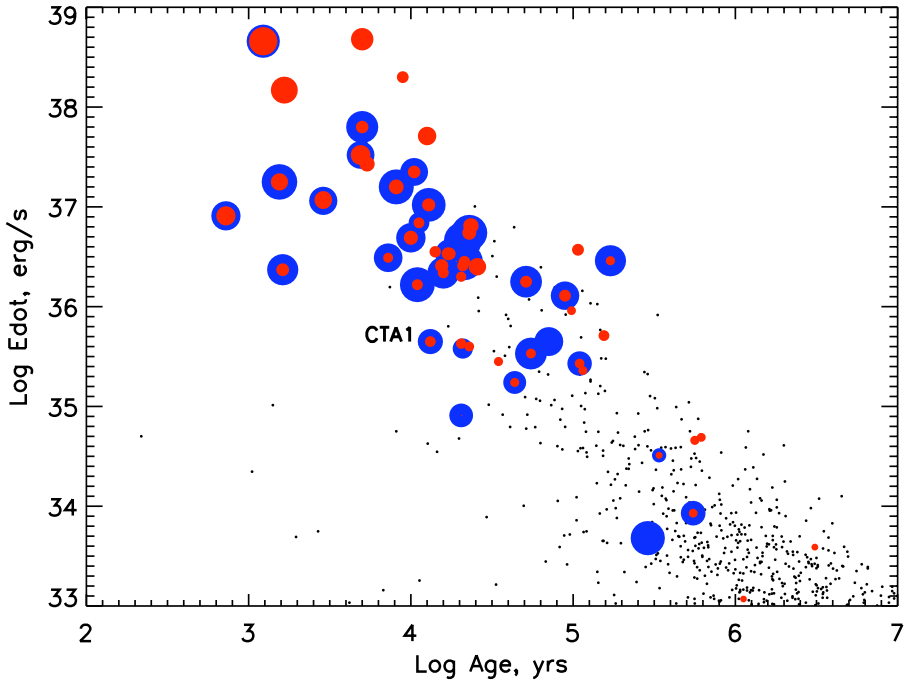

Figure 4.8: Pulsar spin-down luminosity vs age, from Kargaltsev and Pavlov (2010), with CTA 1 point indicated. Filled circles: X-ray (red) and TeV (blue) luminosities of PWNe or PWN candidates. Larger circle sizes correspond to higher luminosities in the corresponding waveband. Small black dots denote ATNF catalog pulsars (Manchester et al., 2005).

Figure 4.10 shows the diameter of the TeV nebula as a function of characteristic age for various PWNe and PWN candidates, with the CTA 1 indicated in red. A comparison of CTA 1 with the TeV/X-ray PWN population supports the PWN origin of the TeV emission.

4.7 Summary and Conclusions

VERITAS has detected TeV gamma-ray emission coincident with SNR CTA 1. The emission is extended, with a centroid near the *Fermi* gamma-ray pulsar PSR J0007+7303 and its X-ray pulsar wind nebula (PWN). The photon spectrum is well described by a power-law with differential spectral index of $\Gamma = 2.2 \pm 0.2_{\rm stat} \pm 0.3_{\rm sys}$ and an inte-

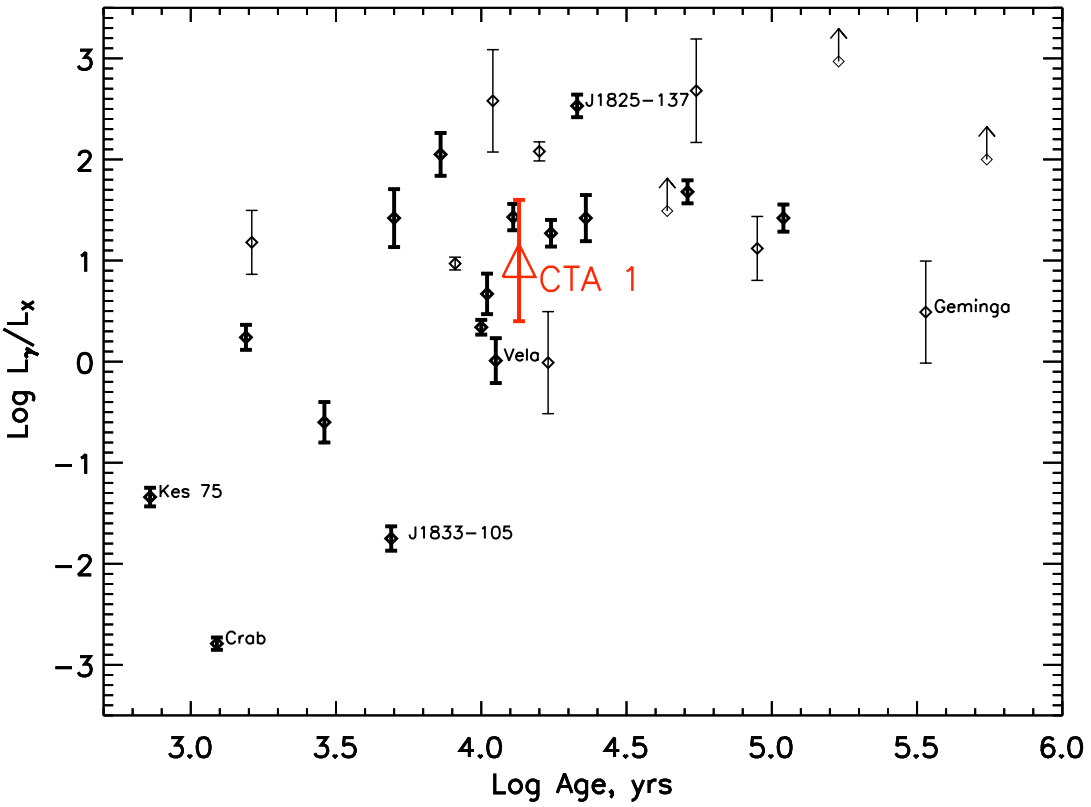

Figure 4.9: Plot of the ratio of TeV to X-ray luminosity vs pulsar spin-down age, from Kargaltsev and Pavlov (2010), with CTA 1 shown by the red triangle. Thick and thin error bars correspond to firm and tentative (or questionable) PWN associations (see Kargaltsev and Pavlov for further details).

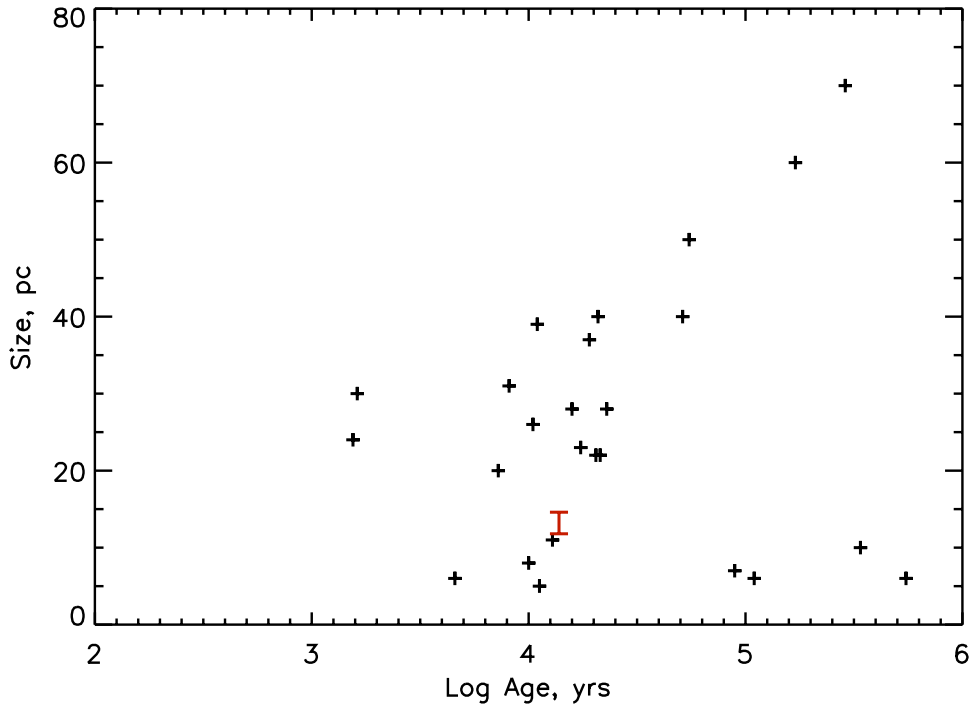

Figure 4.10: Plot of the TeV PWN diameter vs pulsar spin-down age, with CTA 1 shown in red. The values are taken from Kargaltsev and Pavlov (2010), except for the angular sizes of HESS J1825-137, HESS J1616-508, and HESS J1804-216, which are taken from Aharonian et al. (2006b). Note that the sizes are approximate with large uncertainties.

gral flux above 1 TeV corresponding to $\sim 4\%$ of the steady TeV gamma-ray emission from the Crab Nebula. It is unlikely that the TeV emission is due to interaction of the CTA 1 shell with a dense molecular cloud, given that lack of evidence for such a cloud at other wavelengths (60 μm IR or HI maps). We have analyzed archival X-ray data from *ROSAT* (0.5–2 keV) and *ASCA* (4–10 keV) of the large scale nebula and *XMM-Newton* (0.5–10 keV) and *Chandra* (0.5–8 keV) of the region close to the pulsar and find that the large scale emission seems to match the TeV morphology. The positional coincidence with the pulsar, small extent of the TeV emission, and X-ray/TeV luminosities strongly argue for a PWN origin. We have estimated the magnetic field strength assuming particle transport by either diffusion or by advection. A more detailed dynamical model of the SNR-PWN system suggests a 6 μG field along with a recent interaction between the PWN and the SNR reverse shock.

This research is supported by grants from the U.S. Department of Energy Office of Science, the U.S. National Science Foundation and the Smithsonian Institution, by NSERC in Canada, by Science Foundation Ireland (SFI 10/RFP/AST2748) and by STFC in the U.K. We acknowledge the excellent work of the technical support staff at the Fred Lawrence Whipple Observatory and at the collaborating institutions in the construction and operation of the instrument.

Chapter 5

Energy-dependent morphology of CTA 1

As the various transport and loss mechanisms within PWNe exhibit different dependencies on particle energy and magnetic field strength, it may be expected that the particle populations and their resultant emission profiles would exhibit energy-dependent morphologies. Although CTA 1 is a relatively weak source, a first attempt at measuring such a dependence was made. This chapter presents the results of an initial investigation of the angular distribution and energy spectrum of CTA 1 data collected by *VERITAS*. This analysis requires that one account for the dependence of the instrumental point spread function upon both gamma-ray energy and the zenith angle of observation, so we begin with a discussion of the *VERITAS* PSF from simulation studies and point-source data.

5.1 Selecting the energy ranges

Morphological studies are performed on a map of excess gamma-ray like events across the observed region. Given the faintness of the emission, the data is separated into only two discrete energy bands. The separation energy E_{sep} may then be chosen *a priori* so

that an approximately equal number of excess events fall within each band. Using the spectral analysis of the entire data set and histograming the events into logarithmic energy bins of width $\Delta \log E = 0.05$ results in an energy $E_{sep} = 3$ TeV.

5.2 The point-spread function

As with any imaging system, *VERITAS* can not reconstruct a point source perfectly, leading to a finite resolution in the reconstructed image of any extended source of gamma-ray emission. This point spread function (PSF) can be estimated with simulations of the detector response and compared with observations of a point source (i.e. a source of sufficiently small angular extent). Observations of the Crab Nebula have shown it to be compatible with a point-source for modern TeV instruments (e.g., Aharonian et al., 2006a; Albert et al., 2008). Given its relatively steady, strong TeV emission, the Crab has long been considered a standard candle for the field. Thus I analyzed data from the Crab Nebula taken under similar conditions to our CTA 1 data.

As the zenith angle of observations changes, several geometric effects come into play that can effect the gamma-ray PSF. First, the larger distance to the shower maximum with increasing zenith angle makes images appear smaller, as well as results in a reduction in the parallactic displacement of shower images from the center of the field of view (the Distance parameter). Second, as the the array is viewed from lower elevations, the projected positions of the individual telescopes approaches a line, while the larger footprint of the shower makes it more likely for the shower images to fall well outside of the array. As the shower directions are reconstructed (see Section 2.3.3), these effects decrease the angle between the major axes for each pair of images, leading to greater uncertainty in the position of origin.

The PSF may also be dependent on the selection cuts used in the analysis. Events with a larger Size value are less affected by noise, which should lead to better source

Parameter	Moderate	Hard
No. of $\text{pixels}_{\text{min}}$	5	5
$\text{Distance}_{\text{max}}$	1.43	1.43
Size_{min}	400 dc	1000 dc
$\text{MSW}_{\text{min/max}}$	0.05/1.15	0.05/1.1
$\text{MSL}_{\text{min/max}}$	0.05/1.3	0.05/1.2
Emission $\text{height}_{\text{min}}$	7 km	–
No. of $\text{telescopes}_{\text{min}}$	3	3

Table 5.1: Quality and gamma-hadron separation cuts applied to both the CTA 1 data and Crab Nebula data sets. Cuts are applied as the maximum and minimum allowed values of the specified shower parameters, as indicated by subscripts.

localization. However, larger images are more prone to 'clipping' by the edge of the camera, which can affect the event reconstruction.

Measurement of the PSF are based on 9.3 hours of 4-telescope, quality-selected data on the Crab Nebula covering a range of moderate zenith angles (MZA), 35–50°. This range is similar to that of the observations of CTA 1. In addition, 8 hours of data were also selected at small zenith angles (SZA) of $< 20°$ for comparison. The same cuts were applied to the Crab Nebula data as had been applied to the CTA 1 data, as described in Table 5.1.

A map of counts above background was produced for each data set, using the ring-background model. This excess map, corrected for acceptance, was fit with a sum of two, symmetric, two-dimensional

$$G(\vec{r}) = A\left[e^{-(\vec{r}-\vec{r}_0)^2/(2\sigma_1^2)} + A_{rel}\; e^{-(\vec{r}-\vec{r}_0)^2/(2\sigma_2^2)}\right], \tag{5.1}$$

where r_0 is the fitted centroid position, A is an overall normalization factor, A_{rel} is a relative scaling factor, and σ_1 and σ_2 parameterize the widths of the Gaussians. For an single 2D Gaussian, σ constitutes the 39% containment radius, r_{39}. The PSF is also commonly cited in terms of the 68% containment radius, r_{68}, which, for a single 2D Gaussian, equals $\sim 1.51\ r_{39}$. For the sum of Gaussians, these containment radii

Zenith angles	Cuts	Energy range [TeV]	r_{39} [10^{-2} degrees]	r_{68} [10^{-2} degrees]
SZA	mod.	all	6.2	10.3
		< 3	6.2	10.3
		> 3	5.0	9.4
	hard	all	4.9	8.0
		< 3	4.9	8.0
		> 3	4.8	8.1
MZA	mod.	all	7.6	13.1
		< 3	7.8	13.2
		> 3	5.8	10.9
	hard	all	5.8	9.7
		< 3	5.8	9.5
		> 3	5.7	10.6

Table 5.2: Measurements of *VERITAS* PSF (39% and 68% containment radii, r_{39} and r_{68} respectively) from observation of the Crab Nebula, for selected zenith angle ranges, gamma-hadron separation cuts, and energy ranges (see text for descriptions).

may be calculated numerically from the values of A_{rel}, σ_1, and σ_2.

The results of the fits are given in Table 5.2. The PSF is seen to increase at larger zenith angle and decrease with harder selection cuts. While the higher-energy events show an improved PSF over lower energies when using moderate-spectrum cuts, no such improvement is seen with the hard cuts. This may be due to requiring a larger Size value with harder cuts, so that all energies are better reconstructed against fluctuations.

5.3 Morphology of CTA 1

The CTA 1 data were analyzed with standard *VERITAS* procedures, using hard-spectrum selection cuts and a θ^2 cut of 0.055 degree^2 as is typically used for extended source analysis. The final statistical analysis was divided between events above and below the separation energy described in Section 5.1. The resulting uncorrelated,

acceptance-corrected excess maps were fit with an asymmetric, two-dimensional Gaussian of centroid (x_0, y_0), constant offset C, magnitude A, and intrinsic semi-axes σ_X and σ_Y, where the semi-axis defined by σ_X forms an angle ϕ with the x-axis of the coordinate system (taken as to the right in the camera coordinates, or east in sky coordinates). The equation used for the fit is

$$G(\vec{r}) = C + A \ \exp\left(-\frac{1}{2}\left[\frac{x_\phi^2}{(\sigma_X^2 + \sigma_{\rm PSF}^2)} + \frac{y_\phi^2}{(\sigma_Y^2 + \sigma_{\rm PSF}^2)}\right]\right), \tag{5.2}$$

using the shorthand parameters.

$$x_\phi = (x - x_0)\cos(\phi) - (y - y_0)\sin(\phi), \tag{5.3}$$

$$y_\phi = (x - x_0)\sin(\phi) + (y - y_0)\cos(\phi). \tag{5.4}$$

This method assumes the intrinsic signal is convolved with the point spread function, modeled as a single Gaussian of width $\sigma_{\rm PSF}$ which is held constant throughout the fitting. The value of $\sigma_{\rm PSF}$ is taken as the appropriate value of the 39% containment radius r_{39} from Table 5.2. This assumption of a Gaussian PSF allows a simpler fit equation, given above, as the convolution of two Gaussians is another Gaussian. Assuming the intrinsic signal is described by a Gaussian of width $\sigma_{\rm int}$, then the total convolved image has a variance $\sigma_{\rm total}^2 = \sigma_{\rm int}^2 + \sigma_{\rm PSF}^2$.

The results of the fitting are presented in Table 5.3. The low- and high-energy morphologies largely agree to within errors, with the larger errors on the low-energy fit indicating that a higher separation energy may be preferable. A larger difference may be seen by using several energy ranges, which may be possible with more data for improved statistics.

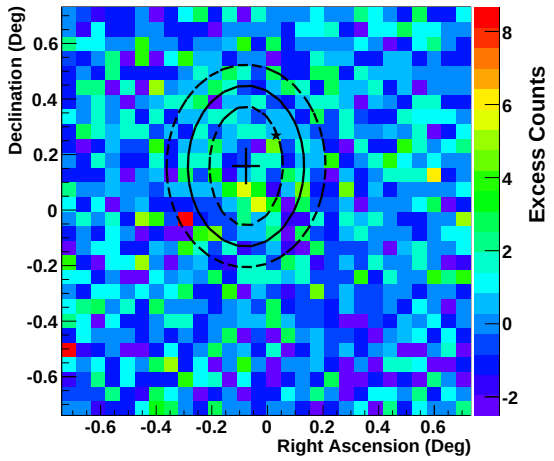

(a) Energies $E < 3$ TeV

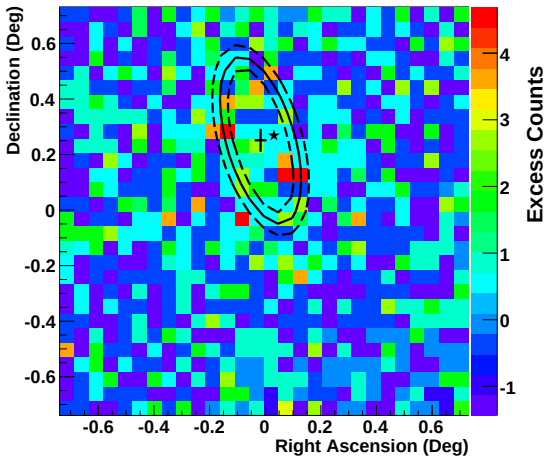

(b) Energies $E > 3$ TeV

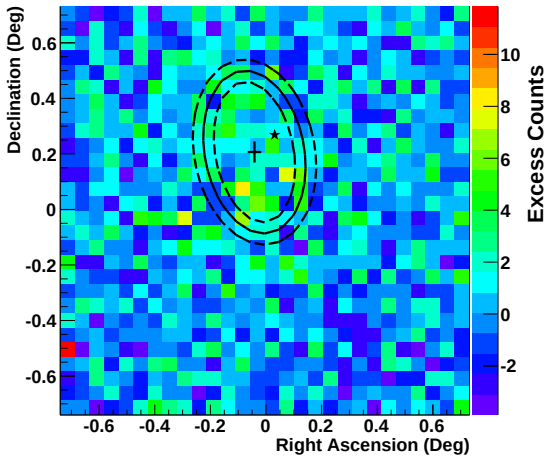

(c) Full dataset

Figure 5.1: Acceptance-corrected uncorrelated excess maps of the region around CTA 1, with a bin size of 0.05°. The maps are for energies below 3 TeV, above 3 TeV, and the combined dataset. The results of fitting a two-dimensional, asymmetric Gaussian to each map are shown, with uncertainties in the extents marked by dashed lines. The uncertainties on the centroids are marked by crosses. The pulsar position is marked by a star. Coordinates are degrees offset from the center of the SNR. North is up and east is to the right.

Parameter	Energy range		
	all	< 3 TeV	> 3 TeV
centroid:			
RA (J2000)	1.51 ± 0.08	1.39 ± 0.17	1.59 ± 0.07
Decl (J2000)	73.00 ± 0.04	72.90 ± 0.07	73.00 ± 0.04
major axis	0.25 ± 0.03	0.24 ± 0.06	0.26 ± 0.04
minor axis	0.15 ± 0.03	0.18 ± 0.07	0.10 ± 0.02
orient. angle	10 ± 11	0 ± 42	16 ± 7

Table 5.3: Measurement of the energy-dependent TeV morphology of the PWN in CTA 1. All parameters are given in degrees. The orientation angle is given as the angle of the major axis west of north.

Chapter 6

Simple Cylindrical Model of PWNe

Pulsar wind nebulae are complex systems with multiple known morphologies. Numerous efforts have been made to model these objects, either individually or as a class. The models use various methods to solve for the structure and evolution of PWNe, with varying simplifying assumptions and symmetries. In this chapter, I summarize some of the previously published models, as well as outline a new multi-zone, cylindrical model. The application of this model to the *VERITAS* observations of CTA 1 will be described in Chapter 7.

6.1 Previous models of PWNe

6.1.1 Green's function approach

Ideally, one would like to find an analytic expression for the differential particle density everywhere within the PWN throughout it's lifetime, given the relevant forms of particle injection, transport, cooling, and escape. We shall denote the density as $N(E, \vec{r}, t)$, so that $N\,dV\,dE$ is the total number of particles with a volume dV with energies between E and $E + dE$.

Ginzburg and Syrovatskii (1964) used a transport equation of the form

$$\frac{\partial N}{\partial t} = Q(E, \vec{r}, t) + D\nabla^2 N - \frac{\partial}{\partial E}(bN) - \frac{N}{T} \tag{6.1}$$

to address the diffusive transport of cosmic rays of a single type (e.g. electrons), where $Q(E, \vec{r}, t)$ is a source term, D is the spatial diffusion constant, $b = \dot{E}$ is the rate of energy losses/gains due to various cooling/acceleration mechanisms, and T is the mean lifetime of the particle with respect to "catastropic" losses (e.g. escape from the region of interest). Note that this equation does not account for systematic, bulk motion of the material (i.e. advection terms of the form $\nabla \cdot (N\vec{u})$, with $\vec{u}(\vec{r}, t)$ the bulk velocity.)

An analytic solution may be found if one assumes that coefficients of Equation 6.1 are independent of spatial coordinates and time. If we assume that the diffusion occurs by scattering in a magnetic field, cooling occurs via synchrotron and IC mechanisims, and that we ignore acceleration ($b < 0$), then the above condition implies that both the magnetic field strength and seed photon populations are also independent of space and time. These requirements are certainly satisfiable for IC scattering of the CMB photons. However, the assumption of a static, homogeneous magnetic field strength is almost certainly of limited applicability for actual PWNe. Along with the lack of advective terms, this model will therefore have limited applicability to PWNe, although it may serve as an analytic cross-check for other methods.

Using the substitutions

$$\lambda(E, E') = \int_{E'}^{E} \frac{D(E)}{b(E)} dE, \tag{6.2}$$

$$\tau(E, E') = \int_{E'}^{E} \frac{1}{b(E)} dE, \tag{6.3}$$

one can find that the Green's function solution for Equation 6.1 is

$$G(E,\vec{r},t,E',\vec{r}',t') = \frac{1}{|b(E)|(4\pi\lambda)^{3/2}} \exp\left[-\frac{\tau}{T} - \frac{(\vec{r}-\vec{r}')^2}{4\lambda}\right] \delta(t-t'-\tau). \qquad (6.4)$$

The delta function reflects the deterministic nature of the particle cooling, with a one-to-one correspondence between energy E at the current time and a single energy $E'(t')$ at a previous time t'. The general solution can then be solved by the standard method of Green's functions,

$$N(E,\vec{r},t) = \int d^3\vec{r}' \int dE' \int_{-\infty}^{t} dt' Q(E',\vec{r}',t') G(E,\vec{r},t,E',\vec{r}',t'). \qquad (6.5)$$

If we assume injection from a point source following a path $\vec{r}_S(t)$, so that

$$Q(E',\vec{r}',t') = Q_0(E',t')\delta[\vec{r}' - \vec{r}_S(t')], \qquad (6.6)$$

then the time and spatial integrals of Equation 6.5 are trivial, given the delta functions of Equations 6.4 and 6.6. This leaves only the integral over energy, which may be performed numerically.

6.1.2 Hydrodynamic models

A full treatment of the hydrodynamical evolution of a gas involves the simultaneous solution of several partial differential equations for the particle distribution function, taking into account the spatial, velocity (energy), and temporal dependence over a broad range of scales. Obtaining a solution is generally difficult at best for analytic solutions, and computationally expensive for numerical solutions. An early spectral model was created by Kennel and Coroniti (1984) to describe the Crab Nebula using a spherical, steady-state, adiabatic wind with a toroidal magnetic field. By solving a series of magnetohydrodynamic equations at the standing termination shock and

setting boundary conditions at the outer edge of the nebula, they found solutions for the radial distributions of the bulk flow speed and the magnetic field, as well as the best fit for the ratio of magnetic field energy to particle energy, the σ parameter of Equation 3.20, with $\sigma \sim 3 \times 10^{-3}$, indicating a strongly particle dominated wind. For such low values of σ, they found that the bulk wind speed would follow a radial distribution of $\beta\Gamma \sim r^{-2}$ out to a characteristic radius before approaching an asymptotic value of $\beta\Gamma \sim \sigma$, where $\Gamma = (1 - \beta^2)^{-1/2}$ and $\beta = u/c$ for a bulk wind speed u. Similarly, the magnetic field strength would scale as $B \sim r$ out to a characteristic radius before falling as $B \sim r^{-2}$.

A numerical treatment by van der Swaluw et al. (2001) used the Versatile Advection Code (VAC; Tóth 1996) to solve the equations of non-relativistic gas dynamics in spherical symmetry, assuming a pulsar that remains centered within an expanding SNR. The PWN and SNR material were treated as a single fluid. These simulations could trace the structure of the PWN as it evolves (an example of their results is shown in Figure 6.1), and formed the basis for later models which introduced additional factors such as a toroidal magnetic field (van der Swaluw, 2003) or cylindrical symmetry with a large pulsar kick velocity (van der Swaluw et al., 2003, 2004). However, these models do not include information on the spectral composition of the particles, nor the radiative losses and subsequent emission profiles.

Blondin et al. (2001) used an adapted version of the VH-1 hydrodynamic code to study the PWN/SNR interaction as a two-fluid model, both in 1- and 2-dimensional treatments. They paid particular focus to the instabilities at the PWN wind/SNR ejecta interface and the results of an asymmetric reverse shock for late PWN evolutionary phases. Similar to van der Swaluw et al. (2001), their model did not account for the spectrum of particle energies, nor did they include a magnetic field and radiative losses.

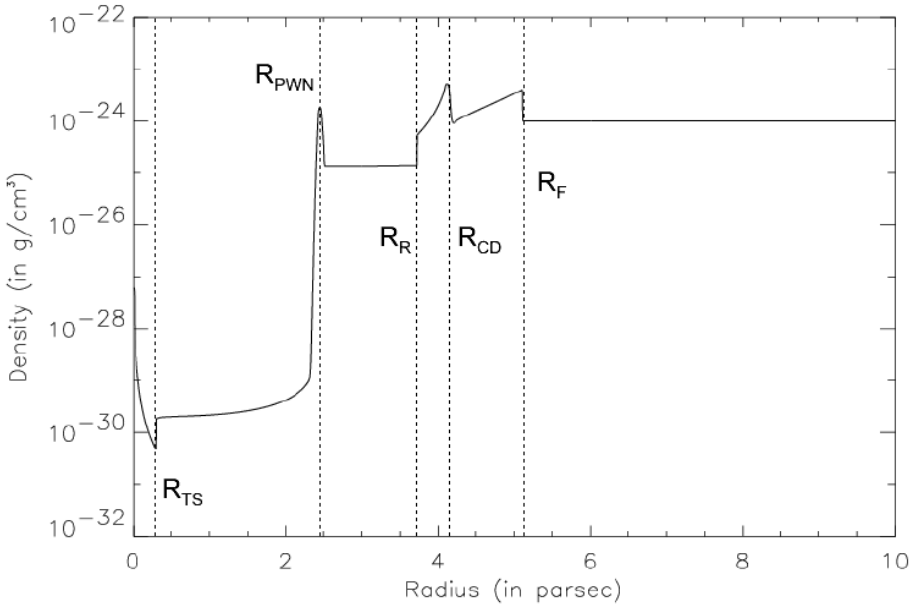

Figure 6.1: Radial density profile of a young PWN inside an expanding SNR, adapted from van der Swaluw et al. (2001). Moving from left to right, the discontinuities represent the pulsar wind termination shock (R_{TS}), the forward shock of the PWN ($R_{\rm PWN}$) with a swept-up shell of ejecta, the SNR reverse shock ($R_{\rm R}$), a contact discontinuity between shocked ejecta and shoacked ISM ($R_{\rm CD}$), and the SNR forward shock ($R_{\rm F}$).

6.1.3 One-zone models

A variety of models have been created which treat the nebula as a spherical bubble and solve the spectral evolution of the particle populations with either analytic or semi-analytic methods. So-called "one-zone models" treat the properties of the PWN, both the spectral distribution of the particles and the dynamical properties of the gas (e.g. pressure), as constant throughout the nebula.

Tanaka and Takahara (2010, 2011) used a uniform expanding sphere to model several young (age < 10 kyr) PWNe. The spectrum of energetic particles injected by the termination shock is parameterized as a broken power-law, normalized so that the integrated particle energy injected at time t is a constant fraction of the spin-down luminosity $L(t)$. Cooling methods include synchrotron emission, IC losses on CMB, IR, and optical photon fields, and adiabatic expansion. They found that a small fraction (a few $\times 10^{-3}$) of the spin-down power goes into the magnetic field, a broken power-law spectrum of injected electrons is preferred, and the inverse Compton emission is dominated by scattering of IR radiation ($T \sim 40$ K) with an energy density of $0.5 - 2.0$ eV cm^{-3}.

Gelfand, Slane, and Zhang (2009) (hereafter GSZ) treated the PWN as a uniform sphere inside a larger, evolving spherical SNR, which is itself expanding into a uniform ISM. (This is the model used in the discussion of Chapter 4, and so will serve as a comparison with the model described here and in Chapter 7.) This semianalytic model predicts both the expansion properties of the nebula (radius and expansion velocity) and its emission spectrum as a function of time.

In the GSZ model, the density, velocity, and pressure profiles of the SNR ejecta are evolved using the 1-dimensional semi-analytic results of Truelove and McKee (1999). Meanwhile the pulsar injects its spin-down energy into the nebula divided between magnetic fields, electron-position pairs, and ions, as in Equation 3.23, with the relative strengths of the three components left as free parameters. These components are

injected at a termination shock located at radius R_{TS} given by Equation 3.21. The magnetic field strength and particle spectra are assumed to be constant throughout the nebula from radius R_{TS} out to a containment radius $R_{\rm PWN}$, where a thin shell of swept-up SNR ejecta is assumed to sit. The combined pressures of the particles and fields within the nebula is compared to the pressure of the ejecta just outside the shell to determine whether the nebula expands or contracts. If the nebula contracts to a sufficiently small size that the pulsar escapes through the shell, injection of energy ceases until the nebula re-expands to encompass the pulsar again (the PWN remains centered within the SNR, even as the pulsar moves outward).

The particles lose energy through both synchrotron emission (possibly modified by self-absorption for periods of high particle density, using a monochromatic approximation) and inverse Compton scattering (accounting for Klein-Nishina effects). Both particles and magnetic field also lose/gain energy from adiabatic expansion/compression. For ultrarelativistic particles of adiabatic index 4/3, the total particle energy E_p in a nebula of pressure P and volume V scales as $E_p = 3PV$, and $PV^{4/3}$ is constant, so $E_p \sim V^{-1/3}$ or $E_{\rm PWN} \sim R_{\rm PWN}^{-1}$. The magnetic field energy scales in identical fashion, with the field strength then calculated from $E_B = VB^2/8\pi$. The losses are shared equally across the nebula, so all particles experience an adiabatic cooling rate of

$$\dot{E}_{ad}(t) = -\frac{\dot{R}(t)}{R(t)}E \tag{6.7}$$

Given the various energy-loss rates and size of the nebula, the particle spectra and subsequent emission are then calculated at each time-step. By testing the model on the properties of the Crab Nebula and its parent pulsar, the authors were able to replicate the size of the nebula and its general spectral shape, but with radio, X-ray, and TeV luminosities off of an order of magnitude.

A model by Bucciantini et al. (2011) is similar to that of GSZ, with a spherical PWN centered within an SNR described by the results of Truelove and McKee (1999).

While the overall energetics of the PWN ignore radiative losses, the emission spectra are calculated assuming monochromatic synchrotron emission and inverse Compton scattering of CMB, synchrotron, and local IR/optical photon fields, as well as π^0 decay from a small population of monoenergetic ions. They note that the model achieves "surprisingly" good agreement with observation, considering that the assumption of efficient mixing of particle populations inherent to one-zone models is not likely valid for higher-energy particles, stressing that more detailed models should be used to accurately describe the region near the termination shock. The authors also note that the inclusion of a hadronic component to the wind is generally unnecessary to achieve a successful fit, and that including it tends to increase the required injection energy above that of the pulsar spin-down power.

6.1.4 Multi-zone model

Van Etten and Romani (2011) used a multi-zone model to fit the spatial variations of TeV and X-ray spectra in the PWN HESS J1825-137. Associated with PSR J1826-1334, HESS J1825-137 shows an angular extent in TeV energies of 1°, with a centroid $0^\circ.3$ from the pulsar and spectral softening with increasing distance from the pulsar (Aharonian et al., 2006c). Van Etten and Romani model the object as a series of 12 partial spherical shells, or "nested bowls", with each section expanding away from the central pulsar. The inner-most shell at a given time (i.e. the one containing the pulsar) sees an injected particle spectrum of the form $dN/dE \sim E^{-p}e^{-E/E_{\rm cut}}$, with the normalization varying with the pulsars spin-down luminosity.

All shells simultaneously undergo adiabatic and radiative cooling, as well as diffusion between neighboring shells. The radial wind and magnetic field profiles vary with distance and time such that $v(r,t) \sim r^\alpha t^{-\alpha}$ and $B(r,t) \sim r^\beta \dot{E}(t)$, with no relation between α and β to conserve magnetic flux. Diffusion is implemented using a Bohm-like scaling with the mean free path $\lambda = aE$. The scaling parameter

a is a free parameter, with no explicit relation to the particle gyroradius in the local magnetic field. In all, there are seven fit-parameters: $\alpha,\ \beta,\ p,\ E_{cut},\ a$, the initial pulsar spin period P_0, and braking index n. Their final fit values include $\alpha = -0.51,\ \beta = -0.69,\ n = 1.9,\ p = 2.24$, and $a = 0.018$ pc/TeV.

6.2 Simple Cylindrical Model

6.2.1 Overview

The previous models of PWNe mentioned above have each made at least one of several assumptions:

Spherical symmetry

At its simplest, this assumption reduces a 3-dimensional system to only a single radial dimension, greatly reducing the computational complexity. However, numerous systems are known to exhibit non-spherical geometry. A pulsar with a kick velocity seems to allow for another symmetry: a cylindrical system with the pulsar's velocity vector defining the axis of symmetry. If particles can escape outside the main PWN, those that escape ahead of the pulsar will evolve differently than those escaping in the opposite direction as the pulsar catches up to them.

One-zone treatment

The values of the particle distribution and magnetic field are treated as uniform throughout the nebula. In terms of the particle populations, this assumes instantaneous transport throughout the nebula from the source, with efficient mixing of material throughout. This prohibits any form of energy-dependent morphology.

Lack of radiative losses

The models generally all allow for adiabatic losses due to the expansion of the nebula, with the energy loss rate scaling as $\dot{E} \sim E$. However, radiative losses from synchrotron and inverse Compton emission will scale as $\dot{E} \sim E^2$ and become particularly important for the highest energy particles.

The aim of this work is to develop a model without these assumptions (or modifications to them). The model is used to solve for the time evolution of the particle density $N(E, \vec{r}, t)$ throughout the PWN. Assuming cylindrical symmetry, the distribution is advanced forward in time using a finite-difference equation on a grid of two spatial dimensions (axial z and radial ρ) and one dimension for energy E. The magnetic field strength and bulk wind velocity are assumed to be radially symmetric about the pulsar, which moves along the axial direction at a constant speed V_p. The spin-down luminosity of the pulsar evolves with time, and is injected into the nebulae via the magnetic field and energetic electron-positron pairs, with a constant ratio between the energy fluxes of the two components. The electrons cool via synchrotron, inverse Compton, and adiabatic losses. The synchrotron and IC specific emissivities are then integrated along the line of sight to determine the fluxes at the observer. Compared to the previous work, I make some simplifying assumptions. I assume that the effects of the surrounding SNR on the PWN system are negligible (e.g. a bow shock is not formed by the pulsar moving through ejecta), the bulk wind speed and magnetic field are continuous throughout the region (no confinement at the edge of the PWN), and the spin evolution of the pulsar is partially fixed by the observations of the current spin-parameters.

6.2.2 Pulsar evolution

The values of the pulsar spin period P and its derivative $\dot{P}$ at the current era are fixed by observation. From these, the current spin-down luminosity $\dot{E}$ and the characteristic

age τ_C can then be found via Equations 3.1 and 3.7, respectively. By choosing a braking index n and current age of the pulsar T, the entire history of the spin-down parameters can be determined from Equations 3.3, 3.5, and 3.8. The phenomenon of pulsar glitches will be ignored, as these ill-understood events are rare, of short duration, and of small magnitude, with $\Delta\nu/\nu \sim 10^{-11} - 10^{-5}$ (Espinoza et al., 2011).

As mentioned in Section 3.1.2, the braking index has been confidently measured for very few pulsars, with $2 < n < 3$. Therefore, the current model will fix the index at the canonical value of 3. An important consequence of this decision is that the true age of the system must be less than the current characteristic time (see Equation 3.8). The age, which is the only free parameter remaining describing the pulsar spin-down history, may be estimated from observations (e.g. via a Sedov analysis of the SNR shell (Slane et al., 2004)), which reduces the parameter space that needs to be investigated.

The spin down luminosity of the pulsar is injected into the nebulae in two components, the magnetic field and a wind of electron-positron pairs. (As the emission from these particles is indistinguishable, they shall hereafter be called simply electrons.) Using the notation of Equation 3.23, this implies that $\eta_B = 1 - \eta_E$ and $\eta_I = 0$. The parameter η_E (or, equivalently, η_B) will be left as a free parameter, constant trough the lifetime of the pulsar. I assume that the injection of energy takes place at the termination shock, at a radius R_{TS}. If the magnetic field component of energy density $U_B = B^2/8\pi$ is carried to the shock in a relativistic wind, then the corresponding energy injection rate is

$$\dot{E}_B = 4\pi c R_{TS}^2 U_B, \tag{6.8}$$

$$\Rightarrow \eta_B \dot{E} = \frac{c R_{TS}^2 B^2}{2}, \tag{6.9}$$

resulting in a magnetic field at the termination shock of

$$B(R_{TS},t) = \sqrt{\frac{2\eta_B \dot{E}(t)}{cR_{TS}^2}} \sim 265 \left(\frac{\eta_B \dot{E}}{10^{36}\ \mathrm{erg/s}}\right)^{1/2} \left(\frac{R_{TS}}{0.01\ \mathrm{pc}}\right)^{-1}\ \mu\mathrm{G}. \tag{6.10}$$

As for the electron pair component of the wind, if $Q(E,\vec{r},t)dE$ is the number density of particles injected into the system per unit time between energies E and $E+dE$, then the rate of injection of particle energy into the nebula is

$$\eta_E \dot{E}(t) = \int_V \int_0^\infty E\ Q(E,\vec{r},t)\ dE\ d^3r \tag{6.11}$$

If the grid spacing is much larger than the size of the termination shock, then we may approximate the injection site as a point source. For simplicity, we assume a power-law spectrum of index α, with limiting energies E_{min} and E_{max} which will remain fixed with time. If the pulsar is located at position $\vec{r}_S(t)$ at time t, then the source term takes the form

$$Q(E,\vec{r},t) = \begin{cases} Q_0(t) E^{-\alpha} \delta(\vec{r}-\vec{r}_S) & \text{for } \mathrm{E_{min}} \leq \mathrm{E} \leq \mathrm{E_{max}}, \\ 0 & \text{otherwise.} \end{cases} \tag{6.12}$$

The normalization constant Q_0 is fixed by using Equation 6.11:

$$Q_0(t) = \begin{cases} \dfrac{\eta_E \dot{E}}{\ln(E_{\mathrm{max}}/E_{\mathrm{min}})} & \text{for } \alpha = 2, \\ \dfrac{(2-\alpha)\eta_E \dot{E}}{E_{\mathrm{max}}^{2-\alpha} - E_{\mathrm{min}}^{2-\alpha}} & \text{otherwise.} \end{cases} \tag{6.13}$$

The above equation could be made slightly more general by including the possibility of an underlying low-energy, thermal component for the wind. An additional

component could be accounted for by including an additional efficiency factor η_{NT} in the numerator of Equation 6.13, which would parameterize what fraction of the wind is accelerated into the non-thermal component. For instance, using particle-in-cell (PIC) models of a relativistic shock, Spitkovsky (2008) found that the downstream particle spectrum should be a relativistic Maxwellian with a power-law tail, a form applied to several PWNe by Fang and Zhang (2010) using an evolutionary model similar to Gelfand et al. (2009). However, the multi-zone modelling of Van Etten and Romani (2011) found that including a relativistic Maxwellian component decreased the goodness-of-fit to their X-ray and TeV data, while also requiring a very short spin-period P_0 and over-predicting the GeV emission (which was not included in the fitting procedure). Combining this with the fact that the one-zone GSZ model in Chapter 4 found an adequate fit to the data using only a (broken) non-thermal injection population, we will avoid the complication of another component and fix $\eta_{NT} = 1$ for the present study.

The spectral index of the injected particle distribution is left as a free parameter. The spectral index of particles accelerated in a non-relativistic shock is commonly given as $\alpha = (r + 2)/(r - 1)$, where r is the compression ratio, the ratio of the downstream density to upstream density. For strong, nonrelativistic shock, $r \simeq 4$ and $\alpha \simeq 2$. However, for relativistic shocks, the effective compression ratio and spectral index are highly dependent on a number of factors, including the magnetic obliquity (the angle between the mean upstream magnetic field and the shock normal), the upstream bulk flow speed, and the ratio of the diffusive mean free path to the particle gyroradius (see Figure 6.2 for an illustration).

6.2.3 Diffusion and advection for a moving source

As the particles and fields escape from the termination shock, they form an extended nebula. There are two methods of transporting particles throughout this extended

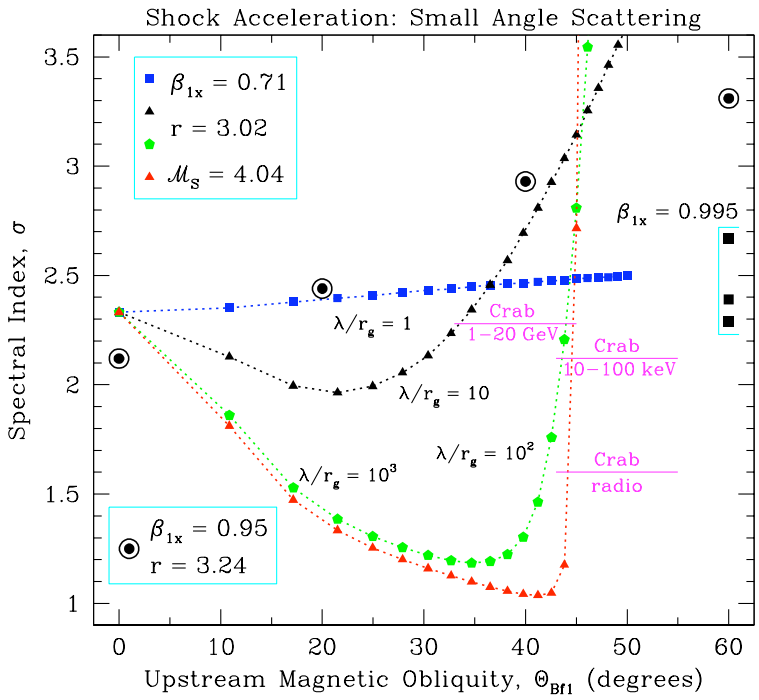

Figure 6.2: Sample of spectral indices from Monte Carlo simulations of particles accelerated in relativisitic shocks of compression ratios $r = 3.02$ and $r = 3.24$ and varying magnetic obliquities Θ_{Bf1} (Figure 4 from Baring (2011)). The colored shapes are for upstream speed $\beta_{1x} = u_{1x}/c = 0.71$, with different ratios of the mean free path λ to the gyroradius r_g (see Section 6.2.3). Dotted circles represent $\beta_{1x} = 0.95$ and $\lambda/r_g = 5$. Black squares represent $\beta_{1x} = 0.995$ and, from bottom to top, $\lambda/r_g = 1, 3, 6$. The canonical spectral index for relativistic shock acceleration is $\sim$2.23. Spectral indices required to match the emission from the Crab Nebula at various wavebands are also indicated.

nebulae: advection via the bulk flow of a wind and diffusion of charged particles within the magnetic field. If the particles within the nebula experience a bulk velocity field $\vec{u}(\vec{r}, t)$, then the change in their distribution is given by the divergence of the quantity $\vec{u}n$:

$$\left(\frac{\partial N}{\partial t}\right)_{\text{adv}} = -\nabla \cdot (\vec{u}N)\,. \tag{6.14}$$

We'll assume that the velocity field is instantaneously radially symmetric about the position of the pulsar, falling off as a power law: $\vec{u}(r) \sim r^{-a}\hat{r}$. The inner boundary of this field occurs at the termination shock radius R_{TS}, where the bulk speed is $\sim$c/3 for a relativitic shock with compression ratio $r = 3$.

While the index a could be left as a free parameter, in the interest of computing time we'll assume the value is fixed by the observed size of the PWN. Using the scaling $R_{\text{PWN}}(t) \sim t^{6/5}$ of Equation 3.28, then the velocity of the forward boundary $\dot{R}_{\text{PWN}}$ for a nebula of age T is $\dot{R}_{\text{PWN}}(T) \sim 1.2R_{\text{PWN}}/T$. Selecting this as the bulk velocity at the outer radius, and using the inner boundary condition at the termination shock, R_{TS}, the index a is given by

$$a = -\frac{\ln(18R_{\text{PWN}}/5cT)}{\ln(R_{\text{PWN}}/R_{\text{TS}})}. \tag{6.15}$$

The selection of $u(R_{\text{PWN}}) = \dot{R}_{\text{PWN}}$ has been used in earlier models including those of Rees and Gunn (1974) and Van Etten and Romani (2011).

Particles may also be transported throughout the nebula via diffusion, scattering off of inhomogeneities in the magnetic field. As the relevant length scale for such scatterings is the particles gyroradius λ, a choice must be made relating this quantity to the diffusion constant D, a question that is also relevant in the theories of both astrophysical particle acceleration (e.g. Casse and Marcowith, 2005) and cosmic ray transport (e.g. Aloisio and Berezinsky, 2004). Possible choices for the diffusion regime include Bohm scaling, where the scattering mean-free path is equal to the particle

gyroradius ($D_{\rm Bohm} = c\lambda/3$), a Bohm-like scaling ($D = AD_{\rm Bohm}$, with $A > 1$), and a Kolmogorov scaling ($D \sim \lambda^{1/3}$). As the most-efficient scattering occurs with the Bohm scaling (which also has the simplest parameterization), this will be the choice for the present simulations.

As with the bulk velocity field, the magnetic field strength B is assumed to be radially symmetric about the pulsar and falling off as power law: $B(r) \sim r^{-b}$. The index b may again be left as a free parameter (e.g. Van Etten and Romani, 2011), or it may be tied to the bulk velocity index a (e.g. Aliu, 2007; Kennel and Coroniti, 1984). If the large-scale magnetic field is toroidal [$\vec{B} \sim B(r)\hat{\phi}$], as evidenced by the torus and jet structures seen in many young PWNe (Gaensler and Slane, 2006), conservation of magnetic flux stipulates

$$0 = \nabla \times (\vec{u} \times \vec{B}) \tag{6.16}$$

$$\Rightarrow 0 = \frac{\partial}{\partial r}[r\ B(r)\ u(r)] \tag{6.17}$$

$$= B_0\ u_0\ \frac{\partial}{\partial r}(r^{1-b-a}). \tag{6.18}$$

We therefore have the requirement that $b = 1 - a$, where a is fixed by Equation 6.15. Again, for simplicity we choose to use this formulation. The normalization of the scaling is set by using the value of the magnetic field at the termination shock given by Equation 6.10. Also, in order to keep the magnetic field from falling to unreasonably small values at large distances, a minimum value of 3 μG is required.

With the above assumptions, the structures of the magnetic field and the advective wind are fully determined by a few parameters: the current size of the PWN $R_{\rm PWN}$, the radius of the termination shock $R_{\rm TS}$, the true age of the system T, and the spin-parameters of the pulsar to determine the magnetic field strength at $R_{\rm TS}$ (as described in Section 6.2.2).

6.2.4 Cooling

As they are transported away from the termination shock, particles cool through both radiative and adiabatic losses. The radiative losses occur through synchrotron and inverse Compton processes. As previously mentioned in Chapter 1, the average synchrotron energy loss-rate for an electron with Lorentz factor γ, assuming an isotropic distribution of pitch angles, is

$$\left(\frac{dE}{dt}\right)_{\text{sync}} = -\frac{4}{3}\sigma_T c\beta^2\gamma^2 U_B, \tag{6.19}$$

and the magnetic field energy density is $U_B = B^2/8\pi$. For a particle of energy E, this rate may be parameterized as $\dot{E} = -\alpha E^2$ and calculated at any position within the nebula once the magnetic field profile is known. Similarly, the average loss rate for IC emission in the Thomson regime is

$$\left(\frac{dE}{dt}\right)_{\text{IC}} = -\frac{4}{3}\sigma_T c\beta^2\gamma^2 U_{ph}, \tag{6.20}$$

where U_{ph} is the energy density of the seed photon field. For scattering on the CMB, this energy density will have a known value, constant in both space and time over the lifetime of the PWN. This is a great simplification compared to the energy densities of other external photon fields, the internal synchrotron photon field, and the magnetic field. Furthermore, for most SNRs and PWNe the contributions from IC scattering of the diffuse-IR and self-Compton are small, or at most on the order of the CMB inverse Compton emission. Thus, in addition to being a simplifying assumption limiting ourselves to the IC scattering of the CMB is a good approximation for the total scattering. As the two modes of radiative cooling have the same form other that the energy field being considered, we combine their contribution to the overall loss term

as

$$\left(\frac{dE}{dt}\right)_{\rm rad} = -\alpha\ (1+\chi)E^2, \tag{6.21}$$

where $\chi = U_{ph}/U_B$ is a "Compton correction factor".

As noted in Chapter 1, when the electron energy E and seed photon energy $h\nu$ are large enough [i.e. $h\nu E \gtrsim (mc^2)^2$], the full Klein-Nishina cross-section must be used; while more energy is lost in a single interaction, the probability of the interaction decreases. We note that more energetic photon fields (e.g. IR and synchrotron) are suppressed. We account for the Klein-Nishina effect across the electron spectrum by modifying the form of the effective energy density. Combining the particle energies into a dimensionless parameter $x \equiv h\nu E/(mc^2)^2$, we define the scaling factor $f(E, h\nu)$ as the ratio of the full Klein-Nishina cross-section to the Thomson cross-section (Figure 6.3):

$$f(E, h\nu) = \frac{\sigma_{KN}}{\sigma_T} \tag{6.22}$$

$$= \frac{3}{8x}\left[\left(1 - \frac{2}{x} - \frac{2}{x^2}\right)\log(1+2x) + \frac{4}{x} + 2x\frac{1+x}{(1+2x)^2}\right]. \tag{6.23}$$

If the seed photons have a number density per frequency interval $n(\nu)$, then one can take the Klein-Nishina effect into account by assuming that the cross-section is given by σ_T but the energy density of seed photons is modified and can be replaced with an effective energy density

$$U_{ph}(E_e) = \int_0^\infty h\nu\ n(\nu)\ f(E_e, h\nu)\ d\nu. \tag{6.24}$$

This is the value of U_{ph} that is used in calculating the correction factor of Equation 6.21.

Adiabatic losses arise from the large-scale expansion of the nebula, with the resulting work coming at the expense of the nebulae's internal energy. As the particles

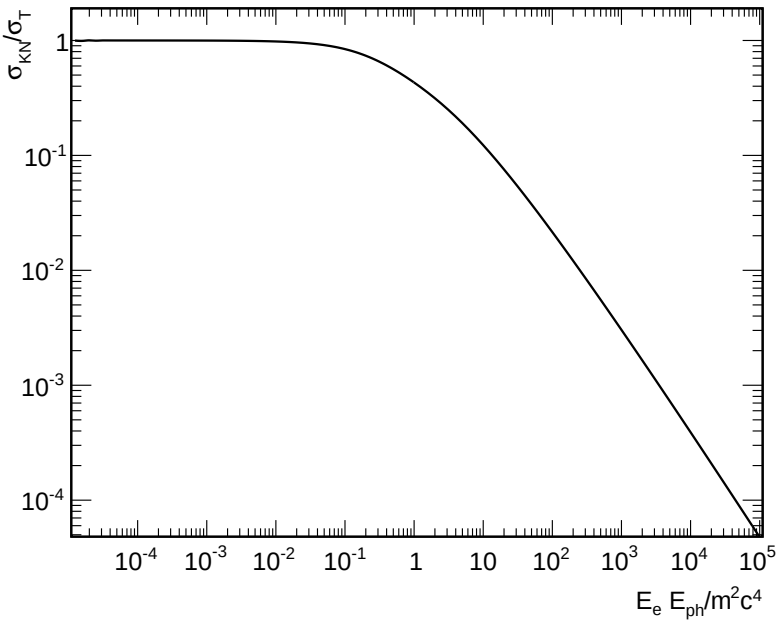

Figure 6.3: The full Klein-Nishina cross-section normalized to the Thomson cross-section, used in calculating the seed photon energy density in inverse Compton cooling.

inside the nebula are relativistic, their adiabatic index is $\gamma = 4/3$. Therefore, for a volume V with pressure P, the quantity $PV^{4/3}$ is constant and the pressure is related to the nebula's energy U by $P = U/3V$. By the first law of thermodynamics, for an adiabatic system,

$$dU = -P\ dV \tag{6.25}$$

$$\Rightarrow \dot{U} = -\frac{U}{3}\frac{\dot{V}}{V}. \tag{6.26}$$

As noted by (Kennel and Coroniti, 1984), the sound speed within the relativistic gas of the nebula is $\sim c/\sqrt{3}$, so any pressure perturbations are dissipated on a time-scale of a few years, which is much shorter than the time-scale of expansion, and the pressure may be assumed to remain uniform across the entire PWN. If we therefore take $\dot{V}$ to represent the expansion of the nebula as a whole (e.g. Gelfand et al., 2009;

van der Swaluw et al., 2001; Van Etten and Romani, 2011), and assuming that the nebula maintains a roughly spherical shape as it expands (ignoring deformation from ram pressure or an SNR reverse shock), then $\dot{V} = 3V\dot{R}_{\rm PWN}/R_{\rm PWN}$ and

$$\dot{U} = -U\frac{\dot{R}_{\rm PWN}}{R_{\rm PWN}}. \tag{6.27}$$

If this loss is shared among all the particles in the nebula, each particle then sees an energy loss rate of

$$\left(\frac{dE}{dt}\right)_{\rm ad} = -\left(\frac{\dot{R}_{\rm PWN}}{R_{\rm PWN}}\right)E \tag{6.28}$$

$$\equiv -\beta_{ad}E. \tag{6.29}$$

Combining this with the radiative loss rate given by Equation (6.21), the total change in the particle distribution from cooling losses is

$$\left(\frac{\partial N}{\partial t}\right)_{\rm cool} = -\frac{\partial}{\partial E}\left[\left(\dot{E}_{\rm ad} + \dot{E}_{\rm rad}\right)N\right] \tag{6.30}$$

$$= \frac{\partial}{\partial E}\left[\beta_{ad}EN + \alpha(1+\chi)E^2N\right]. \tag{6.31}$$

6.2.5 Numerical method

Accounting for each of the processes above, and assuming the pitch angles of the particle are randomized at the termination shock so that we may work in energy-space rather than momentum-space, the total evolution of the particle density is given by

$$\frac{\partial N}{\partial t} = Q + \nabla\cdot(D\nabla N - \vec{u}N) - \frac{\partial}{\partial E}\left[\left(\dot{E}_{\rm ad} + \dot{E}_{\rm rad}\right)N\right] \tag{6.32}$$

The terms on the right-hand side represent: the changes due to the injection of new particles at the termination shock, the transport of particles via diffusion and ad-

vection, and the cooling of particles via adiabatic and radiative losses, respectively. As we will consider particle energies ranging over several orders of magnitude, it is advantageous to first change to a logarithmic scaling in energy. Using the parameters

$$y \equiv \ln E, \tag{6.33}$$

$$G(y) \equiv N(E)\frac{dE}{dy} \tag{6.34}$$

$$= E\ N(E), \tag{6.35}$$

Equation 6.32 becomes

$$\frac{\partial G}{\partial t} = Qe^y + \nabla \cdot (D\nabla G - \vec{u}G) - \frac{\partial}{\partial y}\left[\beta_{ad}G + \alpha(1+\chi)e^y G\right]. \tag{6.36}$$

Equation 6.36 is solved on three-dimensional grid (two spatial dimensions, z and ρ, and log-energy y), with grid points spaced evenly along each dimension. We also assume that the pulsar moves along the z-axis, with $z = 0$ defined by its position at time $t = 0$. The size of the region is chosen to be larger than the expected final size of the nebula, as there is no restriction to keep particles within the radius $R_{\rm PWN}$. For typical sizes of young PWNe ($R_{\rm PWN} \sim$ 1–10 pc), the extent of the grid is set to be 2 pc larger.

The time-step Δt is chosen to be smaller than each of the other relevant time-scales: the advection time across a single cell, the diffusion time, the radiative and advective cooling times, and the time for the pulsar to cross a cell. Each of these times will be highest at the termination shock radius except for the diffusion time, with is highest far from the pulsar where the magnetic field strength is lowest.

The solution of the differential equation will also depend on the boundary conditions. Assuming cylindrical symmetry, a reflecting boundary condition is established along the z-axis (e.g. $\partial N/\partial z|_{z=0} = 0$). Following Van Etten and Romani (2011), the other spatial boundary conditions are set as a constant fraction (~ 0.9) of the value in

the nearest edge-cell to enable a low rate of diffusive escape. In energy space, the upper most bin is set to a value greater than the maximum injection energy. Meanwhile, we calculate the lowest possible energy a particle could cool to in the lifetime of the nebula, and set the lowest energy bin below this value. We may therefore establish Dirichlet boundary conditions at these extreme energies, with $N = 0$.

The equation is solved using the alternating-direction implicit (ADI) method of solving multidimensional finite-difference equations (Press et al., 1992). A variable $u(z, \rho, E, t)$ may be discretized on a grid with points at

$$z_i = z_0 + i\Delta z, \tag{6.37}$$

$$\rho_j = \rho_0 + j\Delta\rho, \tag{6.38}$$

$$E_k = E_0 + k\Delta E, \tag{6.39}$$

$$t_n = t_0 + n\Delta t, \tag{6.40}$$

so that $u^n_{ijk} \equiv u(z_i, \rho_j, E_k, t_n)$. The task is then to use the known values at time step n to solve for the values at the next time-step $n + 1$. For an equation of the form

$$\frac{\partial u}{\partial t} = f(u), \tag{6.41}$$

the left-hand side is discretized as

$$\frac{\partial u}{\partial t} \rightarrow \frac{u^{n+1}_{ijk} - u^n_{ijk}}{\Delta t}. \tag{6.42}$$

An explicit differencing scheme will then discretize the right-hand side of Equation 6.41 in terms of u^n_{ijk}, so that the value of u^{n+1}_{ijk} may be solved for algebraically. While simple to calculate, they may not be stable at reasonable large time-steps, especially for equations with higher order differencing, such as the diffusive terms of Equation 6.36. An implicit scheme discretizes the right-hand side of Equation 6.41 in

terms of u_{ijk}^{n+1}, resulting in a set of $i \times j \times k$ coupled equations which must be solved using matrices. While computationally expensive, the solutions are generally stable where explicit methods fail (Press et al., 1992).

The ADI method seeks to decrease the computational expense of the solution in multiple dimensions while maintaining the benefits of implicit differencing. Suppose the operator $f(u)$ is split into sub-operators $f_a(u) + f_b(u)$ for dimensions a and b respectively, which may each be discretized into terms $F_a(u)+F_b(u)$. The ADI scheme treats each part of the solution implicitly in term, splitting the time-step between them.

$$\frac{u_{ijk}^{n+0.5} - u_{ijk}^{n}}{\Delta t/2} = F_a(u_{ijk}^{n+0.5}) + F_b(u_{ijk}^{n}), \tag{6.43}$$

$$\frac{u_{ijk}^{n+1} - u_{ijk}^{n+0.5}}{\Delta t/2} = F_a(u_{ijk}^{n+0.5}) + F_b(u_{ijk}^{n+1}). \tag{6.44}$$

The advantage is that when the differences in a and b are taken so that they only involve a grid points and its two nearest neighbors in the respective dimension, the implicit part of each step may be expressed as a tridiagonal matrix, which may be solved in $\mathcal{O}(N)$ operations rather than the $\mathcal{O}(N^2)$ of a general matrix inversion (Press et al., 1992).

As the terms in z and ρ have the highest order of differences Equation 6.36, the implicit method is alternated between them. The differences in energy are all of first order, and are always treated explicitly (as noted by Press et al. (1992), it is often sufficient to take only the highest order differences implicitly.) The distribution is thus evolved throughout the grid until the current age of the PWN is reached. The values of $G(z, \rho, y)$ may then be converted back into $n(z, \rho, E)$ for the spectral calculations.

Error Analysis and Validation

In transforming a differential equation of a continuous variable into a finite-difference scheme, we are making an approximation to the true solution. Two sources of error will be introduced during the solving procedure:

- Round-off error – error due to the finite precision of memory storage,
- Truncation error – the inherit difference between the finite-difference approximation and the "true" solution, assuming no round-off error.

If the errors from an initial time-step increase at later time-steps, the differencing scheme is *unstable* and the solution is unreliable. If instead the errors decay away during future time-steps, the solution is *stable*. The requirement of stability may thus place demands on the structure of the differencing scheme and the size of the grid spacings.

One simple test for the stability of a numerical scheme is von Neumann analysis, wherein the error is decomposed into its Fourier components (see, e.g., Press et al., 1992). Given the Fourier components of the the initial error at grid point j,

$$\epsilon_j^0 = \sum_{s=0}^{n} A_s e^{i(j\Delta x)(s\pi/L)}, \tag{6.45}$$

with L the size of the solution region and Δx the grid spacing, the error at futures steps will be composed of the same components multiplied by an amplification factor ξ:

$$\epsilon_j^k = \sum_{s=0}^{n} A_s \xi^k e^{ij(s\pi/n)}. \tag{6.46}$$

If $|\xi| < 1$, then the scheme is stable. One can solve for ξ by applying the differencing equation under examination to a single component.

While this form of analysis is strictly only valid for conditions of periodic boundary conditions, with constant (or at least slowly-varying) coefficients in the governing

equation, and may not be fully sufficient to show stability, it has the advantages of being relatively simple compared to other analyses. Unfortunately, applying the analysis to the complete form of Equation 6.36 results in a very complicated expression, which could not be solved for ξ. However, applying it to individual terms of the equation (for example, the diffusion terms) shows individual stability.

A second check on the accuracy of the solution was made by comparing to the Green's function method (Section 6.1.1). The magnetic field to a static, homogeneous value, in accordance with the derivation of the Green's function. The source function was given the form of a point-source moving with a ballistic velocity V:

$$Q(E,\vec{r},t) = \begin{cases} Q_0(t)E^{-\alpha}\delta(\vec{r}-Vt)H(t) & \text{for } \mathrm{E}_{\min} \leq \mathrm{E} \leq \mathrm{E}_{\max}, \\ 0 & \text{otherwise,} \end{cases} \tag{6.47}$$

where, $H(t)$ is the Heaviside step function, and the normalization Q_0 is allowed to vary with time. The numeric integration of the Green's function was performed using the structures of the GNU Scientific Library (Galassi et al., 2009). The results of the multizone method were found to agree with the analytic calculation to within a few percent.

A final investigation into the accuracy of the solution was made by increasing the resolution of the simulation. Taking the finite differences with finer resolution means a closer approximation to the original differential equation, and should give a more accurate result. By halving the bin size in each dimension (z, ρ, and E), and adjusting the time-step accordingly, no significant change was observed in the final results. As this adjustment by itself requires, at minimum, approximately an order of magnitude increase in computing time, further increases in resolution were deemed prohibitive.

6.2.6 Reference frame transformation

The magnetic field strength, B, and bulk wind velocity, $\vec{u}$, have been taken as spherically symmetric about the pulsar. However, we allow that the pulsar may have a substantial kick velocity with respect to the frame of the ISM, which is the frame in which our finite differencing grid is established. Here we discuss the effect of transforming between the pulsar's inertial frame (F') and the ISM-frame (F), which we shall take as the lab frame of the observer. Quantities measured in the pulsar frame will be denoted with a prime symbol.

We let the pulsar velocity vector define the common z-axis of the two frames. The pulsar moves with velocity $V\hat{z}$ in the ISM-frame, with the origins of the two frames aligned at time $t = 0$. Assuming symmetry around the z-axis, which holds in both frames, we can divide the bulk wind velocity in the pulsar frame into the components parallel to the z-axis, u'_z, and perpendicular to the z-axis, u'_ρ. The relativistic addition of velocities (see, e.g., Jackson, 1998) gives the components in the lab frame as

$$u_z = \frac{u'_z + V}{1 + \frac{Vu' \cos\theta'}{c^2}}, \tag{6.48}$$

$$u_\rho = \frac{u'_\rho}{\Gamma\left(1 + \frac{Vu' \cos\theta'}{c^2}\right)}, \tag{6.49}$$

where $\Gamma = (1 - V^2/c^2)^{-1/2}$ and θ' is the angle between $\vec{u}'$ and the z-axis in the pulsar frame.

This results can be compared to the Galilean transformations, $u_z = u'_z + V$ and $u_\rho = u'_\rho$, which are much simpler to calculate. For an large pulsar kick velocity of $V = 1200$ km/s ($\Gamma = 1 + 8.0 \times 10^{-6}$), using the Galilean transformations results in a error of $< 0.14\%$ in the values of u'_z and u'_ρ, even at the maximum value of the bulk velocity ($c/3$). For a more reasonable pulsar speed of $V = 500$ km/s ($\Gamma = 1 + 1.4 \times 10^{-6}$), using the Galilean transformations results in a error of $< 0.06\%$. Therefore we can safely use the Galilean transformations to calculate the components of the bulk wind

velocity in the frame of the ISM.

6.2.7 Spectral calculation and line-of-sight integral

Once the final state of the particle distribution within the nebula has ben calculated, the spectrum at the observer may be calculated. The differential spectral flux F_ν (in erg cm^{-2} s^{-1} Hz^{-1}) at the observer from a given area of the sky $\Delta\Omega$ around a given direction at frequency ν is given by

$$F_\nu(\nu) = \int_{\Delta\Omega} d\Omega \int_\infty^0 ds\ j_\nu(\nu) \tag{6.50}$$

where j_ν is the emissivity in units of erg cm^{-3} s^{-1} Hz^{-1} sr^{-1} and we have ignored absorption. For simplicity, we assume that the solid angle of given pointing is small enough that we can approximate the value of j_ν over the small interval of solid angle $\Delta\Omega$ by the value along the line-of-sight. This allows us to replace the integral over $d\Omega$ with the simple multiplication by the differential $\Delta\Omega$. Although the integral should begin at $s = \infty$, we treat anything outside our PWN as having zero emission (ignore any background or foreground objects). Therefore, the integral is started at an initial distance s_0 beyond the region of the simulation and the numerical integration is performed with a step-size Δs which is smaller than the grid spacing of the simulation.

At each point in the integral, the position is calculated in the PWN frame. If the location is within the simulation region, the electron density at each energy is interpolated on the ρ-z grid, along with the magnetic field strength at that point. The synchrotron emissivity is calculated for each electron energy for a range of photon frequencies, ranging from radio to X-rays, following the description of Longair (1994). For a grid point with electron density $n(E)$, the synchrotron emissivity is given by

$$j_\nu(\nu) = N(E)\ dE \times \left\langle \frac{\sqrt{3}e^3 B \sin\alpha}{8mc^2} F\left(\frac{\nu}{\nu_c}\right) \right\rangle, \tag{6.51}$$

where ν_c is the critical synchrotron frequency (see Equation 1.1), $F(x) = x \int_x^\infty K_{5/3}(z)dz$ (tabulated by Ginzburg and Syrovatskii (1964)), $K_{5/3}$ is the modified Bessel function of order $\frac{5}{3}$, and the angled brackets denote the average over the pitch angle α. The inverse Compton emissivity is calculated by the method of Blumenthal and Gould (1970), which accounts for the full Klein-Nishina cross-section. Assuming an electron density $N(E)$, a seed photon density $n_s(\epsilon)$ for photon energy ϵ, and using the unitless variables $x \equiv h\nu/E$, $\Gamma \equiv 4\epsilon E/(mc^2)^2$, and $q \equiv x/\Gamma(1-x)$, then the IC emissivity is given by

$$j_\nu(\nu) = N(E)\ dE \frac{3\sigma_T m^2 c^5 h^2 \nu}{16\pi E^2} \int d\epsilon \frac{n_s(\epsilon)}{\epsilon} F(q), \tag{6.52}$$

where

$$F(q) = 2q \ln q + (1+2q)(1-q) + \frac{\Gamma^2 q^2 (1-q)}{2(1+\Gamma q)}. \tag{6.53}$$

The cumulative emissivities are then multiplied by Δs and added to arrays which store the result of the integration for each radiative process and the pathlength increased, continuing until s is no longer within the simulation region.

The integral is repeated for each pointing along a grid in sky coordinates. A Cartesean coordinate system is first constructed at the position of the observer (the "observer system", with axis denoted by X, Y, and Z). The current position of the pulsar is a distance d from the observer, with the Z-axis defined by the line from the observer to the pulsar. The pulsar's motion may form an angle ψ with this axis. As a typical PWN system will have dimensions on the order of a few parsecs and typical distances to these systems are on the order of kiloparsecs, we can assume that d is much greater than the dimensions of the simulated region. The X-axis is constructed so the pulsar's velocity vector lies within the X-Z plane (for $\psi \neq 0$) and may be projected along $+\hat{X}$. The Y-axis may then be chosen to make a right-handed system. See Figure 6.4 for an illustration of the assumed geometry of the system.

The grid is then constructed in angular coordinates Θ_X and Θ_Y, where Θ_X is the

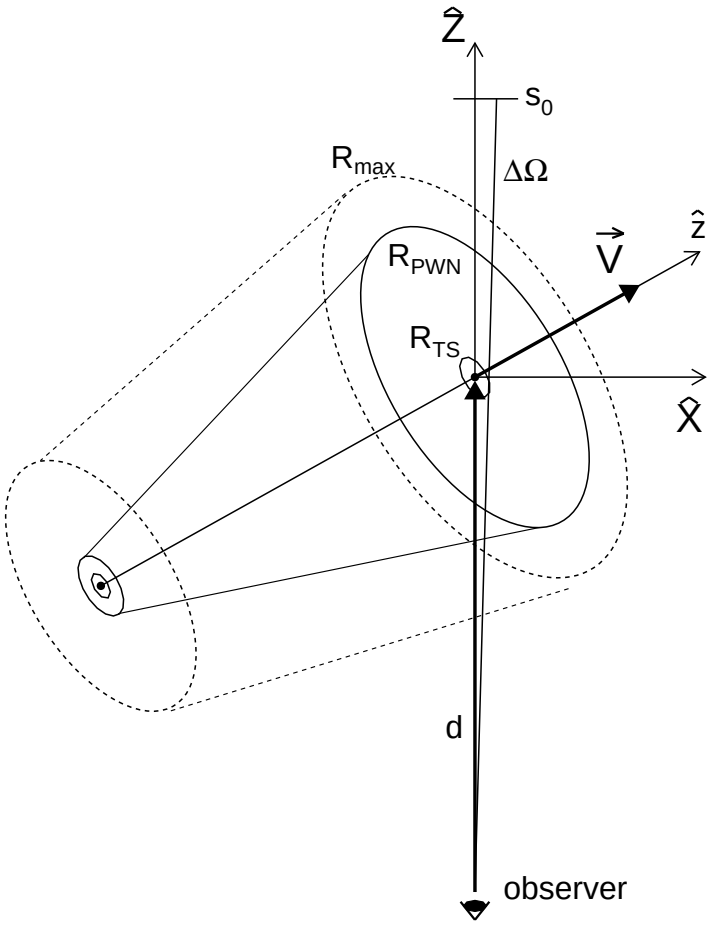

Figure 6.4: Geometry of the PWN system and line-of-sight integration scheme. The line between the observer and the current position of the pulsar established the Cartesean frame of the integration. The velocity $\vec{V}$ of the pulsar establishes the cylindrical geometry of the PWN region.

angle between the line-of-sight path and the Y-Z plane and Θ_Y is the angle between the line-of-sight path and the X-Z plane. For grid spacings $\Delta\Theta_X$ and $\Delta\Theta_Y$, the solid angle around a single grid point is

$$\Delta\Omega = 4 \arcsin\left[\sin\left(\frac{\Delta\Theta_X}{2}\right)\sin\left(\frac{\Delta\Theta_Y}{2}\right)\right] \tag{6.54}$$

$$\approx \Delta\Theta_X \ \Delta\Theta_Y \tag{6.55}$$

where the final approximation holds for small grid spacings.

6.2.8 Assumptions

As a summary, we list here some of the key assumptions of the model. Future refinements to the model may adapt or replace any of these:

- A key assumption of the model is in ignoring the effects of the surrounding SNR, other than using Equation 3.28 to define the size of the PWN, which was derived using hydrodynamic models of the PWN/SNR interaction. One consequence of this assumption is that the pulsar system must be fairly young ($\lesssim 10^4$ yr) so that the SNR reverse shock has not yet reached the system.

- As described above, the bulk wind velocity is radially outward from the pulsar (in the pulsar's frame of reference), and both the wind speed and the magnetic field strength falling off as power-laws, with the power-law indices tied together to reduce the number of free parameters. The exact values are tied to other properties of the PWN. The diffusion constant of the particles within the magnetic field is assumed to follow Bohm scaling. The particles may be transported past the outer radius $R_{\rm PWN}$ so that they escape ahead of or behind the moving pulsar. We thus ignore the shock that would form at $R_{\rm PWN}$ (see Figure 6.1), and treat $R_{\rm PWN}$ merely as a point of reference in establishing the parameters of the nebula. In this spirit, the magnetic field, adiabatic losses, and advective transport terms are all calculated the same for $r > R_{\rm PWN}$ as for $r < R_{\rm PWN}$.

- The injection of new particles and magnetic field energy is tied to the spin evolution of the pulsar, with the current values fixed by *Fermi*-LAT measurements, so that the only open parameters are the true age of the system and the braking index.

Chapter 7

Application of the Simple Cylindrical Model to CTA 1

Here I describe the application of the cylindrical PWN model, described in Chapter 6, to the *VERITAS* observations of CTA 1. A preliminary investigation of the limited parameter space (guided by the observed properties of the pulsar and non-thermal PWN emission) is performed to see if the predicted morphology and spectrum match the measured values.

7.1 Inputs

In applying the model to the data, a number of parameters were held constant at nominal values supported by prior data, while other unknown parameters were varied in an attempt to match the observations. Table 7.1 lists the input parameters that were held constant across all trials. The current spin parameters of the pulsar PSR J0007+7303 are constrained to the values as measure by the *Fermi*-LAT (Abdo et al., 2012). These include the period P and its time-derivative $\dot{P}$, along with the corresponding values of the characteristic time τ_C and spin-down power $\dot{E}$. The pulsar braking index is fixed at $k = 3$, which restricts the true age of the pulsar $T < \tau_C$.

Parameter	Value
	Pulsar:
Spin period, P	0.31587319 s (Abdo et al., 2012)
Period derivative, $\dot{P}$	3.604×10^{-13} s s^{-1} (Abdo et al., 2012)
Braking index, n	3.0
Current spin-down, $\dot{E}$	3.6×10^{37} erg s^{-1}
Characteristic age, τ_C	1.39×10^4 yr
Distance, d	1.4 kpc (Pineault et al., 1997)
	Particle injection:
E_{min}	10^9 eV
E_{max}	10^{14} eV
Termination shock radius, R_{TS}	0.01 pc

Table 7.1: Input parameters for the cylindrical model for CTA 1, held constant across all simulations.

The position of the pulsar wind termination shock is fixed at 0.01 pc which is much smaller than the size of the grid spacing in the spatial dimensions. This value is supported by X-ray observations of the region around PSR J0007+7303 by *Chandra*, which show faint nebulous emission at less than $3''$ from the pulsar, after accounting for PSF (Halpern et al., 2004). This corresponds to 0.02 pc at a distance of 1.4 kpc. If this emission comes from the wind just outside the termination shock, that setting $R_{TS} = 0.01$ pc seems reasonable. The pulsar speed is estimated by scaling the estimate from Slane et al. (2004), made by assuming the pulsar originated at the center of the SNR shell, to the appropriate age.

Table 7.2 lists the remaining free parameters of the model and the various trial values. In the interest of time, each parameter was restricted to a few possible values. Thus, while the final fit may not be the ideal result, it should be a useful initial investigation of the parameter space.

As mentioned above, the true age of the system is restricted to to be less than the characteristic age $\tau_C = 13.9$ kyr. Three possible choices of 8, 10, and 13 kyr were chosen to span a significant range of ages. The current size of the remnant R_{pwn} was

Parameter	Values
True age, T	8, 10, 13 kyr
Final PWN size, $R_{\rm PWN}$	7, 9 pc
Particle index, α	2.0, 2.5, 3.0
Magnetic energy fraction, η_B	0.001, 0.01, 0.1

Table 7.2: Free parameters and the trial values for the cylindrical modeling of CTA 1.

taken from observation. A size of 7 pc results in an angular size of 0°.29 for a distance of 1.4 kpc, which is comparable to the $0°.30 \times 0°.24$ extension measured by *VERITAS*, although a larger size of 9 pc (0°.37 at 1.4 kpc) was also sampled.

Unlike the age and extension of the PWN, the parameters governing the injection of particles and magnetic field at the termination shock are not as directly constrained by observation. As illustrated by Figure 6.2, the spectral index α of the wind at the shock is highly variable and dependent on a number of factors. Therefore, three values were selected to cover a reasonable range of indices for highly relativistic winds with abundant scattering. This range also incorporates the fitted high-energy spectral index of the one-zone model used in Chapter 4. The fraction of injected energy-flux going into magnetic fields ($\eta_B = \dot{E}_B/\dot{E}$) varies over two orders of magnitude, although the wind is always particle dominated ($\eta_B = 0.001 - 0.1$). We emphasize that this analysis is not performed with the goal of finding a unique "best-fit" solution, but to explore the parameter space given a reasonable framework for understanding the non-thermal emission from CTA 1.

7.2 Analysis

After simulating the evolution of the particle population within the nebula and performing the line-of-sight integral over the synchrotron and IC emissivities, two files are produced containing the differential energy flux F_ν at each point in the sky around the pulsar, from radio to TeV energies. This differential energy flux may be converted

into a differential photon flux $\frac{dN}{dE}$, where $\frac{dN}{dE}dE$ is the number of incident photons per unit area per unit time between photon energies E and $E + dE$. It can be shown that $\nu F_\nu = E^2 \frac{dN}{dE}$, which is the energy flux per logarithmic energy band.

The simulation results may now be compared to the observed data. First, a map is constructed of the total number of incident photons from each sky position in the source region for energies in the range 1 TeV–30 TeV, corresponding to the results of the hard-cut *VERITAS* analysis. This number is simply the total of $\frac{dN}{dE}dE = F_\nu \, d\nu/h\nu$ for each energy within the specified range, multiplied by the observation time (41.2 hours) and effective area. The effective area is taken from the same file used in the *VERITAS* data analysis chain, selected for a zenith angle and noise level representative of the actual observation conditions. This map is then convolved with an energy-dependent single-Gaussian PSF, where the appropriate width of the Gaussian is taken from Table 5.2.

The PSF-convolved map is fitted with an asymmetric 2-dimensional Gaussian. The fitted Gaussian accounts for the PSF of the entire energy range as a whole (i.e., not accounting for the energy dependence of the PSF, as in Chapter 5). The spectrum is calculated by adding the fluxes from all bins within a radius $\theta = 0°.23$ of the centroid position of the fitted Gaussian. Separate PSF-convolved maps are also produced for the relevant energy bands $E < 3$ TeV and $E > 3$ TeV.

7.3 Results

The parameters of the best-fit scenario are given in Table 7.3. Similar to the results of the GSZ model (see Table 4.2), the model favors an old PWN ($T \approx 0.9\tau_c$) with low magnetization. The hardest spectrum is favored for the injected particles.

The PSF-convolved emission map of the PWN is shown in Figure 7.1. The corresponding maps for energies above and below 3 TeV are shown in Figure 7.2. The one

Parameter	Value
Free Parameters:	
True age, T	13 kyr
Final PWN size, $R_{\rm PWN}$	7 pc
Particle index, α	2.0
Magnetic energy fraction, η_B	0.01
Derived Parameters:	
Spin-down time τ_0	887 yr
Adiabatic wind index, a	0.77
Magnetic field index, b	0.23
Nebular expansion speed, $\dot{R}_{\rm PWN}$	630 km s^{-1}
Pulsar kick velocity	450 km s^{-1}

Table 7.3: Best fit parameters for the cylindrical modeling of CTA 1, taken from the possible values listed in Table 7.2. For a description of the derived parameters, see Chapter 6.

standard-deviation extent of a 2-dimensional Gaussian fitted to each map is shown by a red ellipse, with the fitted values of the parameters given in Table 7.4. The extent from the fitted *VERITAS* data is also shown on each map by a black ellipse, where the centroid has been set equal to that of the simulated data. While the model does predict an asymmetric profile, with a tail of emission extending behind the pulsar, the model underestimates the extent of emission when combining data across all energies. In one case (the > 3 TeV map), the extent of the emission region predicted by the model matches the measured width. The centroid of the high-energy (> 3 TeV) emission is nearer to the pulsar than the low-energy (< 3 TeV) emission, although the errors on the two positions are large compared to the difference between them.

The spectrum extracted from around the fitted centroid is shown in Figure 7.3. While the relative normalization between the synchrotron and IC peaks is approximately correct, the overall normalization is about one order of magnitude too low.

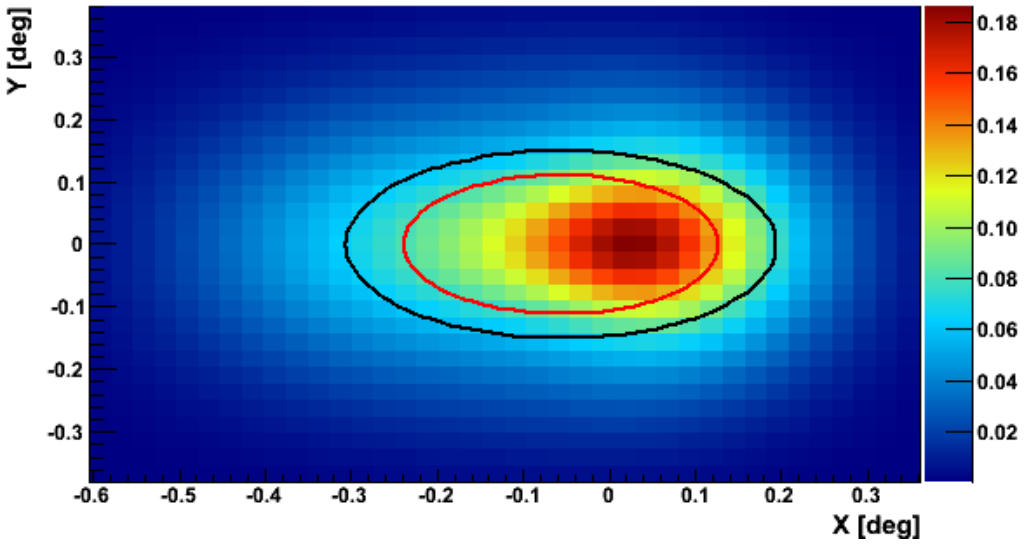

Figure 7.1: PSF-convolved map of the expected emission from the best-fit model. The red ellipse marks the 2-dimensional Gaussian fitted to the map. The black ellipse marks the fitted extension from the *VERITAS* data. The pulsar is located at the origin. The color-scale is in expected counts within a bin.

Parameter	Energy range		
	all	$1-3$ TeV	$3-30$ TeV
centroid offset	0.056 ± 0.073	0.059 ± 0.078	0.033 ± 0.070
major axis	0.18 ± 0.05	0.19 ± 0.06	0.14 ± 0.05
minor axis	0.11 ± 0.03	0.11 ± 0.03	0.10 ± 0.03

Table 7.4: Result of fitting a 2-dimensional, asymmetric Gaussian to the PSF-convolved map of emission above 1 TeV for the best-fit model. All parameters are given in degrees.

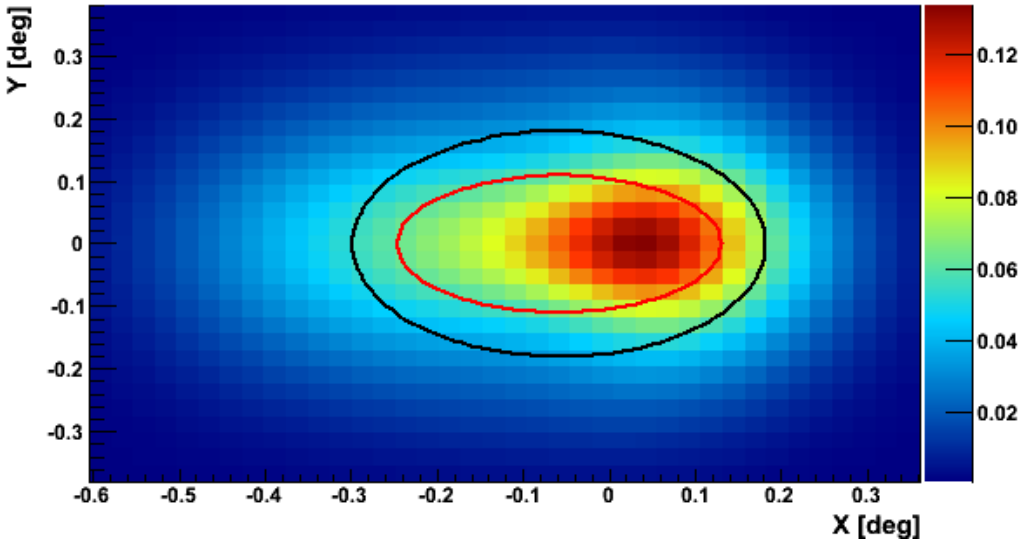

(a) Energies $1 - 3$ TeV

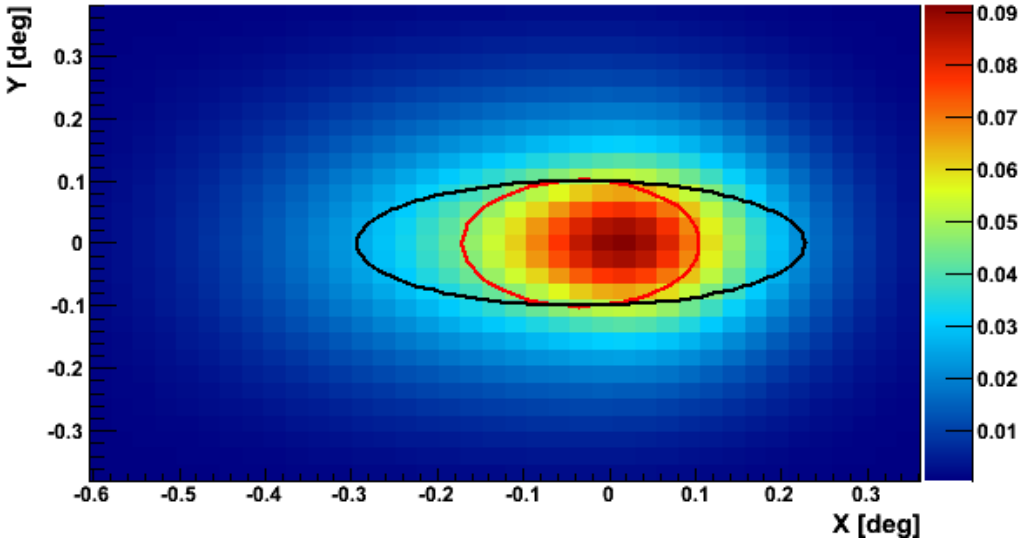

(b) Energies $3 - 30$ TeV

Figure 7.2: PSF-convolved maps of the expected emission from the best-fit model for energies above and below 3 TeV. The red ellipses mark the 2-dimensional Gaussian fitted to each map. The black ellipses mark the fitted extension from the *VERITAS* data for the respective energy bands. The pulsar is located at the origin. The color-scale is in expected counts within a bin.

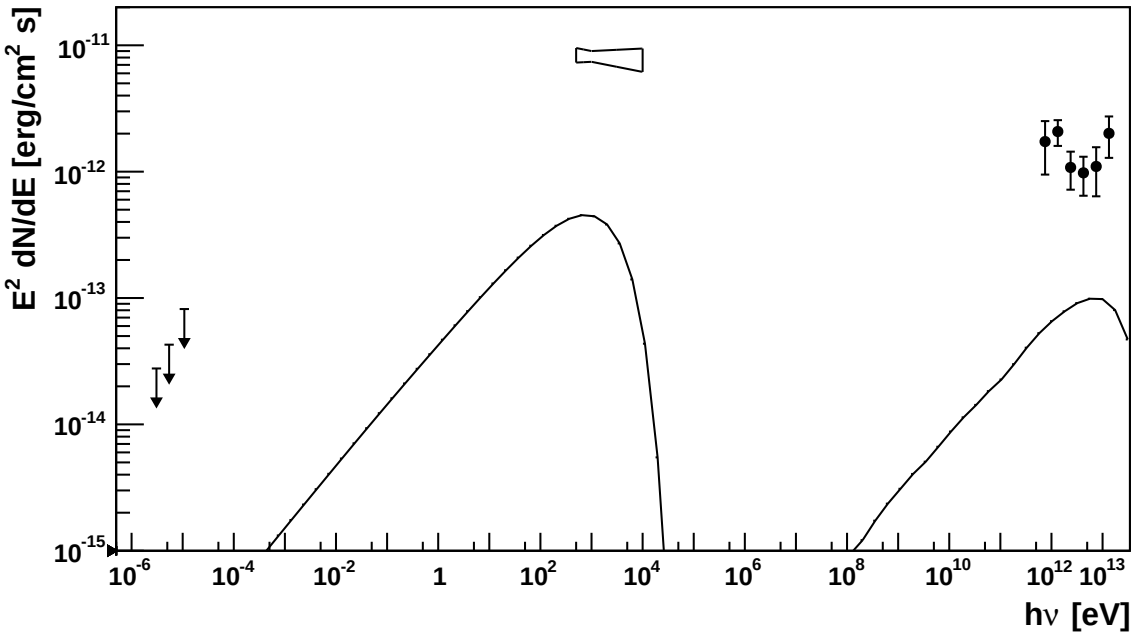

Figure 7.3: Multiwavelength spectrum of the best-fit model, including synchrotron emission and inverse Compton scattering of the CMB. The TeV data points and radio upper limits are described in Chapter 4. X-ray data is from Slane et al. (1997).

7.4 Interpretation

Using nominal values for many parameters, and considering only a few free parameters with constrained values, we recover reasonable agreement in morphology and spectral shape. However, even in the best fit scenario, both the synchrotron and inverse Compton emission of the model fall approximately an order of magnitude below the observational data, and the predicted spatial extent of the emission is too small. Rather than taking a nonphysical approach of simply increasing the number of free parameters and running a multiparameter fitting program, we instead look to physical mechanisms that could account for these discrepancies. Invoking Occam's Razor, preference is given to mechanisms that can both increase the overall luminosity of the nebula at all wavelengths while transporting the emitting particles farther from the pulsar.

7.4.1 Increasing the emission

The inverse Compton peak could be enhanced by scattering of other ambient photon fields. As a test, an isotropic far-infrared (FIR) field was included in the IC line-of-sight integral, using the same electron population as the best-fit model above (i.e. no additional cooling effects were included due to the additional scattering). The FIR field is parameterized with a temperature of 70 K and an energy density of 0.2 eV cm^{-3}, values typical for a Galactic disk environment (Hinton and Aharonian, 2007). The Klein-Nishina cutoff for electrons scattering such a spectrum begins at a particle energy of only $\sim$4 TeV. As shown in Figure 7.4, the IC peak from the this component is an order of magnitude lower then for the CMB component, so our assumption of using only scattering of the CMB to represent the IC process remains valid. While larger energy density of seed photons could boost the IC emission to the level of the data, this would be an ad hoc assumption, adding another free parameter to the model without observational evidence to constrain it, and would still not fix the deficit of synchrotron emission.

A simple method of increasing the synchrotron peak is to increase the magnetic field, as the power per unit frequency emitted by a power-law spectrum of particles $N(E) \sim E^{-p}$ is proportional to $B^{(p+1)/2}$ (Rybicki and Lightman, 1979). However, if the synchrotron (X-ray) emission and IC (TeV) emission are assumed to originate from the same population of particles, then the ratio of the integral fluxes is tied to the magnetic field strength (Govoni and Feretti, 2004). As the ratio of these two peaks is already similar to that seen in the data, changing only the magnetic field strength (by changing the parameter η_B) is insufficient. In addition, increasing the particle emissivities, and thus the radiative cooling rates, without changing the underlying particle spectrum, would lead to fewer TeV-emitting particles at large distances from the pulsar. This would decrease the extent of the TeV nebula, which is already smaller than the observed morphology.

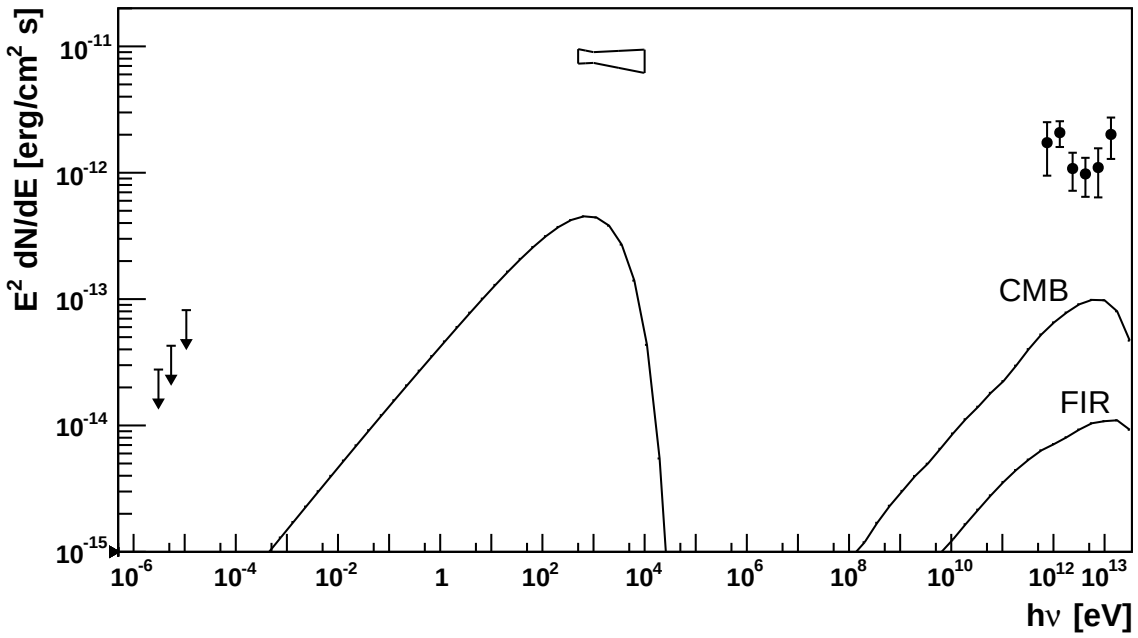

Figure 7.4: Multiwavelength spectrum of the best-fit model, including inverse Compton scattering of the CMB and a FIR field typical of the Galactic disc environment (see text for description). The two IC modes are plotted seperately, as labeled. Data points are the same as Figure 7.3.

One way to solve the synchrotron and IC deficits simultaneously would be to increase the population of electrons emitting at these energies. However, we can not simply scale up the number of injected particles, as their injected power is already 99% of the pulsar spin-down luminosity. Similarly, the hardness of the injected spectrum (and thus the fraction of injection energy going into the highest-energy particles) is already near the reasonable limits of a relativistic shock while maintaining efficient scattering.

7.4.2 Particle transport and cooling

Another modification one might consider to the model is a decrease in the particle cooling rate, which would have the effects of increasing the survival time of high-energy (X-ray- and TeV-emitting) electrons, transporting them farther out into the nebula. This would simultaneously increase the radiative luminosity and the extent of the PWN as seen in X-rays and TeV gamma rays.

Given the radial profile of the advective wind speed, $u(r) = u_0(r/r_0)^{-a}$, and the formulas for the radiative lifetimes of an electron (Equations 1.9 and 1.10), one can calculate how far the highest-energy particles will be carried within their cooling time. For a lifetime τ, a particle will travel a distance r as given by

$$\tau = \int_{R_{\rm TS}}^{r} \frac{dr'}{u(r')} \tag{7.1}$$

$$= \frac{3}{c} \int_{R_{\rm TS}}^{r} dr' \left(\frac{r'}{R_{\rm TS}} \right)^{a} . \tag{7.2}$$

Solving for r (assuming $a \neq -1$),

$$r(\tau) = R_{\rm TS} \left[1 + \frac{(a+1)c\tau}{3R_{\rm TS}} \right]^{1/(a+1)} . \tag{7.3}$$

For the following discussion I'll assume particle energies of 100 TeV, the upper limit of

the injected spectrum, as these particles will radiate with the characteristic energies needed to explain the highest X-ray and TeV emission, as given by Equations 1.7 and 1.8.

The shortest lifetime occurs at the termination shock where the magnetic field is largest, so that we may use that value to derive a lower limit on the advection distance. Given the parameters of the best-fit model, the magnetic field strength at the termination shock is 275 μG early in the pulsar's lifetime (at times much less than the spin-down time) and 18 μG at the current time. These result in synchrotron lifetimes of 1.7 yr and 390 yr, respectively, with advection distances of 0.07 pc and 1.5 pc. These are obviously much smaller than the final extent of the remnant.

At its smallest, the magnetic field strength is $\sim$ 4 μG (a distance of 7 pc from the pulsar). This results in a synchrotron lifetime of 7.8 kyr. However, IC losses are no longer negligible at such low field strengths. Following Aharonian et al. (2006c) and including a factor of 2/3 in the IC loss-rate to account for the Klein-Nishina suppression, the total cooling time is

$$\tau_{tot} = \frac{E}{\dot{E}_{sync} + \dot{E}_{IC}} \tag{7.4}$$

$$\approx 17.9 \left(\frac{100 \text{ TeV}}{E}\right) \left[1 + 14.3 \left(\frac{B}{10 \ \mu\text{G}}\right)^2\right]^{-1} \text{ kyr}, \tag{7.5}$$

or 5440 yr for a 100 TeV particle in a field of 4 μG. This results in an advective distance of 6.5 pc, which is comparable with the size of the PWN.

It should be noted that adiabatic losses will further decrease this distance if the respective timescale is comparable with the radiative cooling time. While the adiabatic losses also decrease with time, so that the cooling time $\tau_{ad} = 5t/6$, the radiative losses will only dominate for high energy particles in strong magnetic fields (>10 μG).

Of course, the true expression for the distance traversable by the particles is more difficult to calculate, as they sample a varying magnetic field strength as they are

advected outward. However it should lie somewhere between the two extreme cases described above. At best, the 100 TeV particles which radiate the highest energy X-rays and gamma-rays should only fill a fraction of the PWN volume. This stands in contrast to the GSZ one-zone model, which by its construction requires that the particle spectrum be the same through the nebula.

Our model also includes diffusive transport which depends on the spectrum of turbulence in the magnetic field, and the efficiency of pitch-angle and cross-field scattering. If the diffusion speed is sufficiently fast, the particles could be carried into to outer nebula before they cool on the higher magnetic fields near the termination shock. For a Bohm scaling of the diffusion constant $D = cE/3eB$, the diffusion time τ_{diff} to travel a distance r is

$$\tau_{diff} = 905 \left(\frac{r}{1 \text{ pc}}\right)^2 \left(\frac{100 \text{ TeV}}{E}\right) \left(\frac{B}{10 \ \mu\text{G}}\right) \text{ yr.} \tag{7.6}$$

Therefore, with the current model, diffusion may be important at the farthest distances (i.e. at the lowest magnetic field strengths), but only if the high-energy particles survive to those distances via advection. An alternative scaling for the diffusion constant may make diffusive transport more efficient by decreasing the rate of scattering and therefore increasing the mean free path. This would require the introduction of further free parameters; a greater understanding of the spectrum of turbulence within the nebula would be useful for constraining these values. Alternatively, altering the magnetic field profile to a steeper fall-off would provide faster transport and less cooling, but with similar problems as before. Again, a more detailed mapping of the magnetic field structure through high-resolution imaging of the synchrotron emission could thus provide valuable constraints on the model.

Aside from transporting the particles to outer nebula more quickly, a decrease in the adiabatic cooling rate would also allow for a larger population of high-energy particles while leaving the radiative cooling rates (and thus the ratio of the spectral

luminosities) unaffected. Interaction with the SNR reverse shock, as accounted for in the GSZ model, would slow the expansion of the PWN, decreasing adiabatic losses. Furthermore, as the reverse shock continues to propagate inward, it compresses the nebula, so that the particles would experience adiabatic acceleration, which could increase the energetic particle population. However, these gains could in turn be offset by the associated increase in the magnetic field strength, which burn off the high-energy particles through enhanced synchrotron emission (Gaensler and Slane, 2006). This burn-off can serve to increase the synchrotron luminosity but decrease the TeV luminosity. Therefore, accounting for the SNR-PWN interaction could provide some benefit to the model, but only if the SNR reverse shock does not compress the PWN too much.

Finally, it is possible that the model is too simple and neglects important physical processes within the system. There may be some additional source of power not yet accounted for, such as reacceleration near the PWN forward shock, or interaction with the SNR reverse shock. Such shocks could reenergized the cooling particles, leading to more high-energy emission. The SNR reverse shock in particular could introduce energy originally associated with the kinetic energy of the SNR explosion and subsequent ejecta, so that the pulsar spin-down no longer constrains the overall energetics. Alternatively, the wind could contain a non-negliable hadronic component, which would suffer vastly lower synchrotron and IC losses and contribute to the gamma-ray emissivity through pion decay. The lower radiative-cooling rate means that the hadronic particles could survive longer than the corresponding electrons, reaching larger distances from the pulsar. Therefore the failure of a purely leptonic model to fit the data could point to new understanding of the pulsar wind system.

7.5 Summary

The simple cylindrical model was applied to the PWN within the SNR CTA 1. The inputs to the model combined the *Fermi* measurements of the pulsar spin parameters and the *VERITAS* measurements of the PWN size. A limited search of the parameter-space revealed a best-fit scenario of an old remnant with a hard particle spectrum and low magnetization. The model was unable to match the observed multiwavelength spectrum and TeV morphology, although it did predict an asymmetric shape and the proper ratio of synchrotron to inverse Compton luminosity. While the luminosities could be enhanced by increasing the energy density of the magnetic field and adding additional seed ambient photon fields, reducing the cooling of the particles and/or increasing their rate of transport into the outer nebula may correct both the spectral and morphological issues.

Chapter 8

Conclusions

For over a decade, observations of TeV gamma rays have enabled investigations of extreme astrophysical environments, both Galactic and extragalactic. These observations make use of the atmospheric Cherenkov imaging technique, using arrays of large mirrors, sensitive photodetector cameras, and high-speed electronics to record the faint Cherenkov flashes from particle showers initiated by gamma-rays in the upper atmosphere. By using an array of telescopes, modern instruments such as *VERITAS* can perform stereoscopic reconstruction of these showers to increase their sensitivity. Over 100 sources TeV have thus been detected.

Of the identified Galactic TeV sources, the largest number (> 30) are pulsar wind nebulae (PWNe). Pulsars lose rotational energy to an ultrarelativistic, magnetized wind of electron-positron pairs. The confinement of this wind by the ambient pressure of the surrounding medium produce a relativistic wind termination shock in which the particles are accelerated and have their pitch angles randomized. The particles then radiate via synchrotron and inverse Compton processes as they expand outward to form the nebula. Interactions with the surrounding SNR or ISM, combined with the pulsar kick velocity and spin-down, result in a range of PWN morphologies in a complicated evolutionary progression. PWNe therefore offer excellent opportunity to study relativistic particle acceleration, pulsar evolution, and wind-SNR interactions.

One of the most recently detected TeV sources is the PWN inside the SNR CTA 1. Guided by the discovery of the pulsar PSR J0007+7303 by the *Fermi*-LAT instrument, along with theoretical modeling of the unpulsed PWN emission, *VERITAS* observed CTA 1 for $\sim$ 41 hours in between September 2010 and December 2011. Analysis revealed an extended source of gamma-rays at a 6.5 standard deviation post-trials significance, with a centroid $5'$ from the pulsar and no significant variation in morphology with respect to energy. The TeV spectrum is hard, with a differential spectral index of $\Gamma = 2.2$, and the integral power is 0.2% of the pulsar's spin-down power. The energetics and size of the TeV emission, along with multiwavelength imaging of the system, argue for the identification of the source as the PWN of PSR J0007+7303, which is visible in archival X-ray data. Modeling of the SNR-PWN system with a one-zone evolutionary model suggests an average magnetic field of 6 μG, along with recent interaction between the PWN and the reverse shock of the SNR.

In order to further investigate the structure of PWNe, including energy-dependent morphology and the influence of multiple methods of particle transport and cooling, a multi-zone model is required. One such model is described which uses an assumption of cylindrical symmetry to describe the particle distribution around a moving pulsar and the resulting emission. While neglecting the effects of the surrounding SNR, the model accounts for particle transport by both an advective wind and Bohm diffusion within a magnetic field, as well as cooling by synchrotron, inverse Compton, and adiabatic channels.

As a test, the model is applied to the observations of the CTA 1 PWN. Various input parameters are fixed by the *Fermi* measurements of the pulsar spin parameters and the *VERITAS* measurement of the PWN size. A limited search of the remaining parameter space is performed. Qualitatively, the model correctly predicts an asymmetric, extended morphology, along with the correct ratio between the synchrotron and IC peaks. However, it underestimates both the extent of the nebula and the mag-

nitudes of the radiative fluxes, and it can not explain the shape of the unpulsed GeV emission detected by the *Fermi*-LAT. The fit of the model might be improved by increasing the rate of particle transport into the outer nebula, where radiative losses are lower, or by decreasing the rate of adiabatic cooling throught the entire nebula.

We hope to refine this model and apply it to other PWNe more suited to this analysis. Ultimately, tailed-out PWNe may provide a unique glimpse into the entire spin-down history and energetics of pulsars. These objects may imprint their evolution along the pulsar trajectory, offering information not accessible in young, symmetric nebulae. They may therefore act as some of the best laboratories for studying the properties of astrophysical plasmas, including the nature of particle diffusion in magnetic turbulence, relativistic shock acceleration, and pulsar magnetospheres.

Bibliography

A. A. Abdo, M. Ackermann, W. B. Atwood, et al. The Fermi Gamma-Ray Space Telescope Discovers the Pulsar in the Young Galactic Supernova Remnant CTA 1. *Science*, 322:1218, Nov. 2008.

A. A. Abdo, M. Ackermann, M. Ajello, et al. Fermi Large Area Telescope Observations of PSR J1836+5925. *ApJ*, 712:1209–1218, Apr. 2010.

A. A. Abdo, K. S. Wood, M. E. DeCesar, et al. PSR J0007+7303 in the CTA1 Supernova Remnant: New Gamma-Ray Results from Two Years of Fermi Large Area Telescope Observations. *ApJ*, 744:146, Jan. 2012.

A. Abramowski, F. Acero, F. Aharonian, et al. H.E.S.S. Observations of the Globular Clusters NGC 6388 and M15 and Search for a Dark Matter Signal. *ApJ*, 735:12, July 2011.

V. A. Acciari, M. Beilicke, G. Blaylock, et al. VERITAS Observations of the γ-Ray Binary LS I +61 303. *ApJ*, 679:1427–1432, June 2008.

V. A. Acciari, E. Aliu, T. Arlen, et al. VERITAS Observations of Gamma-Ray Bursts Detected by Swift. *ApJ*, 743:62, Dec. 2011.

F. Aharonian, A. G. Akhperjanian, A. R. Bazer-Bachi, et al. Observations of the Crab nebula with HESS. *A&A*, 457:899–915, Oct. 2006a.

F. Aharonian, A. G. Akhperjanian, A. R. Bazer-Bachi, et al. The H.E.S.S. Survey of the Inner Galaxy in Very High Energy Gamma Rays. *ApJ*, 636:777–797, Jan. 2006b.

F. Aharonian, A. G. Akhperjanian, A. R. Bazer-Bachi, et al. Energy dependent γ-ray morphology in the pulsar wind nebula HESS J1825-137. *A&A*, 460:365–374, Dec. 2006c.

F. A. Aharonian, W. Hofmann, A. K. Konopelko, and H. J. Völk. The potential of ground based arrays of imaging atmospheric Cherenkov telescopes. I. Determination of shower parameters. *Astroparticle Physics*, 6:343–368, Mar. 1997.

F. A. Aharonian, A. G. Akhperjanian, A. R. Bazer-Bachi, et al. A possible association of the new VHE γ-ray source HESS J1825 137 with the pulsar wind nebula G 18.0 0.7. *A&A*, 442:L25–L29, Nov. 2005.

J. Albert, E. Aliu, H. Anderhub, et al. VHE γ-Ray Observation of the Crab Nebula and its Pulsar with the MAGIC Telescope. *ApJ*, 674:1037–1055, Feb. 2008.

J. Aleksić, E. A. Alvarez, L. A. Antonelli, et al. Searches for dark matter annihilation signatures in the Segue 1 satellite galaxy with the MAGIC-I telescope. *J. Cosmology Astropart. Phys.*, 6:35, June 2011.

E. Aliu. *VHE gamma-ray observations of Northern sky pulsar wind nebulae with the MAGIC Telescope*. PhD thesis, Universitat Autónoma de Barcelona, 2007.

R. Aloisio and V. Berezinsky. Diffusive Propagation of Ultra-High-Energy Cosmic Rays and the Propagation Theorem. *ApJ*, 612:900–913, Sept. 2004.

T. Anada, A. Bamba, K. Ebisawa, and T. Dotani. X-Ray Studies of HESS J1809-193 with Suzaku. *PASJ*, 62:179, Feb. 2010.

P. W. Anderson and N. Itoh. Pulsar glitches and restlessness as a hard superfluidity phenomenon. *Nature*, 256:25–27, July 1975.

A. M. Atoyan and F. A. Aharonian. On the mechanisms of gamma radiation in the Crab Nebula. *MNRAS*, 278:525–541, Jan. 1996.

M. G. Baring. Lepton Acceleration in Pulsar Wind Nebulae. In D. F. Torres & N. Rea, editor, *High-Energy Emission from Pulsars and their Systems*, page 453, 2011.

M. Beilicke and the VERITAS Collaboration. The Galactic Center Region Imaged by VERITAS. In A. Morsellia and R. Bellazzini and A. Copone and P. Caraveo and S. Ciprini and S. Cutini and M. Ercoli and D. Gasparrini and L. Latronico and A. Morselli and G. Spandre and V. Vitale, editor, *Proceedings of the 2011 Fermi Symposium*, 2011.

D. Berge, S. Funk, and J. Hinton. Background modelling in very-high-energy γ-ray astronomy. *A&A*, 466:1219–1229, May 2007.

R. D. Blandford, J. P. Ostriker, F. Pacini, and M. J. Rees. Radio Halos around Old Pulsars - Ghost Supernova Remnants. *A&A*, 23:145, Feb. 1973.

J. M. Blondin, R. A. Chevalier, and D. M. Frierson. Pulsar Wind Nebulae in Evolved Supernova Remnants. *ApJ*, 563:806–815, Dec. 2001.

G. R. Blumenthal and R. J. Gould. Bremsstrahlung, Synchrotron Radiation, and Compton Scattering of High-Energy Electrons Traversing Dilute Gases. *Reviews of Modern Physics*, 42:237–271, 1970.

K. T. S. Brazier, O. Reimer, G. Kanbach, and A. Carraminana. A candidate gamma-ray pulsar in the supernova remnant CTA 1. *MNRAS*, 295:819–824, Apr. 1998.

R. Brun and F. Rademakers. ROOT – An object oriented data analysis framework. *Nucl. Inst. & Meth. in Phys. Res. A*, 389:81–86, 1997. See also `http://root.cern.ch/`.

N. Bucciantini, E. Amato, and L. Del Zanna. Relativistic MHD simulations of pulsar bow-shock nebulae. *A&A*, 434:189–199, Apr. 2005.

N. Bucciantini, J. Arons, and E. Amato. Modelling spectral evolution of pulsar wind nebulae inside supernova remnants. *MNRAS*, 410:381–398, Jan. 2011.

P. A. Caraveo, A. De Luca, M. Marelli, et al. X-ray Pulsations from the Radio-quiet Gamma-ray Pulsar in CTA 1. *ApJ*, 725:L6–L10, Dec. 2010.

F. Casse and A. Marcowith. Astroparticle yield and transport from extragalactic jet terminal shocks. *Astroparticle Physics*, 23:31–56, Feb. 2005.

K. S. Cheng, C. Ho, and M. Ruderman. Energetic radiation from rapidly spinning pulsars. I - Outer magnetosphere gaps. II - VELA and Crab. *ApJ*, 300:500–539, Jan. 1986.

P. A. Cherenkov. Visible emission of clean liquids by action of γ radiation. *Doklady Akad. Nauk SSSR*, 2:451, 1934.

P. Cogan. VEGAS, the VERITAS Gamma-ray Analysis Suite. In *International Cosmic Ray Conference*, volume 3 of *International Cosmic Ray Conference*, pages 1385–1388, 2008.

M. K. Daniel. The VERITAS standard data analysis. In *International Cosmic Ray Conference*, International Cosmic Ray Conference, pages 1325–1328, 2008.

O. C. de Jager and A. Djannati-Ataï. Implications of H.E.S.S. observations of pulsar wind nebulae. In W. Becker, editor, *Astrophysics and Space Science Library*, volume 357 of *Astrophysics and Space Science Library*, page 451, 2009.

O. C. de Jager, P. O. Slane, and S. LaMassa. Probing the Radio to X-Ray Connection of the Vela X Pulsar Wind Nebula with Fermi LAT and H.E.S.S. *ApJ*, 689:L125–L128, Dec. 2008.

C. M. Espinoza, A. G. Lyne, B. W. Stappers, and M. Kramer. A study of 315 glitches in the rotation of 102 pulsars. *MNRAS*, 414:1679–1704, June 2011.

J. Fang and L. Zhang. Multiband emission from pulsar wind nebulae: a possible injection spectrum. *A&A*, 515:A20, June 2010.

V. P. Fomin, A. A. Stepanian, R. C. Lamb, et al. New methods of atmospheric Cherenkov imaging for gamma-ray astronomy. I. The false source method. *Astroparticle Physics*, 2:137–150, May 1994.

I. M. Frank and I. E. Tamm. Coherent visible radiation of fast electrons passing through matter. *Doklady Akad. Nauk SSSR*, 14:109, 1937.

B. M. Gaensler and P. O. Slane. The Evolution and Structure of Pulsar Wind Nebulae. *ARA&A*, 44:17–47, Sept. 2006.

M. Galassi, B. Gough, G. Jungman, et al. *GNU Scientific Library Reference Manual*. Network Theory Ltd., third edition, 2009.

J. D. Gelfand, P. O. Slane, and W. Zhang. A Dynamical Model for the Evolution of a Pulsar Wind Nebula Inside a Nonradiative Supernova Remnant. *ApJ*, 703: 2051–2067, Oct. 2009.

P. Ghosh. *Rotation and Accretion Powered Pulsars*. World Scientific Publishing Co, 2007.

V. L. Ginzburg and S. I. Syrovatskii. *The Origin of Cosmic Rays*. Pergamon Press Ltd., 1964.

F. Giordano, M. Naumann-Godo, J. Ballet, et al. Fermi Large Area Telescope Detection of the Young Supernova Remnant Tycho. *ApJ*, 744:L2, Jan. 2012.

T. Gold. Rotating Neutron Stars as the Origin of the Pulsating Radio Sources. *Nature*, 218:731–732, May 1968.

P. Goldreich and W. H. Julian. Pulsar Electrodynamics. *ApJ*, 157:869, Aug. 1969.

F. Govoni and L. Feretti. Magnetic Fields in Clusters of Galaxies. *International Journal of Modern Physics D*, 13:1549–1594, 2004.

T. A. Hall, S. P. Wakely, and VERITAS Collaboration. Observations of Galactic Pulsars and Shell-Type SNRs with the Whipple 10 m Imaging Atmospheric Cherenkov Telescope. In *International Cosmic Ray Conference*, volume 6 of *International Cosmic Ray Conference*, page 2485, Aug. 2001.

J. P. Halpern and S. S. Holt. Discovery of soft X-ray pulsations from the gamma-ray source Geminga. *Nature*, 357:222–224, May 1992.

J. P. Halpern, E. V. Gotthelf, F. Camilo, D. J. Helfand, and S. M. Ransom. X-Ray, Radio, and Optical Observations of the Putative Pulsar in the Supernova Remnant CTA 1. *ApJ*, 612:398–407, Sept. 2004.

J. P. Halpern, F. Camilo, and E. V. Gotthelf. The Next Geminga: Search for Radio and X-Ray Pulsations from the Neutron Star Identified with 3EG J1835+5918. *ApJ*, 668:1154–1157, Oct. 2007.

D. Hanna, A. McCann, M. McCutcheon, and L. Nikkinen. An LED-based flasher system for VERITAS. *Nuclear Instruments and Methods in Physics Research A*, 612:278–287, Jan. 2010.

D. E. Harris and J. A. Roberts. Radio Source Measurements at 960 Mc/s. *PASP*, 72: 237, Aug. 1960.

R. C. Hartman, D. L. Bertsch, S. D. Bloom, et al. The Third EGRET Catalog of High-Energy Gamma-Ray Sources. *ApJS*, 123:79–202, July 1999.

W. Heitler. *Quantum theory of radiation*. Clarendon Press, third edition, 1954.

H.E.S.S. Collaboration, A. Abramowski, F. Acero, et al. Very-high-energy gamma-ray emission from the direction of the Galactic globular cluster Terzan 5. *A&A*, 531: L18, July 2011.

A. M. Hillas. Cerenkov light images of EAS produced by primary gamma. In F. C. Jones, editor, *International Cosmic Ray Conference*, volume 3 of *International Cosmic Ray Conference*, pages 445–448, Aug. 1985.

J. A. Hinton and F. A. Aharonian. Inverse Compton Scenarios for the TeV Gamma-Ray Emission of the Galactic Center. *ApJ*, 657:302–307, Mar. 2007.

J. A. Hinton and W. Hofmann. Teraelectronvolt Astronomy. *ARA&A*, 47:523–565, Sept. 2009.

G. Hobbs, D. R. Lorimer, A. G. Lyne, and M. Kramer. A statistical study of 233 pulsar proper motions. *MNRAS*, 360:974–992, July 2005.

W. Hofmann, I. Jung, A. Konopelko, et al. Comparison of techniques to reconstruct VHE gamma-ray showers from multiple stereoscopic Cherenkov images. *Astroparticle Physics*, 12:135–143, Nov. 1999.

J. Holder, E. Aliu, T. Arlen, et al. VERITAS: Status and Highlights. *ArXiv e-prints*, Nov. 2011.

J. D. Jackson. *Classical Electrodynamics, 3rd Edition*. Wiley, July 1998.

J. V. Jelley. *Čerenkov Radiation and Its Applications*. Pergamon Press, 1958.

J. V. Jelley and N. A. Porter. Čerenkov Radiation from the Night Sky, and its Application to γ-Ray Astronomy. *QJRAS*, 4:275, Sept. 1963.

O. Kargaltsev and G. G. Pavlov. Pulsar Wind Nebulae in the Chandra Era. In C. Bassa, Z. Wang, A. Cumming, & V. M. Kaspi, editor, *40 Years of Pulsars: Millisecond Pulsars, Magnetars and More*, volume 983 of *American Institute of Physics Conference Series*, pages 171–185, Feb. 2008.

O. Kargaltsev and G. G. Pavlov. Pulsar-wind nebulae in X-rays and TeV γ-rays. *X-ray Astronomy 2009; Present Status, Multi-Wavelength Approach and Future Perspectives*, 1248:25–28, July 2010.

C. F. Kennel and F. V. Coroniti. Confinement of the Crab pulsar's wind by its supernova remnant. *ApJ*, 283:694–709, Aug. 1984.

B. Khelifi, A. Barrau, R. Bazer-Bachi, et al. TeV gamma ray observations of Shell-type Supernova remnants by the CAT telescope (1999-2001). In *International Cosmic Ray Conference*, volume 6 of *International Cosmic Ray Conference*, page 2444, Aug. 2001.

N. Komin and for the H. E. S. S. collaboration. Search for Galactic Cosmic Ray Sources with H.E.S.S. In *Proceedings of the 23rd Rencontres de Blois*, 2011.

H. Krawczynski, D. A. Carter-Lewis, C. Duke, et al. Gamma hadron separation methods for the VERITAS array of four imaging atmospheric Cherenkov telescopes. *Astroparticle Physics*, 25:380–390, July 2006.

S. M. LaMassa, P. O. Slane, and O. C. de Jager. Probing the Nature of the Vela X Cocoon. *ApJ*, 689:L121–L124, Dec. 2008.

L. D. Landau and E. M. Lifshitz. *The classical theory of fields*. Pergamon Press, 1975.

T.-P. Li and Y.-Q. Ma. Analysis methods for results in gamma-ray astronomy. *ApJ*, 272:317–324, Sept. 1983.

M. A. Livingstone, V. M. Kaspi, F. P. Gavriil, et al. New phase-coherent measurements of pulsar braking indices. *Ap&SS*, 308:317–323, Apr. 2007.

M. S. Longair. *High Energy Astrophysics: Volume 2, Stars, the Galaxy and the Interstellar Medium*. Cambridge University Press, 1994.

R. N. Manchester, G. B. Hobbs, A. Teoh, and M. Hobbs. The Australia Telescope National Facility Pulsar Catalogue. *AJ*, 129:1993–2006, Apr. 2005.

T. Montmerle. On gamma-ray sources, supernova remnants, OB associations, and the origin of cosmic rays. *ApJ*, 231:95–110, July 1979.

P. D. Morley. Pulsar glitches, ROSAT data and mass accretion. *A&A*, 313:204–208, Sept. 1996.

I. V. Moskalenko, T. A. Porter, and A. W. Strong. Attenuation of Very High Energy Gamma Rays by the Milky Way Interstellar Radiation Field. *ApJ*, 640:L155–L158, Apr. 2006.

R. A. Ong, V. A. Acciari, T. Arlen, et al. Highlight Talk: Recent Results from VERITAS. In *International Cosmic Ray Conference*, International Cosmic Ray Conference, 2009.

F. Pacini. Rotating Neutron Stars, Pulsars and Supernova Remnants. *Nature*, 219: 145–146, July 1968.

G. G. Pavlov, M. A. Teter, O. Kargaltsev, and D. Sanwal. The Variable Jet of the Vela Pulsar. *ApJ*, 591:1157–1171, July 2003.

J. Pétri and Y. Lyubarsky. Magnetic Reconnection at the Termination Shock of a Striped Pulsar Wind. *International Journal of Modern Physics D*, 17:1961–1967, 2008.

S. Pineault, T. L. Landecker, B. Madore, and S. Gaumont-Guay. The supernova remnant CTA1 and the surrounding interstellar medium. *AJ*, 105:1060–1073, Mar. 1993.

S. Pineault, T. L. Landecker, C. M. Swerdlyk, and W. Reich. The supernova remnant CTA1 (G 119.5+10.3): a study. of the breakout phenomenon. *A&A*, 324:1152–1164, Aug. 1997.

W. H. Press, S. A. Teukolsky, W. T. Vetterling, and B. P. Flannery. *Numerical Recipes in C (2nd ed.): The Art of Scientific Computing*. Cambridge University Press, 1992.

M. J. Rees and J. E. Gunn. The origin of the magnetic field and relativistic particles in the Crab Nebula. *MNRAS*, 167:1–12, Apr. 1974.

S. P. Reynolds and R. A. Chevalier. Evolution of pulsar-driven supernova remnants. *ApJ*, 278:630–648, Mar. 1984.

M. S. E. Roberts, R. W. Romani, and N. Kawai. The ASCA Catalog of Potential X-Ray Counterparts of GEV Sources. *ApJS*, 133:451–465, Apr. 2001.

G. Rowell and HEGRA Collaboration. TeV Observations of Selected GeV Sources with the HEGRA IACT-System. In *International Cosmic Ray Conference*, volume 4 of *International Cosmic Ray Conference*, page 2329, July 2003.

G. B. Rybicki and A. P. Lightman. *Radiative Processes in Astrophysics*. Wiley, 1979.

F. D. Seward, B. Schmidt, and P. Slane. X-Ray Emission from the Supernova Remnant CTA 1. *ApJ*, 453:284, Nov. 1995.

W. Sieber, C. J. Salter, and C. J. Mayer. Spectral and polarization characteristics of the supernova remnant CTA1. *A&A*, 103:393–404, Nov. 1981.

P. Slane, F. D. Seward, R. Bandiera, K. Torii, and H. Tsunemi. Nonthermal X-Ray Emission from CTA 1. *ApJ*, 485:221, Aug. 1997.

P. Slane, E. R. Zimmerman, J. P. Hughes, et al. X-Ray Observations of the Compact Source in CTA 1. *ApJ*, 601:1045–1049, Feb. 2004.

A. Spitkovsky. Particle Acceleration in Relativistic Collisionless Shocks: Fermi Process at Last? *ApJ*, 682:L5–L8, July 2008.

F. Stephenson and D. Green. *Historical supernovae and their remnants*. International series on astronomy and astrophysics. Clarendon Press, 2002.

A. W. Strong, I. V. Moskalenko, and O. Reimer. Diffuse Continuum Gamma Rays from the Galaxy. *ApJ*, 537:763–784, July 2000.

S. J. Tanaka and F. Takahara. A model of the spectral evolution of pulsar wind nebulae. *ApJ*, 715(2):1248, 2010.

S. J. Tanaka and F. Takahara. Study of four young tev pulsar wind nebulae with a spectral evolution model. *ApJ*, 741(1):40, 2011.

T. Temim, P. Slane, B. M. Gaensler, J. P. Hughes, and E. Van Der Swaluw. Chandra and XMM Observations of the Composite Supernova Remnant G327.1-1.1. *ApJ*, 691:895–906, Feb. 2009.

D. F. Torres, G. E. Romero, T. M. Dame, J. A. Combi, and Y. M. Butt. Supernova remnants and γ-ray sources. *Phys. Rep.*, 382:303–380, Aug. 2003.

G. Tóth. A General Code for Modeling MHD Flows on Parallel Computers: Versatile Advection Code. *Astrophysical Letters and Communications*, 34:245, 1996.

J. K. Truelove and C. F. McKee. Evolution of Nonradiative Supernova Remnants. *ApJS*, 120:299–326, Feb. 1999.

H. Uchiyama, H. Matsumoto, T. G. Tsuru, K. Koyama, and A. Bamba. Suzaku Observation of HESS J1825-137: Discovery of Largely-Extended X-Rays from PSR J1826-1334. *PASJ*, 61:189, Jan. 2009.

E. van der Swaluw. Interaction of a magnetized pulsar wind with its surroundings. MHD simulations of pulsar wind nebulae. *A&A*, 404:939–947, June 2003.

E. van der Swaluw, A. Achterberg, Y. A. Gallant, and G. Tóth. Pulsar wind nebulae in supernova remnants. Spherically symmetric hydrodynamical simulations. *A&A*, 380:309–317, Dec. 2001.

E. van der Swaluw, A. Achterberg, Y. A. Gallant, T. P. Downes, and R. Keppens. Interaction of high-velocity pulsars with supernova remnant shells. *A&A*, 397:913–920, Jan. 2003.

E. van der Swaluw, T. P. Downes, and R. Keegan. An evolutionary model for pulsar-driven supernova remnants. A hydrodynamical model. *A&A*, 420:937–944, June 2004.

A. Van Etten and R. W. Romani. Multi-zone Modeling of the Pulsar Wind Nebula HESS J1825-137. *ApJ*, 742:62, Dec. 2011.

VERITAS Collaboration, E. Aliu, T. Arlen, et al. Detection of Pulsed Gamma Rays Above 100 GeV from the Crab Pulsar. *Science*, 334:69, Oct. 2011.

H. J. Völk and K. Bernlöhr. Imaging very high energy gamma-ray telescopes. *Experimental Astronomy*, 25:173–191, Aug. 2009.

S. Wakely and D. Horan. TeVCat. `http://tevcat.uchicago.edu/`, July 2012.

T. C. Weekes, M. F. Cawley, D. J. Fegan, et al. Observation of TeV gamma rays from the Crab nebula using the atmospheric Cerenkov imaging technique. *ApJ*, 342:379–395, July 1989.

A. Weinstein. The VERITAS Trigger System. In *International Cosmic Ray Conference*, volume 3 of *International Cosmic Ray Conference*, pages 1539–1542, 2008.

V. I. Zatsepin and A. E. Chudakov. On the methods of searching for local sources of high energy photons. *J. Exp. Theor. Phys.*, 41:655, 1961.

L. Zhang, Z. J. Jiang, and G. F. Lin. High-energy Emission from CTA 1. *ApJ*, 699: 507–512, July 2009.